Ulm University
Institute of Orthopaedic Research and Biomechanics
Director: Professor Dr. Anita Ignatius

Mechanical Multiscale Characterisation of Vertebral Trabecular Bone for the Prediction of Vertebral Fracture Risk

Cumulative Dissertation to Obtain the Doctoral Degree
of Human Biology (Dr. biol. hum.)
of the Medical Faculty of Ulm University

handed in by Dipl.-Ing. Uwe Wolfram
born 2nd of July 1979 in Oelsnitz (Vogtl.)

Ulm, January 13, 2011

To my wife. Without you everything would be nothingness!

Acting Dean: Prof. Dr. Thomas Wirth
1. Reviewer: Prof. Dr. Hans-Joachim Wilke
2. Reviewer: Prof. Dr. Philippe K. Zysset
Date of Graduation: November 17, 2011

Contents

Definitions VI

1 Introduction **1**

2 Vertebral trabecular main direction **10**
2.1 Introduction 10
2.2 Material and Methods 11
2.3 Results 15
2.4 Discussion 19

3 Transverse isotropic elastic properties of dry vertebral trabecular bone matrix **22**
3.1 Introduction 22
3.2 Materials and Methods 23
3.3 Results 27
3.4 Discussion 30

4 Rehydration affects the elastic properties of vertebral trabecular bone **33**
4.1 Introduction 33
4.2 Material and Methods 35
4.3 Results 37
4.4 Discussion 41

5 Valid μFinite Element Models can be Set Up Directly With Nanoindentation **48**
5.1 Introduction 48
5.2 Materials and Methods 49
5.3 Results 52
5.4 Discussion 55

6 Damage Accumulation of Vertebral Trabecular Bone **61**
6.1 Introduction 61
6.2 Materials and Methods 62
6.3 Results 64
6.4 Discussion 69

7 Conclusion **73**

8 Bibliography **75**

A Acknowledgements **90**

B Scientific Curriculum Vitae **91**

C List of Publications **92**

Nomenclature

AX	axial
BMD	bone mineral density
CT	computer tomograph
E	Young's modulus
E_{app}	apparent Young's modulus
E^{dry}	Young's modulus under dry testing conditions
E^{exp}	experimental Young's modulus
E^{sim}	simulated Young's modulus
E_{tiss}	tissue Young's modulus
E^{wet}	Young's modulus under wet testing conditions
E_{AX}	axial Young's modulus
E_{TR}	transverse Young's modulus
FE	finite element
G	shear modulus
G_{app}	apparent shear modulus
G^{dry}	shear modulus under dry testing conditions
G^{exp}	experimental shear modulus
G^{sim}	simulated Shear modulus
G_{tiss}	tissue shear modulus
G^{wet}	shear modulus under wet testing conditions
GST	gradient structure tensor
HBSS	Hank's balanced salt solution
IT	inertia tensor
T1	1st thoracal vertebra
L2	2nd lumbar vertebra
L3	3rd lumbar vertebra
L5	5th lumbar vertebra
MIL	mean intercept length
PMMA	Poly-Methyl Methacrylate
PU	Polyurethane
ROI	region of interest
VOI	volume of interest
T	torsion
TR	transverse
T6	6th thoracal vertebra
T8	8th thoracal vertebra
T10	10th thoracal vertebra
T12	12th thoracal vertebra

UC	uniaxial compression
UT	uniaxial tension
p	statistical significance level
r^2	Pearson's correlation coefficient
r_c	concordance correlation coefficient
r^{dry}	correlation coefficient for dry testing conditions
r^{wet}	correlation coefficient for wet testing conditions
u_z	displacement in z-direction
$\|u\|$	absolute displacement
W	total indentation work in mNμm
W^d	dissipated indentation energy in mNμm
W^e	elastic indentation energy in mNμm
ε_i	i^{th} load step
ε^{UC}	uniaxial compressive strain
ε^{UT}	uniaxial tensile strain
γ	shear strain
μCT	micro computer tomograph
μFE	micro finite element

Explanations

apparent Young's modulus	Young's modulus of a specimen of trabecular bone that is dissected from the trabecular core of vertebral bodies. It is different to the effective *in situ* stiffness since the trabecular connectivity is destroyed.
apparent shear modulus	Shear modulus of a specimen of trabecular bone that is dissected from the trabecular core of vertebral bodies. It is different to the effective *in situ* stiffness since the trabecular connectivity is destroyed.
anisotropy	Denotes the directional dependence of a mechanical property. For instance, bone stiffness is higher when loaded in longitudinal direction than in transverse direction.
damage	Represents the decay in stiffness and can be understood as the effective surface density of microdefects.
dissipated energy	Measures the energy lost during a mechanical deformation.
elastic energy	Measures the recoverable energy after release of a mechanical deformation.
elastic modulus	The slope of the initial stress-strain curve is called elastic modulus or Young's modulus.
eigenvalue	Characteristic values of a tensor or matrix are called eigenvalues. In terms of the mean intercept length fabric tensor its eigenvalues can be understood as the characteristic mean intercept lengths for the analysed specimen.
eigenvector	Characteristic main directions of a tensor are called eigendirection. In terms of the mean intercept length fabric tensor its eigenvecors can be understood as the characteristic main directions of the pores or trabeculae of the analysed trabecular specimen.
gradient	Denotes the derivative on a scalar field such as the grey value field obtained with computer tomography.

heterogeneous	Denotes the irregularity or nonuniformity of elements of a set with respect to one or more properties.
homogeneous	Denotes the regularity or uniformity of elements of a set with respect to one or more properties.
inertia	The resistance of a physical object to changes in its state of motion is called inertia.
indentation modulus	Denotes a stiffness obtained from the unloading curve of an indentation experiment without an assumption about the material symmetry of the specimen.
isotropy	A property that is isotropic is direction independent. For instance, most metals show the same stiffness when loaded from different directions.
linear elastic material	A material where stresses and strains are proportional related and where any answer to an inscribed load is reversible if the load is withdrawn is linear elastic.
modulus	Slope. In terms of a linear elastic material it denotes the slope of the stress strain curve and, thus, the stiffness.
tensor	Physical quantity containing of magnitude and direction for a material particle. In case of a second order tensor such as the stress tensor it is written as 3×3 matrix which contains six independent values, three normal and three shear stresses. Each stress is described by its magnitude, the normal direction of the area on which it is acting and the direction in which it is acting. A first order tensor is a vector and a zeroth order tensor is a scalar.
transverse isotropic	Describes the direction dependence of a property where in the transverse plain there is no difference but between this and the longitudinal direction.

scalar product	Dot product is an algebraic operation that takes two equal-length sequences of numbers (usually coordinate vectors) and returns a single number obtained by multiplying corresponding entries and adding up those products.
strain	The relative displacement between two particles in a material body is called strain.
strength criterion	For an arbitrary load direction a strength criterion describes the point where the maximal bearable load is exceeded.
volume fraction	Relative volume content of a quantity is called volume fraction. In case of bone volume fraction it describes the relative amount of bone in an evaluated volume.
yield criterion	For an arbitrary load direction a yield criterion describes the point from where on irreversible deformations occur.

Chapter 1

Introduction

Osteoporosis in general, is a major problem of aging societies (Maghraoui et al., 2008). It causes only in Europe an estimated 32 billion Euro annual costs which are expected to rise to an estimated 77 billion Euro by 2050 (Kanis and Johnell, 2005). One third of all women beyond their menopause and one fifth of all men beyond the age of fifty are affected (Randell et al., 1995). The disease is characterised by a loss of bone mass which is radiographically detectable in a decrease of bone mineral density (BMD). Osteoporosis results in a loss of structural integrity (Keaveny and Yeh, 2002) and, thus, in an increased risk of fracture of the bone tissue.

Bone mass is gained during growth at young age. At approximately 30 years peak bone mass is reached and a gradual decrease in bone mass begins (Figure 1.1). Bone loss can be introduced by different factors such as disuse (Bikle et al., 1997; Donahue et al., 2006; Lennox and Goodship, 2008), hormonic diseases (Sato et al., 2005), malnutrition (Schürch et al., 1998; Huang et al., 1998; Hannan et al., 2000; Chapuy et al., 2002; Shea et al., 2002) or ageing (Frost, 1997; Keaveny and Yeh, 2002). Generally, it can be distinguished in primary and secondary osteoporosis. Whereby primary osteoporosis is due to ageing and in women due to post-menopausal hormonic changes. Secondary osteoporosis can be found within the course of an illness. Both are detectable by a changing bone mass. In primary osteoporosis, the BMD lifetime curve shows distinct effects for males and females. The age induced decrease in bone mass (senile or type II osteoporosis) is noticeable for males after peak bone mass is reached. Women build up significantly lower peak bone mass and suffer a severe drop of bone mass due to decreasing hormone levels (mainly oestrogen) after menopause (post-menopausal or type I osteoporosis). This drop is followed by an age induced decrease in bone mass.

Eventually, osteoporosis manifests itself through a fracture. Regarding the evolution of the life expectancy which indicates that in 2004 German women over 60 years had a life expectancy of 84 years and men over 60 years had a life expectancy of 80 years (Eisenmenger et al., 2006) an increasing amount of vertebral fractures due to osteoporosis or other age dependent diseases can be expected. This trend is further corroborated by the continuously increasing life expectancy of newborns (Eisenmenger et al., 2006) which will lead to an increase in the lifetime risk of suffering a forearm, hip or vertebral fracture which was already 41% in 2000 (Kanis, 2002).

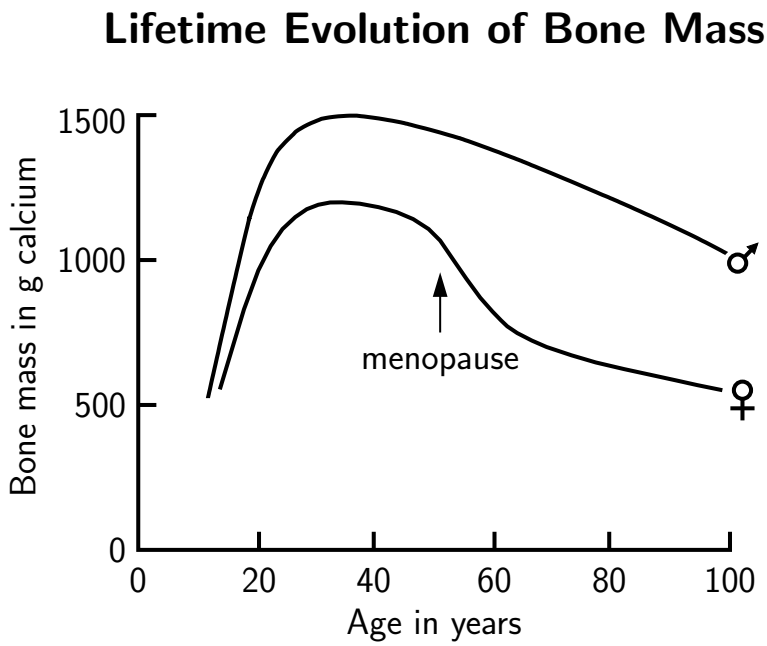

Figure 1.1: Bone mass evolution over age. Two distinct effects are visible for males and females. In males, bone mass decreases almost linearly after reaching the peak with approximately 30 years. In females, a severe drop due to decreasing oestrogen levels occurs after the menopause. The figure was adapted from different sources (Riggs and Melton III, 1983; Thomsen et al., 1986; Bonjour et al., 1994; World Health Organization, 1994, 2003; Verhulp, 2006).

Nine million new fractures occur annually world wide (Johnell and Kanis, 2006). Among these nine million fractures, 1.6 million hip fractures, 1.7 million forearm fractures and 1.7 million clinical vertebral fractures could be distinguished. Overall 51% of these fractures occurred in Europe and North America. Furthermore, 51% of all fractures occur in women (Johnell and Kanis, 2006). The risk of suffering any type of fracture increases to 86% after a previous fracture history (Kanis et al., 2004). It was shown that radius and vertebral fractures show the highest prevalence as first fractures in post-menopausal women (Sontag and Krege, 2009). Therefore, the diagnosis and treatment of vertebrae at risk of fracture or already fractured vertebrae is important to initiate treatments that could possibly hinder a subsequent fracture. However, the under-diagnosis of vertebral fractures is a major problem with false-negative rates (undiagnosed and therefore untreated vertebral fractures) of 45.2% in North America, 46.5% in Latin America and 29.5% in Europe/South Africa/Australia (Delmas et al., 2005).

Structure and Function of Vertebral Bone The central load bearing element of the human skeleton is the spinal column. The spinal column without the sacral

bones is usually made up of 24 individual vertebrae which are connected by intervertebral discs, muscles and ligaments. As all bones, vertebrae provide support for the body. In general, bones shape the skeleton and transfer loads to enable movement. They provide protection for the large organs in the cranial, thoracal and pelvic cavities. Besides being the central element for this skeletal protection, the spinal column protects and houses the spinal cord, which enables the propagation of nerves throughout the body. The red bone marrow located within the vertebrae produces blood cells (haematopoiesis). In ageing bodies, red bone marrow is replaced by yellow bone marrow and the haematopoiesis is decreased. The yellow marrow can be usually found in the medulla of long bones and serves as fat reservoir. Vertebrae and all other bones serve as storage for minerals such as calcium or important growth factors such as insulin like growth factors and bone morphogenetic proteins.

Macro-anatomically bones can be roughly distinguished in irregular shaped bones such as vertebrae, flat bones such as the cranial bones, and long bones such as the femur. The irregular shaped bones and here especially the vertebrae, the flat bones and the ends of the long bones usually consist of a trabecular core within a cortical shell (Figure 1.2). Cortical and trabecular bone are build up essentially the same. The bone matrix consists of approximately 10% water, 20% organic material and 70% anorganic material. The anorganic material is mainly mineral in form of hydroxyapatite. The organic material consists of approximately 95% collagen type I and 5% proteoglycans and other non-collagenous proteins such as Osteonectin, Osteopontin and Osteocalcin (Cowin, 2001). Cortical and trabecular bone are macroscopically distinguishable over their bone volume fraction. The trabecular core shows a bone volume fraction of $5-60\%$ while cortical bone shows a bone volume fraction of $80-95\%$ (Jee, 1983). The trabeculae vary from slender rods to thick plates. Their shape and orientation is governed by the local mechanical environment. The orientation of trabeculae were related to stress trajectories (Culmann's crane[1]) in a homogeneous structure with similar geometry (von Meyer, 1867; Wolff, 1870). This concept of the trabecular orientation following local mechanical loads led to "Wolff's Law" which describes the adaption of bone to external loads (Wolff, 1892). The present ideas about the functional adaption of bone follow the concept that it is governed by bone cells which are influenced by their local strain state (Roux, 1881; Klein-Nulend and Bacabac, 2005).

The combination of organic and anorganic materials and cells makes bone a living organ which is able to grow and heal itself. The bone tissue is constantly remodelled by an equilibrium between bone resorption performed by osteoclasts

[1]The drawing of Culmann's crane was depicted in Wolff's original work about the inner architecture of bone (Wolff, 1870). The relation of stress trajectories to trabecular orientation was probably done by Culmann based on a line drawing of trabecular orientation by von Meyer (1867).

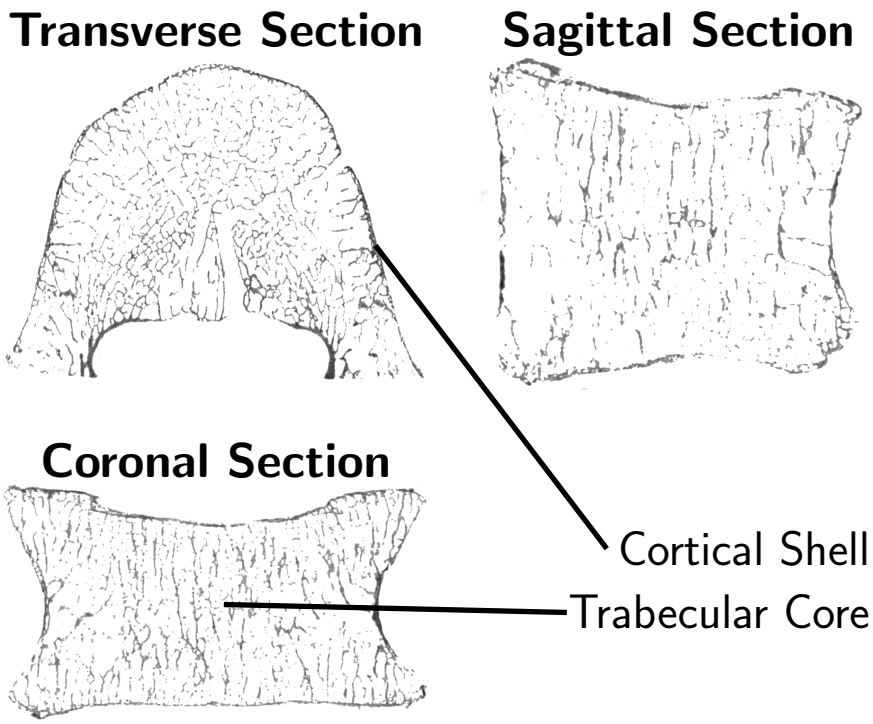

Figure 1.2: Transversal, sagittal and coronal midplane images of a micro-computer tomography (μCT) scan of a L4 vertebra of an 86 y old female donor are shown. The difference in density and thickness between cortical bone and trabeculae is visible. The microscopic resolution of $(30\ \mu m)^3$ reveals that the morphological main difference between cortical and trabecular bone is the respective porosity.

and bone modelling carried out by osteoblasts. A remodelling cycle starts with the disposal of osteoclasts. These cells resorb bone using a local acid (Hydroxy-Chloride Acid) environment (Kornak and Mundlos, 2003). Subsequently, the generated cavity is filled by osteoblasts with an organic matrix (osteoid) that is later mineralised to form mature bone. During the disposal of new bone, some osteoblasts are trapped within the bone matrix and differentiate to osteocytes. Each individual osteocyte is connected to other osteocytes or to bone lining cells on the bone surface (flattened osteoblasts). The cell network enables the transmission of mechanically stimulated cell signals to control the gain and loss of bone (Klein-Nulend and Bacabac, 2005). This enables bone to adjust to external loads and generate and maintain a structure that is optimised in shape and strength. This yields a dominant orientation of trabeculae in superior – inferior direction in vertebral bodies (Figure 1.2). Deviations from this dominant direction are due to other external load influences to the vertebral body such as muscle forces or age induced changes in the double-s-shape of the spinal column. If the remodelling process is not in an equilibrium state, the adaption to external loads is insufficiently and

results in a weaker bone structure and reduced strength. The most severe disturbance of the remodelling cycle is called osteoporosis where an over-expression of osteoclasts (Raisz, 2005) leads to higher bone resorption. Due to the higher ratio of bone surface to bone volume (active surface for osteoclasts to attach), trabecular bone is more vulnerable to bone resorption than cortical bone. Thus, the mechanical properties of the trabecular core seem more important for the understanding of vertebral fracture load.

A side note about vertebral fractures is helpful to develop an idea about the course of these fractures and why certain characteristics should be investigated. Vertebral fractures occur as Type A fracture (Magerl et al., 1994), i. e. vertebral body compression without injured posterior structures, in over 60% of all cases (Magerl et al., 1994; Reinhold et al., 2009). Most of the vertebral fractures were detected in the thoraco-lumbar conjunction T10 to L1 (Magerl et al., 1994; Reinhold et al., 2009). This is attributable to the different compliance of the thoracal and the lumbar spinal column which are due to the stiffening effect of the costae. Of these type A fractures, 51% were wedge fractures, 17% biconcave fractures, 13% crush fractures, 7% combined wedge and crush fractures, 6% combined wedge and biconcave fracture and 4% combined wedge crush biconcave fractures.

The fracture risk of vertebral bodies is dependent on the loading mode, the previous load history and the trabecular bone conditions such as reduced density or induced damage. A third of all vertebral fractures is caused by falls, 15% by lifting heavy loads or traffic accidents and 50% are not relatable to single traumatic events (Silva, 2007). In the latter case vertebrae can show sinter processes which indicate the accumulation of damage and permanent deformation (Keaveny et al., 1994) in a cyclic fatigue fashion. Vertebrae can also accumulate substantial damage after isolated overloads. The associated small permanent deformation is not detectable in clinical radiographs but with a decrease in stiffness and strength (Kopperdahl et al., 2000). This damage accumulation can increase the risk of fracture (Fyhrie and Schaffler, 1994; Burr et al., 1997; Kopperdahl et al., 2000) and finally lead to collapsing vertebrae. In addition, the ability of bone to repair occurring damage decreases with age while at the same time bone microdamage increases with age (Waldorff et al., 2007; Burr et al., 1997). A clear understanding of the damage properties of vertebral trabecular bone is thus mandatory for the prediction of fracture load.

Reloading of trabecular bone leads to severe loss of stiffness and accumulation of residual strain (Zysset, 1994; Keaveny et al., 1994, 1999). Qualitatively, this damage accumulation appears to be independent on site, species and density (Keaveny et al., 1994; Zysset and Curnier, 1996; Kopperdahl et al., 2000). Cortical bone shows

qualitatively similar damaging behaviour as trabecular bone (Fondrk et al., 1988; Garcia et al., 2010). This suggested that similar damage mechanisms are present at the nanometer level (Keaveny et al., 2001) were cortical and trabecular bone are structural similar. Cracks and diffuse damage that accumulate within trabeculae cause reductions in apparent modulus prior to failure of whole trabeculae (Wachtel and Keaveny, 1997). This was corroborated by findings that trabecular bone accumulates damage already at small apparent strains lower than apparent ultimate strain (Morgan et al., 2005). Trabecular damage leads then to the formation of fracture bands or greater regions of fractured trabeculae (Moore and Gibson, 2001; Thurner et al., 2006) until overall failure. Thus, damage of trabecular bone is a mixture of microcracking, diffuse damage and fractured trabeculae. It occurs already at small deformation. In a healthy metabolism it is a stimulus for bone remodelling and repair (Martin, 2002; Lee et al., 2006). In an unhealthy metabolism it increases the fracture susceptibility (Cooper, 1993; Burr et al., 1997; Mc Donnell et al., 2007).

Finite Element (FE) models provide the possibility to study the mechanical behaviour of vertebrae and other spinal structures numerically *in silico* (Shirazi-Adl et al., 1986; Crawford et al., 2003a; Schmidt et al., 2007; Chevalier et al., 2009). The possibility to predict vertebral fracture risk from computer tomography (CT) generated image data would be very useful for the management of patients with osteoporosis. The identification of the most beneficial intervention site by finding the vertebrae with the highest risk of fracture or a load threshold that should be avoided during daily activities could be supported by CT-based anatomy specific FE models. Continuum level FE simulations of whole bones require effective macroscopic material properties to accurately represent the mechanical behaviour of vertebrae.

Constitutive continuum models have been developed to describe the mechanical behaviour of trabecular and cortical bone including its specific bone mass and the main orientation of its spatial distribution (Zysset, 2003). They were further developed to include the irreversible damage and softening behaviour occurring after overloading the bone (Zysset and Curnier, 1996; Garcia et al., 2009). These material models can be included in FE simulations which could be used to improve the determination of fracture load (Chevalier et al., 2009). However, those material models depend critically on the quality of the input parameters. It was found that the material properties of bone are site specific (Morgan and Keaveny, 2001; Morgan et al., 2003). Furthermore, it is known that they are distinctly direction dependent (Cowin, 1985). Thus it is necessary to determine the input parameters for FE simulations for the specific anatomic site of interest in different directions. A major part of the vertebral load is borne by the cancellous core. It

is known, that the cortical shell plays an important role in the uptake and sharing of external compressive loads (Eswaran et al., 2006). How this holds for off axis or multiaxial loads is unclear. However, since it constitutes the greatest part of the vertebral volume, the load baring capabilities of the cancellous core take on a key role for the mechanical resistance of whole vertebral bodies. Due to its hierarchical nature (Rho et al., 1998), the macroscopic material behaviour of vertebral bone especially the cancellous core may be dependent on the micromechanical properties of the contained trabeculae (Zysset et al., 1999). Thus, it is necessary to understand the mechanical behaviour of vertebral trabecular bone at different length scales to properly incorporate the mechanical behaviour of vertebral bone tissue in FE simulations.

The hierarchical structure of bone are (1) the macro-structure where trabecular and cortical bone can be distinguished (Figure 1.2); (2) the microstructure from 10 to 500 μm with single trabeculae, osteons, Haversian channels; (3) the submicrostructure form 1 to 10 μm with single lamellae; (4) the nanostructure from a few hundred nm to 1 μm with collagen fibrilla and mineral platelets; and (5) the sub-nanostructure below a few hundred nm with molecular structure of the constituent materials such as mineral, collagen, non-collagenous proteins (Rho et al., 1998). These multiple scales constitute a hierarchically organised heterogeneous and anisotropic structure. This means that vertebral bone shows load direction dependent (anisotropic) behaviour over different length scales.

From a clinical point of view the determination of vertebral fracture load or the mechanical behaviour after implantation shows of course a similar hierarchy, which can be considered shifted upwards one scale (Figure 1.3). The hierarchy starts at the patient level where sites such as the spinal column are of interest for the deployment of treatments such as vertebroplasty, implants or the prediction of fracture load. It than steps down to the patient specific anatomy of single vertebrae. The mechanical behaviour of these is critically influenced by the underlying material properties, which vary spatially within the vertebral body. These local material properties could be in turn influenced by the microscopic material properties of single trabeculae. If simulations should be used for the determination of vertebral fracture load or the assessment of the mechanical impact of spinal implants the used material properties need to reflect these multiscale nature. No attempt has been made to scale up the mechanical behaviour starting at the microscale and ending at the macroscale, which is necessary for simulations to determine the vertebral fracture load.

The objectives of this cumulative PhD-thesis were set to form the basis for the prediction of vertebral fracture load. Prevention of vertebral fractures necessitates

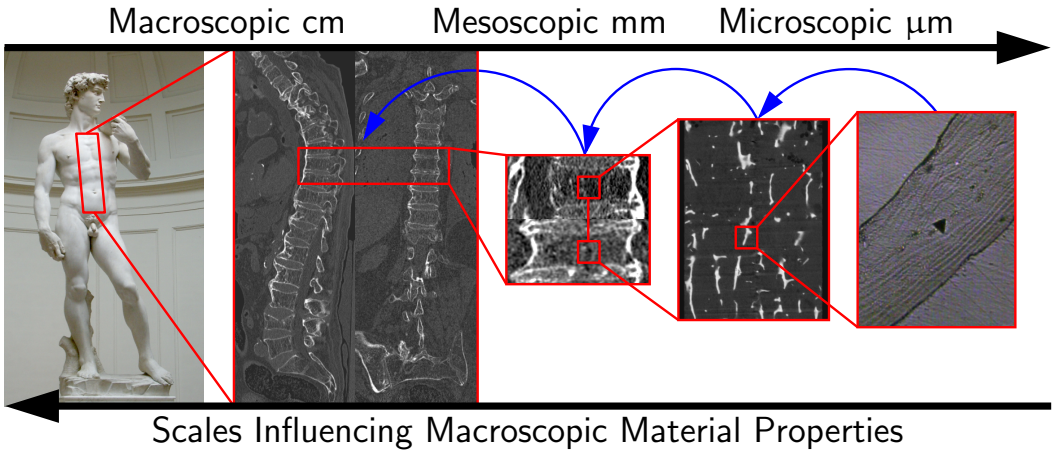

Figure 1.3: Hierarchical scales affecting the mechanical competence of vertebral bones (1) patient scale; (2) the macroscale with the spinal column as the site of interest for treatment or analyses; (3) the mesoscale with single anatomy specific vertebral bodies which contain trabecular and cortical bone; (4) the upper microscale with locally heterogeneous trabecular bone; (5) the lower microscale with single trabeculae. First shows Michelangelo's David, Wikipedia, `http://de.wikipedia.org/wiki/David_(Michelangelo)`.

the diagnosis of the weakest vertebrae in the spinal column. This necessitates detailed knowledge of the mechanical properties of the trabecular core, since it constitutes the major load bearing part of a vertebra. To reflect the multiscale nature of vertebral trabecular bone this thesis investigated mechanical properties from the micro- to the macro-scale. A combination of numerical and experimental methods was used to address the following research questions:

(i.) The bone mineral density could serve as measure for the amount of bone mass. However, it is known that the spatial orientation of vertebral trabecular bone is the second critical independent variable characterising its mechanical behaviour. Is it possible to detect the trabecular orientation from clinical CT datasets?

(ii.) The macroscopic mechanical behaviour, morphologically mainly characterised by bone volume fraction and trabecular orientation, may be influenced by the microscopic mechanical properties such as stiffness. The question arises, how big is the stiffness of the bone material of single trabeculae? How is it distributed and how big are the directional differences?

(iii.) The micromechanical properties were determined on dried sections of trabecular bone. Thus, the experiments were maximally controllable but not physiological. This initiated the investigation of the effects of rehydration.

How big is the micromechanical stiffness of vertebral trabecular bone and their distribution in a hydrated more physiological setting?

(iv.) Macroscopic stiffness of vertebral trabecular bone may be dominated by its microscopic stiffness. Using the experimental results on the microscale, large scale finite element models were set up. Can the macroscopic stiffness be simulated in a hydrated setting and is it necessary to use specimen specific micromechanical stiffness of vertebral trabecular bone?

(v.) Clinical research questions targeting the fracture load of vertebral bodies or the behaviour of implants and their effects on the affected vertebrae necessitate accurate knowledge about the macroscopic mechanical properties of the vertebral trabecular core. Furthermore, it is important to know whether the mechanisms leading to vertebral collapse are dependent on the load direction. Is the damage evolution in cranial-caudal different from that in transverse loading direction? Does the accumulation of damage depend on loading mode?

These research questions have led to the peer reviewed publications which are summarised in the following sections and attached to this manuscript. The first research question addresses a practical question. It is necessary to show that trabecular orientation can be determined using clinical CT scanners and settings without additional effort. Otherwise it is not possible to use modern material models that incorporate the trabecular orientation besides BMD for the determination of fracture load.

The second and third research questions were mainly dedicated to the material properties along a trabecula. However, the experiments were set up so that the influences of age and gender on the micro-mechanical properties of vertebral trabecular bone could be investigated.

The fourth research question aimed at the possibility to simulate macro-mechanical properties if the specific micro-mechanical properties are known from experiments. The study provided the opportunity to investigate the influence of the variability of the micromechanical stiffness on the macromechanical properties of vertebral trabecular bone. This indicated whether the macroscopic mechanical properties are dominated by the micromechanical properties.

Finally, the fifth research question experimentally addressed the macroscopic material behaviour of vertebral trabecular bone in the reversible and irreversible load range. The damage properties investigated therein are crucial for the understanding of vertebral fracture load.

Chapter 2

Vertebral trabecular main direction

As published in: Wolfram, U., Schmitz, B., Heuer, F., Reinehr, M., Wilke, H.-J., 2009. Vertebral Trabecular Main Direction can be Determined From Clinical CT Datasets Using the Gradient Structure Tensor and not the Inertia Tensor — A Case Study. Journal of Biomechanics 42 (10), 1390 — 1396. ★

2.1 Introduction

Osteoporosis is a wide spread disease with one third of all women beyond their menopause and a fifth of men above the age of 50 years suffering from it (Randell et al., 1995). The disease is characterised through a loss of bonemass, which induces a decrease in mechanical performance and structural integrity. Thus, the ability to withstand unusual loads diminishes (Karlsson et al., 2005). In vertebra the incidence of fractures increases with age in both genders, which constitutes a severe cost factor for health care systems (EFFO and NOF, 1997; Kanis and Johnell, 2005).

The gold standard of assessing the fracture risk of human vertebrae is the measurement of bone mineral density (BMD) using for instance dual x-ray absorptiometry (DEXA) (Ito et al., 1997) or quantitative computer tomography (qCT) (Andresen et al., 2006). However, the measurement of BMD indicates osteoporosis but not necessarily the specific fracture risk (Siris and Delmas, 2008). Patient specific Finite Element (FE) models would be a great improvement for the diagnosis of vertebral fracture risk (Faulkner et al., 1991; Crawford et al., 2003a; Liebschner et al., 2003; Crawford et al., 2003b). In these models, patient specificity is usually incorporated using empirical relations between BMD of the trabecular structures and their stiffness besides the specific vertebra geometry. The great advantage of those relationships is that BMD can be measured easily in situ using qCT scans (Crawford et al., 2003a; Helgason et al., 2008). It is known that the tissue heterogeneity and structural anisotropy (Goulet et al., 1994) cannot be expressed with BMD alone (Jiang et al., 1998; Ulrich et al., 1999; Teo et al., 2007). It was furthermore found that the incorporation of the local anisotropy can improve explanatory power of specific FE models of trabecular structures (Rietbergen et al., 1996, 1998; Keaveny et al., 2001; Morgan et al., 2004). Different material models have been

proposed, which incorporate information about the anisotropy of trabecular bone in addition to BMD using a second rank structure tensor (Zysset, 2003).

Classically, the structure tensor of trabecular bone is measured from μCT datasets using for instance the mean intercept length ($\mathbf{M}^{MIL}$) concept (Whitehouse, 1974; Harrigan and Mann, 1984; Odgaard, 1997). Unfortunately this method cannot be applied to coarse resolutions or in situ datasets gained at adequate radiation doses, because the phase boundaries of the bone and the marrow phase cannot be distinguished properly. Recent studies determined the anisotropy from high resolution Magnetic Resonance datasets using autocorrelation analysis on clinically gained datasets. These experiments were restricted to peripheral sites (Rotter et al., 2001; Wald et al., 2007).

Rao and Schunk (1991) proposed the gradient structure tensor ($\mathbf{M}^{GST}$) to determine texture orientation. In a recent paper, Tabor and Rokita (2007) applied this method to grey level images of explanted vertebrae submerged in water. Alternatively, Jähne (2002) proposes the usage of the inertia tensor ($\mathbf{M}^{IT}$) to compute structure. The question remains which of the latter methods is applicable to determine vertebral trabecular structure in situ.

This study aimed to measure structure of human vertebral trabecular bone under in situ conditions using clinically achievable resolutions and appropriate radiation doses. Structure information of vertebrae derived from clinical datasets using $\mathbf{M}^{GST}$ and $\mathbf{M}^{IT}$ were compared to those derived from μCT datasets at the same locations using $\mathbf{M}^{MIL}$.

2.2 Material and Methods

To work in a setting as close as possible to the in vivo situation the experiments were performed on a fresh 88 years old full body donor[1]. The donor could be regarded as osteoporotic according to the WHO recommendations with a T-Score of -4.87 and a Z-Score of -1.39 (World Health Organization, 1994). A data acquisition protocol was used to extract comparable datasets at different scan levels (Figure 2.1).

Scans in the in situ setting were performed using a clinical full body CT (Philips Mi8000 IDT 16, Philips Medical Systems, Netherlands). Two basic protocols were used in the in situ setting, a normal dose (ND) and a high dose (HD) routine. Datasets at different radiation doses and resolutions were generated (Table 2.1). The donor was positioned for thorax screening, i.e. the arms were laid back behind the head so that they could not attenuate the x-rays.

Subsequent to the scans in the in situ setting, the spinal column was explanted and dissected. Four representative vertebrae (T8, T10, T12, L2) were selected and

[1]Confirmation of the ethical board of Ulm University is ensured!

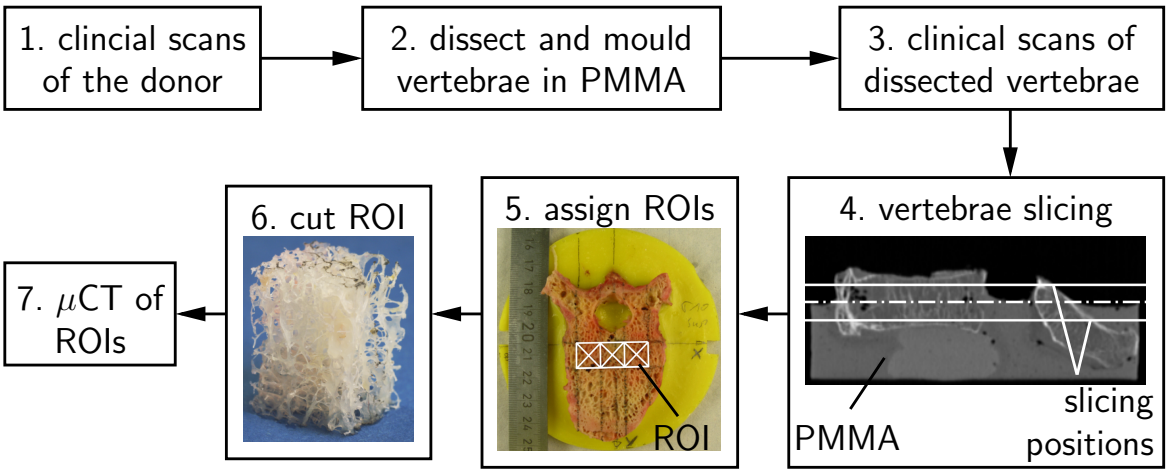

Figure 2.1: Chart of the data acquisition process. Four kinds of datasets were generated, a normal and a high dose scan after step 1 of the whole spinal column, two high dose scans of four dissected vertebrae after step 3 and a μCT scans of the ROIs defined and dissected in step 5 and 6.

moulded in polymethyl methacrylate (PMMA) cylinders. These vertebra-PMMA complexes were scanned again with the clinical CT using a high dose protocol (HD512, Table 2.1).

Table 2.1: Protocol of the image acquisition. Scans in the in situ setting are evaluated with respect to patient applicability using the dose length product (DLP) provided by the scanner software. DLPs for the normal dose (ND) and high dose (HD) scans are for a scan of the whole spinal column. The in situ settings are standard clinical routines used in daily practise. The in vitro settings in the clinical scanner (HD512) are gained with a high dose routine.

Scan	Resolution in μm	DLP in $cGy \cdot cm$	CT	setting
ND	$365 \times 365 \times 500$	639	Philips Mx8000	in situ
HD	$365 \times 365 \times 500$	1700	IDT 16	in situ
HD512	$365 \times 365 \times 500$	–	Philips Mx8000	in vitro
μCT	$30 \times 30 \times 30$	–	Stratec μ-Scope	in vitro

Following these scans, the vertebrae were further processed by removing the superior and inferior endplates with a high precision band saw (Exakt Apparatebau, Norderstedt, Germany). Cutting positions were defined using the CT datasets of the explanted vertebrae so that a 14 mm high slice was obtained (Figure 2.1, Step 4).

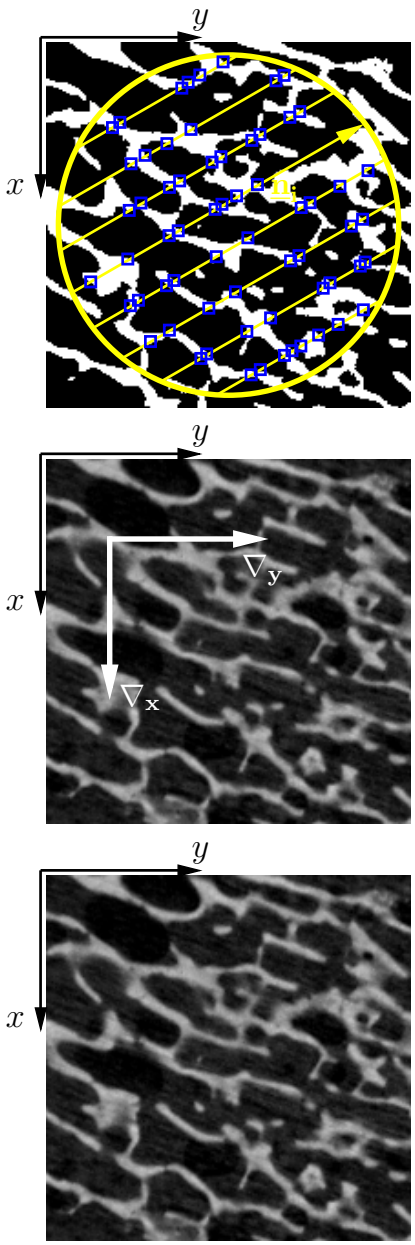

$$\underline{\underline{\Theta}}^{MIL} \leftarrow \frac{L}{I\left(\underline{n}_i\right)}$$

$$\underline{\underline{\Theta}}^{GST} = \int_V \nabla u(\underline{x}) \otimes \nabla u(\underline{x})\, d\underline{x}$$

$$\underline{\underline{\Theta}}^{IT} = \int_V \rho(\underline{x}) \left((\underline{x} - \underline{s})^2 \cdot \underline{\underline{\mathbb{I}}} - (\underline{x} - \underline{s}) \otimes (\underline{x} - \underline{s}) \right) d\underline{x}$$

Figure 2.2: Used structure tensors. Left, sketched ROIs and right, definition. On top MIL which is regarded as gold standard. Here the orientation distribution is gained by superimposing a virtual measurement grid in the μCT dataset. Subsequently the number of intersections of the grid with bone-marrow interfaces is determined for several directions $\underline{n}_i$. Dividing the grid length by this number gives the mean intercept length for $\underline{n}_i$. Fitting this to an ellipsoid yields the MIL structure tensor. The middle shows the gradient structure tensor (GST). Here the gradient vector is computed for every point in the gray value dataset. Calculating the dyadic product and integrating over the whole ROI yields the GST. Finally, the bottom line describes the inertia tensor. The gray values are regarded as distributed mass points within the ROI.

Three regions of interest (ROI) were defined on the superior face of each remaining slice (Figure 2.1, Step 5). Subsequently, a photo was taken with a digital camera (Olympus Camedia C-5060 Wide Zoom, Olympus Corporation, Tokyo, Japan). The ROIs were dissected, delivering 12 hexahedral specimens of size $10 \times 10 \times 14$ mm. The specimens were cleaned from marrow using a pulsed water jet (Braun Oral-B PC 8500 Oxyjet, Kronberg, Germany) and scanned in a µCT (XCT FAN Beam µ-Scope, Stratec Medizintechnik GmbH, Pforzheim, Germany) at 30 µm resolution.

To allow for comparisons of structure measurements at the different scanning levels, e.g. between the µCT and a clinical level, the datasets were aligned using image registration algorithms (MatLab, The MathWorks, Natick, MA, USA).

The clinical datasets were considered noisy. Thus, it was necessary to investigate the need of an image enhancement process in all steps of the data analysis. A coherence enhancing, nonlinear anisotropic diffusion process was chosen to reduce noise and reconnect fragmentary resolved structures (Weickert, 1998). A diffusion algorithm proposed by Brosper et al. (2005) was adopted and implemented in MatLab. The system of partial differential equations derived from setting up the diffusion process in every point of the datasets was modelled using a finite volumes scheme and solved with a biconjugate gradients stabilised method. An explicit Euler method was used for the time-integration. Three kinds of image enhancements were performed, that are "plain", "main" and "weickert". The first "plain" is simply no enhancement. The second "main" allows diffusion along the main direction of the underlying structure. In the third "weickert", the diffusion process recognised whether the underlying structure was rod-, plate- or sphere-like and allowed for cross diffusion in one, two or all directions (Weickert, 1998).

Three points along the longitudinal axis of each of the 12 hexahedral ROIs were chosen to determine and compare structure through the different scan levels giving 36 measurement points. Cubic sub-ROIs of 6 mm edge length (Harrigan et al., 1988) were defined around these points to determine $\mathbf{M}^{GST}$ and $\mathbf{M}^{IT}$ in the datasets obtained with the clinical scanner. $\mathbf{M}^{MIL}$ was determined solely at the µCT level and served as standard against which $\mathbf{M}^{GST}$ and $\mathbf{M}^{IT}$ were compared in each scan level (see Figure 2.2 for a description of the tensors).

The comparison was carried out by correlating the eigenvalues. Performance with regard to main direction was tested by calculating the scalar product between the eigenvectors $\underline{v}$ of the structure tensors which point in trabecular main direction. That means that if the scalar product between $\underline{v}^{MIL}$ and $\underline{v}^{GST}$ or $\underline{v}^{IT}$ was one, the eigenvectors pointed in the same direction. Thus, $\underline{v}^{GST}$ or $\underline{v}^{IT}$ respectively determined from a clinical dataset can be considered to indicate the same trabecular main direction as $\underline{v}^{MIL}$ determined from the µCT scans.

To exclude a possible bias constituted through the fact that the trabecular structures are imaged with different resolutions, i.e. slice distance is greater than in-

plane resolution, measurements are repeated on the same points but with artificially declined ROIs. The declination angles were determined using a random number generator (MatLab) and held constant through the scan levels for each ROI. Furthermore, the robustness of $\mathbf{M}^{GST}$ and $\mathbf{M}^{IT}$ in comparison to $\mathbf{M}^{MIL}$ to geometrical errors was tested by compressing the datasets prior to the rotation of the ROIs and assuming an isotropic resolution.

Statistical tests were carried out using the Wilcoxon rank sum test in MatLab with a significance level of $p < 0.05$.

2.3 Results

Eigenvalues determined with $\mathbf{M}^{GST}$ or $\mathbf{M}^{IT}$ did not correlate with those determined with $\mathbf{M}^{MIL}$ $p >> 0.05$ and $|r^2 < 0.5|$. See Figure 2.3 on the results for the artificially declined datasets gained with the ND protocol. Scanning levels HD and HD512 did not produce better results.

Comparing the trabecular main directions determined from the clinical scans to those determined from the µCT datasets in 3D indicates that $\mathbf{M}^{GST}$ and $\mathbf{M}^{IT}$ can predict the trabecular main direction determined with $\mathbf{M}^{MIL}$. The median of the scalar products for the normal dose scans without image enhancement was approximately 0.98 for the comparison $\mathbf{M}^{MIL}$ and $\mathbf{M}^{GST}$ and 0.99 for the comparison of $\mathbf{M}^{MIL}$ and $\mathbf{M}^{IT}$ (see Figure 2.4).

Performing the same comparisons but for the datasets with the artificially declined ROIs shows that $\mathbf{M}^{GST}$ in comparison to $\mathbf{M}^{MIL}$ performed equally well as in the situation before with a median of the scalar of 0.98. Comparing $\mathbf{M}^{IT}$ and $\mathbf{M}^{MIL}$ for the artificially declined ROIs led to a drop in the median of the scalar products to 0.5 (see Figure 2.4).

Comparing the datasets with isotropic resolution and artificially declined ROIs shows a deterioration of the results. In case of comparing $\mathbf{M}^{GST}$ to $\mathbf{M}^{MIL}$, the median of the scalar products dropped to 0.95. As before $\mathbf{M}^{IT}$ delivered results not comparable to $\mathbf{M}^{MIL}$ with a median of the scalar products of 0.33 (see Figure 2.4).

Evaluating the influence of the image enhancement process on the comparison of trabecular main direction between $\mathbf{M}^{GST}$ and $\mathbf{M}^{MIL}$ shows that the medians of the scalar products are equal to a significance level of $p < 0.05$. Except for the "weickert"-diffusion which performed slightly worse. The diffusion did not lead to a better prediction using $\mathbf{M}^{IT}$ (see Figure 2.5)

Finally, comparing $\mathbf{M}^{GST}$ to $\mathbf{M}^{MIL}$ for the datasets gained with the normal dose routine and the high dose routine showed that the scalar products tend to be equal to a significance level of $p < 0.05$. Comparing the detection of the trabecular main direction for the datasets generated after explanation of the vertebrae gives

slightly better results. The medians tend to be equal as well to a significance level of $p < 0.05$ (see Figure 2.6).

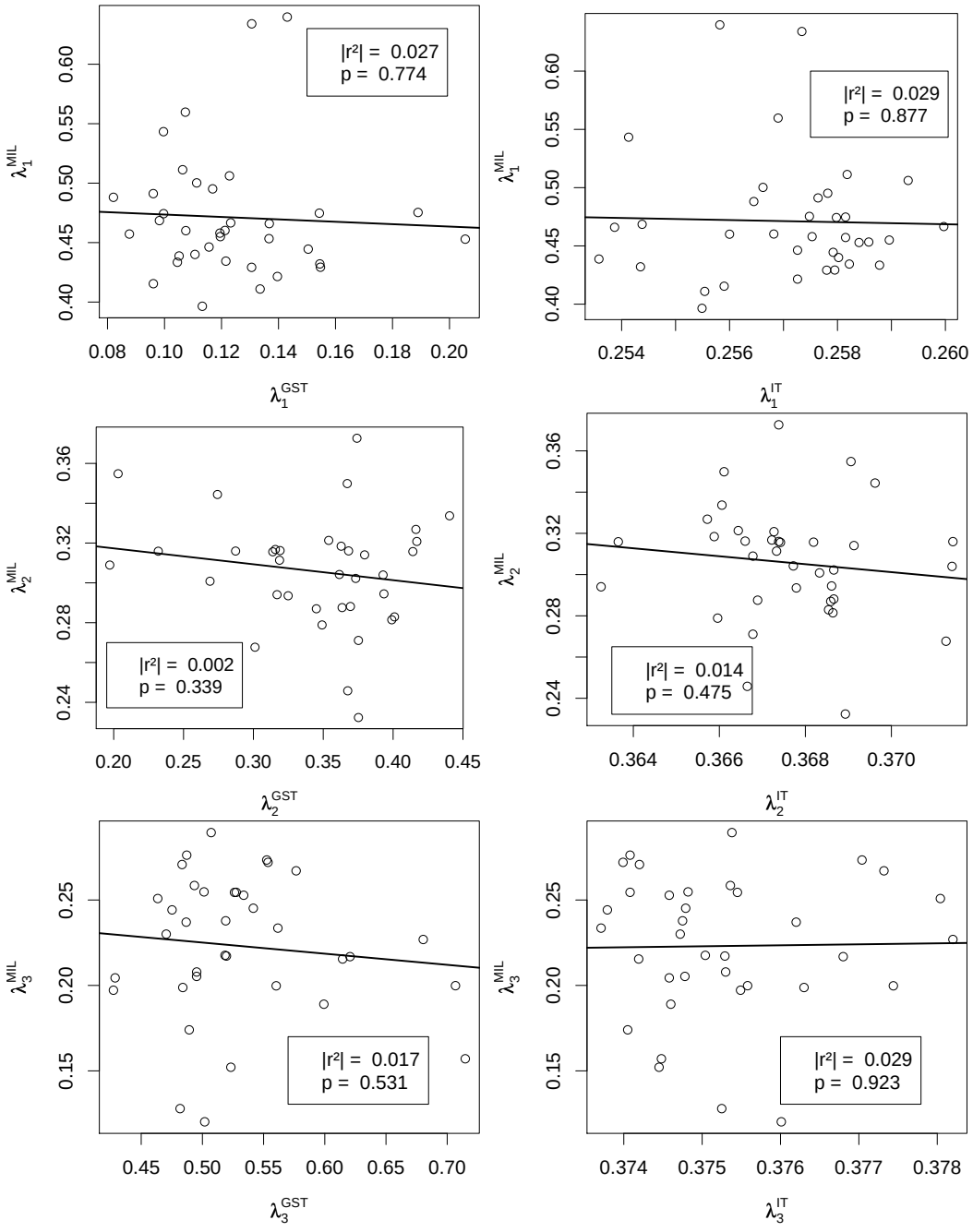

Figure 2.3: Eigenvalues determined with GST (left) and IT (right) on the artificially declined ND datasets compared to those determined using MIL on the µCT datasets.

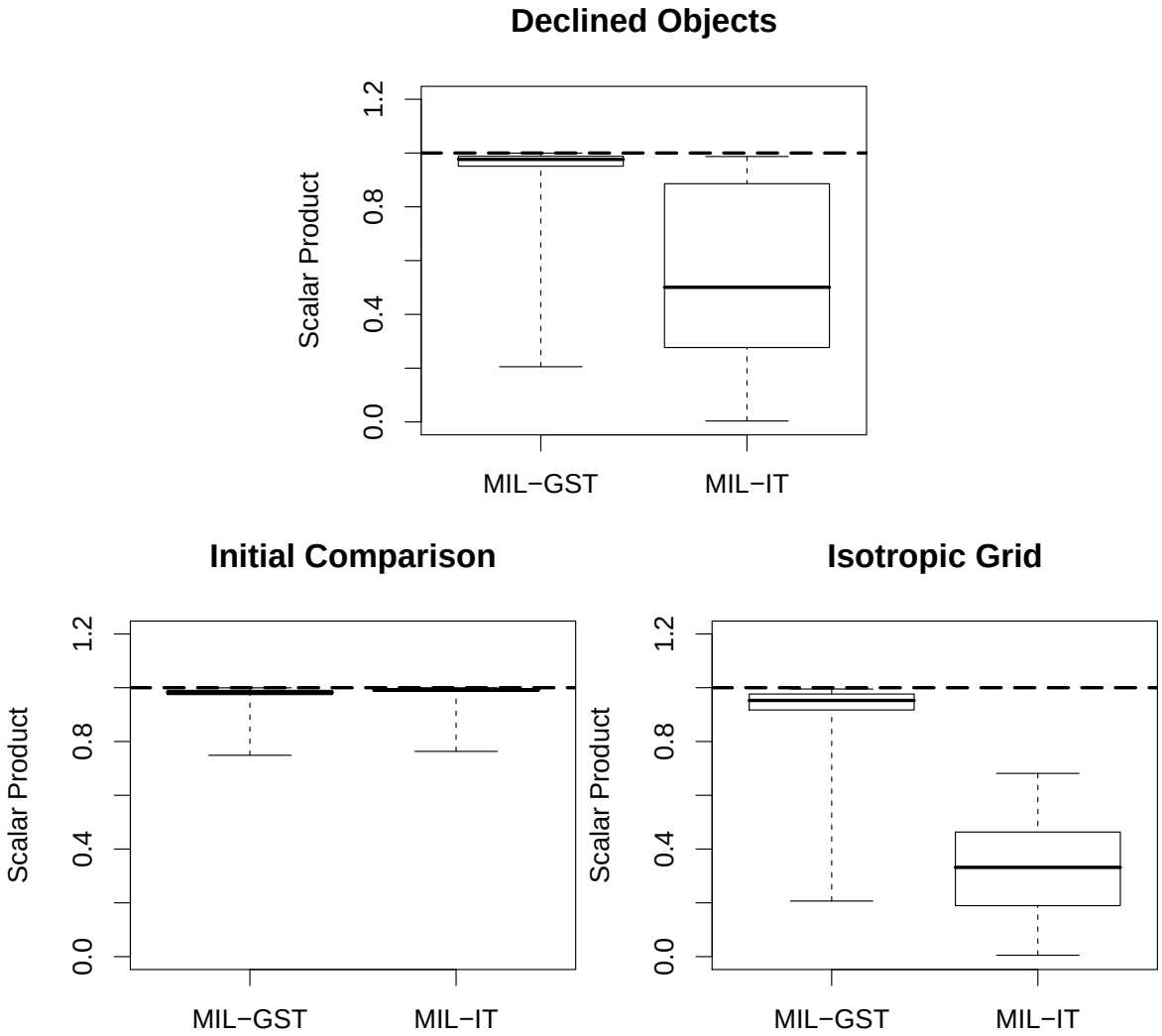

Figure 2.4: Comparing the performance of $\mathbf{M}^{GST}$ and $\mathbf{M}^{IT}$ in the determination of the trabecular main direction for the ND protocol. Top, for the artificially declined datasets. Bottom left, for the initial datasets from the scanner. Bottom right, evaluation of the effect of the grid compression on the artificially declined datasets. Grid lines indicates a scalar product of 1.0.

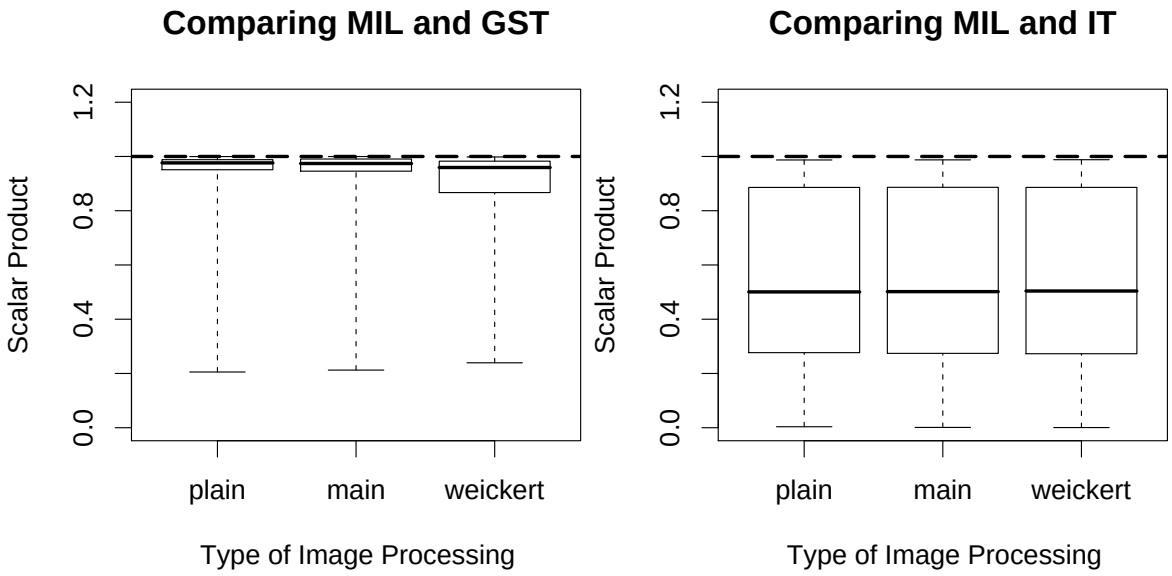

Figure 2.5: Effect of the diffusion process shown on the artificially declined datasets for the ND protocol. Number of timesteps and timestep size was 2. Left, comparing the eigenvector in trabecular main direction between $\mathbf{M}^{MIL}$ and $\mathbf{M}^{GST}$. Right, comparing the eigenvector in trabecular main direction between $\mathbf{M}^{MIL}$ and $\mathbf{M}^{IT}$. The grid line indicates a scalar product of 1.0.

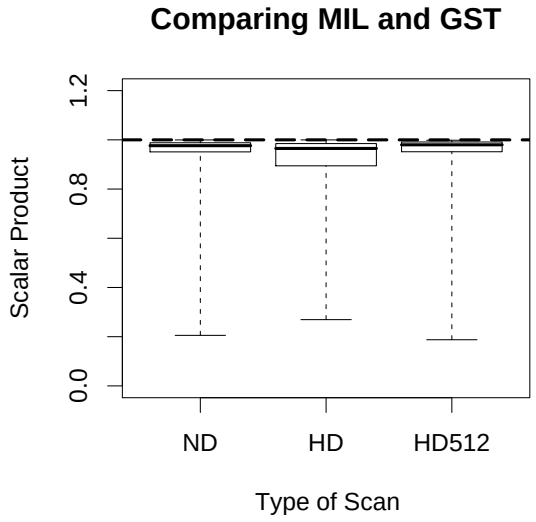

Figure 2.6: Comparing the effect of different dose levels on the determination of trabecular main direction as well as the removal of the surrounding soft tissue (HD512) on the artificially declined data. The grid line indicates a scalar product of 1.0.

2.4 Discussion

A case study on a full body donor was performed to evaluate the possibility of determining a local structure tensor of vertebral trabecular bone comparative to $\mathbf{M}^{MIL}$ in situ. For that $\mathbf{M}^{GST}$ and $\mathbf{M}^{IT}$ were compared to $\mathbf{M}^{MIL}$ through different scan levels. The study could show that it is possible to measure local trabecular main orientation using CT routines from daily clinical practise. The results indicate that the method of choice for in situ datasets is $\mathbf{M}^{GST}$ instead of $\mathbf{M}^{IT}$.

Comparing the predicted eigenvalues in 3D reveals that neither of the alternative structure tensors can predict the eigenvalues determined by $\mathbf{M}^{MIL}$ throughout all scan levels (see Figure 2.3). In contrast, Tabor and Rokita (2007) could show that the eigenvalues of $\mathbf{M}^{MIL}$ can be correlated to those of $\mathbf{M}^{GST}$ but at higher resolutions. The bad performance in the present case could have been due the coarse resolution of the clinical datasets (365 μm) since removal of the surrounding tissue did not lead to any enhancement in the results. Furthermore, the donor could be considered osteoporotic. Thus providing thinner bone with lower attenuation capabilities and therefore weaker structural information as for instance a healthy donor. Thus, the available information was too weak (see Figure 2.7).

Evaluating the prediction of the trabecular main direction, it can be concluded that $\mathbf{M}^{GST}$ is able to determine the direction calculated with $\mathbf{M}^{MIL}$ but from in situ datasets (see Figure 2.4 and Figure 2.7). Subjecting the alternative tensors to artificially declined ROIs and repeating the measurements revealed that $\mathbf{M}^{IT}$ was not able to predict this main direction. This indicates that the measurement method is sensitive to the spacing of the grid and the way the grey values are distributed therein. Introducing an error by compressing the datasets to an isotropic grid did lead to a slight drop in the ability to predict trabecular main direction for $\mathbf{M}^{GST}$. This is presumably due to a dislocation of the structure which was than compared to µCT measurements where the resolution was isotropic.

The bad performance of $\mathbf{M}^{IT}$ could be due to the fact that it measures a mass distribution which is dependent on the distance of the masses instead of an edge distribution as in the case of the other tensors. Thus, not determining the same kind of anisotropy. A possible solution could be the usage of the magnitude or power representation of the datasets in frequency space obtained with a Fast Fourier Transformation (FFT) (Guerin and Elliott, 2006).

The small deviation of the scalar products from one for $\mathbf{M}^{GST}$ could be caused by noise introduced through the image generation process and slight positioning inaccuracies due to the somewhat subjective image alignment process. The outlier present in the results over all is somewhat unexplainable. Justified from the small quartile range it could be due to a severe positioning error in a single measurement.

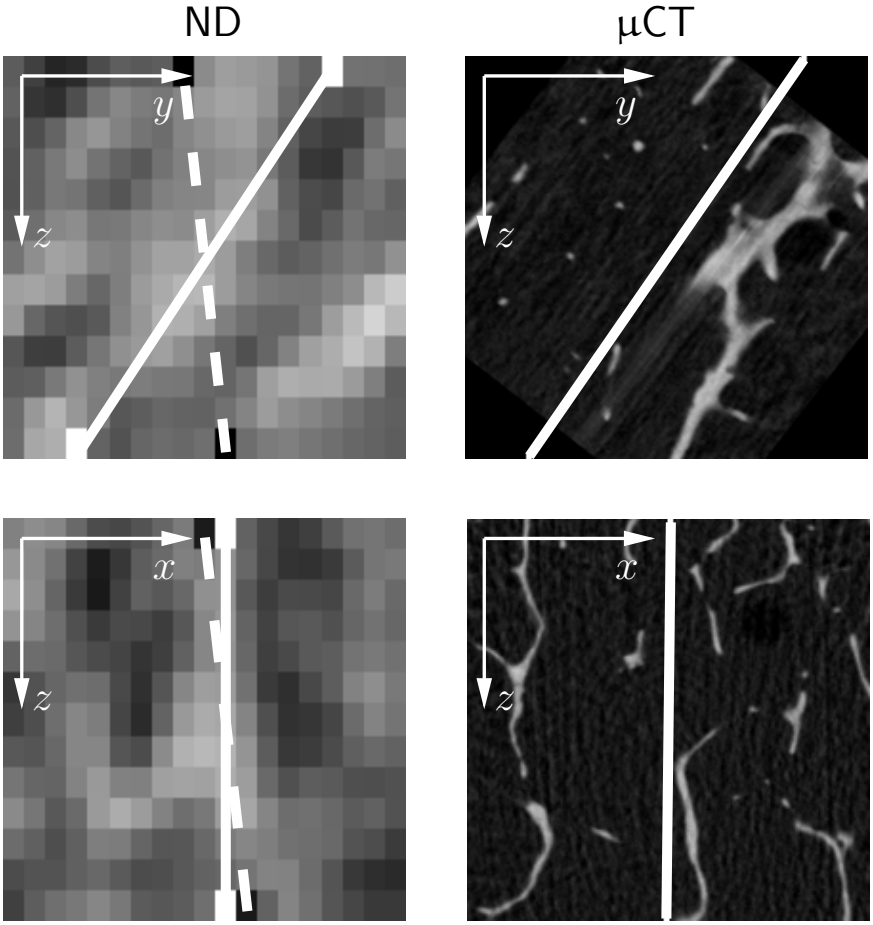

Figure 2.7: Illustration of the detection of the main direction for an exemplary region of interest of the tilted datasets for different scanning protocols. Main direction was determined for the midpoint of the region of interest. In the left figure, the solid line represents the main direction computed with GST and the dashed line the main direction computed with IT. In the right figure, the solid line indicates the main direction computed using MIL. The figures are mid-plain images of the region of interest under consideration.

An interesting finding of the study was that the image enhancement process is unnecessary (see Figure 2.5). The "weickert" diffusion did even worsen the results. Further, these data manipulations did not lead to any enhancement of the predictive power of $\mathbf{M}^{IT}$. The diffusion process is meant to preserve edges. Since the resolution is too low to adequately represent trabecular bone marrow interfaces (Banse et al., 2001) this edge preservation could not evolve properly.

When comparing the artificially declined ROIs through the dose levels (see Figure 2.6) apparently the HD dose performs worse. This is presumably due to a higher amount of noise generated by the higher radiation dose. Removing the soft tissue leads to a clear improvement of the predictions.

Altogether, knowing the trabecular main direction and assuming transverse isotropy of vertebral trabecular bone (Cowin, 2001) with a degree of anisotropy (DA) taken from the literature (Gong et al., 2006) it is possible to construct a fabric tensor (Zysset, 2003) even though the eigenvalues are not correlative to those found by $\mathbf{M}^{MIL}$. With λ_{AX} the eigenvalue in axial direction and λ_{TR} the eigenvalue in transverse direction eigenvalues can be found using a norm.

$$3 = \lambda_{AX} + 2\lambda_{TR} \tag{2.1}$$

$$DA = \frac{\lambda_{AX}}{\lambda_{TR}} \tag{2.2}$$

In the case of transverse isotropy the choice of the transverse eigenvectors is arbitrary. Thus, knowing the eigenvector $\mathbf{v}_{AX}$ in axial direction, the two other vectors $\mathbf{v}_{TR}$ from the eigenproblem can be taken. With the dyadic product $\otimes$, the fabric tensor is than given as

$$\mathbf{M} = \lambda_{TR}\left(\overset{1}{\mathbf{v}}_{TR} \otimes \overset{1}{\mathbf{v}}_{TR}\right) + \lambda_{TR}\left(\overset{2}{\mathbf{v}}_{TR} \otimes \overset{2}{\mathbf{v}}_{TR}\right) + \lambda_{AX}\left(\mathbf{v}_{AX} \otimes \mathbf{v}_{AX}\right) \tag{2.3}$$

A limitation of the study was the small number of 36 measurement points which were obtained from one full body donor. The osteoporotic donor was a trade off. It was advantageous because patient specific FE models would be applied after some standard clinical method, e.g. DEXA, would indicate osteopenia. Hence, structure needs than to be measured from bones showing weaker attenuation. However, the weaker attenuation was presumably the reason for the bad prediction of the eigenvalues (Tabor and Rokita, 2007).

Finally, the classical methods to determine structure such as $\mathbf{M}^{MIL}$ (Odgaard, 1997) are not applicable to clinical datasets. This is because features necessary for the measurements, e.g. bone marrow interfaces, are not visible anymore. This study could show that the measurement of the trabecular main direction is possible in an in situ setting. It was found that the method of choice would be $\mathbf{M}^{GST}$ and not $\mathbf{M}^{IT}$. Unfortunately, neither of the alternative measurement methods could determine the eigenvalues correctly. However, knowing the main direction gives the possibility to construct a specific fabric tensor for the in situ situation at least for transverse isotropy for human vertebral trabecular bone.

Chapter 3

Transverse isotropic elastic properties of dry vertebral trabecular bone matrix

As published in: Wolfram, U., Wilke, H.-J., Zysset, P. K., 2010. Transverse Isotropic Elastic Properties of Vertebral Trabecular Bone Matrix Measured Using Microindentation Under Dry Conditions (Effects of Age, Gender and Vertebral Level). Journal of Mechanics in Medicine and Biology 10 (1), 139 — 150. ★

3.1 Introduction

In the elderly, vertebral bodies have a high risk of fracture, most likely due to osteoporosis (Melton et al., 1992). New treatments such as vertebroplasty are available to avoid such fractures. The surgeon however faces the problem to decide which vertebra needs to be treated. Therefore a robust assessment of the fracture risk on individual vertebrae is essential. In particular for trabecular bone, the assessment of fracture risk relies on macroscopic material properties. Due to the hierarchical nature of bone (Fratzl and Weinkamer, 2007) these parameters can only be derived experimentally with a huge effort whereas others remain indeterminable (Rincón-Kohli and Zysset, 2009).

Micro Finite Element (μFE) models to obtain those material parameters were developed to overcome these difficulties. Isotropic tissue properties were used for the bone phase (Müller and Rüegsegger, 1995; Kabel et al., 1999; Niebur et al., 2000; Rietbergen et al., 2003; Bayraktar et al., 2004a; Chevalier et al., 2007; Verhulp et al., 2008). The results of these simulations are explicitly dependent on the quality of the mechanical properties assigned to the trabeculae (Chevalier et al., 2007; Verhulp et al., 2008; Zysset et al., 1999). Some studies tried to estimate isotropic elastic trabecular properties inverse from macroscopic tests using μFE -models (Niebur et al., 2000; Rietbergen et al., 1995). Since the ultrastructure of trabecular bone indicates non-isotropic material behavior, information about the anisotropy at the micro-level as well as its dependence on the microanatomical testing location could help to improve these models (Fratzl and Weinkamer, 2007; Brennan et al., 2009; Linden et al., 2001).

Depth-sensing indentation techniques (Oliver and Pharr, 1992) provide the possibility of directly determining directional elastic properties of trabecular bone ex-

perimentally. Elastic moduli were determined on transverse sections of trabeculae as well as in the longitudinal direction of tibial cortex (Rho et al., 1997). In subsequent studies two different material directions were tested (Rho et al., 1999; Roy et al., 1999). Nanoindentation was compared to measurements of elastic properties using acoustic microscopy of cortical bone (Turner et al., 1999). The authors found that both techniques gave the same ratio of anisotropy E_{AX}/E_{TR}. For femoral trabecular bone it could be shown that its elastic properties are independent of age and gender at the lamellar-level (Hoffler et al., 2000b). Whether this holds true for vertebral trabecular bone over all vertebral levels on a measurement scale more suitable for µFE modelling remains unclear. A validation study (Hengsberger et al., 2003) proposed a method to determine the relative elastic moduli along two orthogonal directions for bovine compact bone. This method was further developed (Franzoso and Zysset, 2009) to determine an orthotropic elasticity tensor for bone structural units. Subsequently it was used (Mazza et al., 2008) to determine the transverse isotropic elastic properties of trabecular and cortical vertebral bone. A recent review indicated that information about the transverse isotropic properties of vertebral trabecular bone over a broad spectrum of vertebrae is missing (Lewis and Nyman, 2008).

To assure robust reproducibility, the current study was concerned with determining transverse isotropic elastic properties at different microanatomical locations of dried vertebral trabecular bone obtained in different anatomic directions. Since the mechanical competence of trabecular bone could be affected by donor specific factors a particular focus was paid to the influence of the vertebral level, gender of the donor and age of the donor. Hence it was hypothesized, i) indentation modulus (E^{IM}) in axial direction is higher than in transverse direction. ii) E^{IM} in the inner region of trabeculae is higher than at the outside due to an expected higher degree of mineralization. iii) the anatomic orientation of the trabeculae has no effect on E^{IM}. iv) E^{IM} will increase with age due to an expected higher mineralization. v) E^{IM} increases with vertebral level from thoracic to lumbar due to the higher body mass borne and vi) gender has no effect on E^{IM}.

3.2 Materials and Methods

A total of 104 human vertebrae from T1 to L3 of 50 male and 54 female donors with a median age of 65 (21 – 94) years were used. Vertebrae were stored at $-20°C$ immediately after harvest. The vertebrae were randomly assigned to three groups indicating the normal of a cutting plane, cranial-caudal (CC), anterior-posterior (AP) and dexter-sinister (DS). Vertebrae were cleaned of surrounding soft tissue and the posterior structures were removed. Subsequently, a 5 mm thick slice was obtained from the cancellous core using a high precision band saw (Exakt Appa-

ratebau, Norderstedt, Germany). Samples were freed from marrow and defatted. For this, samples were submerged in soapy water in an ultrasound bath (Sonorex, BANDELIN electronic GmbH & Co. KG, Berlin, Germany) and exposed to ultrasound for five minutes at 35 kHz. Afterwards, the bath was left at 40°C for 12 hours (Chevalier et al., 2007). Subsequently, the samples were again exposed to ultrasound for five minutes at 35 kHz, rinsed with water and left to dry over night at room temperature. Specimens were than embedded in epoxy resin (Struers A/S, Ballerup, Denmark) and allowed to cure at room temperature (≈21°C) for 12 hours. After curing the samples were polished with progressive grades of silicon carbide paper (P1000, P1400, P2000, P2500, P4000 – Hermes Schleifmittel GmbH & Co. KG, Hamburg, Germany) and finished with 1 μm diamond paste on a polishing cloth. In-between each grinding step the samples were cleaned from grinding particles in an distilled water ultrasound bath for seven minutes at 35 kHz. Indentations were performed under dry conditions using a depth-sensing nanohardness tester equipped with a pyramidal Berkovich diamond tip (CSM Instruments SA, Peseux, Switzerland). Indentations were driven to a fixed depth of 2.5 μm to average the results over approximately three bone lamellae (Cowin, 2001). Load was applied as a monotonic ramp at 120 $\frac{mN}{min}$ followed by a hold time of 30 s to prevent the influence of creep and an unloading ramp similar to the loading ramp. In a parameter test prior to the measurements, this protocol was found to be a good compromise between accuracy and test duration. Six regions of interest (ROI)

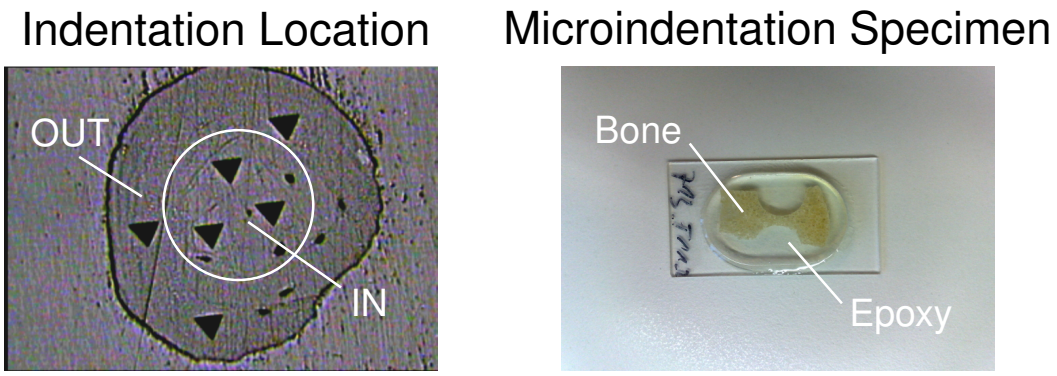

Figure 3.1: Axial and transversal regions of interest for the indentations. Left, testing in axial direction. Right, testing in transverse direction. The triangles are the remaining impressions of the Berkovich indenter.

were defined per sample, three axial (AX) and three transversal (TR). These were additionally divided into an inner (IN) and an outer (OUT) sub-ROI (Figure 4.2). Three indents were performed within each sub-ROI to determine E^{IM} giving 36 indentations per sample. Outer indentations were placed at approximately seven times the testing depth away from the bone-epoxy interface to avoid embedding effects (Hengsberger et al., 2002).

Indentation moduli were defined as in Equation 3.1 with E the Young's modulus and ν the Poisson's ratio of vertebral trabecular bone.

$$E^{IM} = \frac{E}{(1-\nu^2)} \tag{3.1}$$

To quantify and visualize the assumed transverse isotropy in a homogenized stiffness-tensor for dried trabecular bone, an inverse scheme was used (Swadener and Pharr, 2001; Franzoso and Zysset, 2009; Hengsberger et al., 2003). With respect to the trabecular ultrastructure (Rokita et al., 2005) a fabric based representation of the compliance tensor (Zysset, 2003) was used as target tensor. To set up these tensors, indentation moduli were converted to elastic moduli choosing a Poisson's ratio of 0.32 for trabecular bone (Oliver and Pharr, 1992; Hengsberger et al., 2003).

$$\begin{aligned}\mathbb{E}(\mathbf{M}) &= \sum_{i=1}^{3} \frac{1}{\varepsilon_0 m_i^2} (\mathbf{M}_i \otimes \mathbf{M}_i) - \sum_{\substack{i,j=1 \\ i\neq j}}^{3} \frac{\nu_0}{\varepsilon_0 m_i m_j} (\mathbf{M}_i \otimes \mathbf{M}_j) \\ &\quad + \sum_{\substack{i,j=1 \\ i\neq j}}^{3} \frac{\varepsilon_0}{2\mu_0 m_i m_j} (\mathbf{M}_i \,\underline{\overline{\otimes}}\, \mathbf{M}_j)\end{aligned} \tag{3.2}$$

Here, $\mathbf{M}$ denotes the second order fabric tensor, m_i the eigenvalue to its corresponding eigenvector $\mathbf{m}_i$ and $\mathbf{M}_i = \mathbf{m}_i \otimes \mathbf{m}_i$ the tensorial product so that $\mathbf{M} = \sum_i m_i (\mathbf{m}_i \otimes \mathbf{m}_i)$. The eigenvalues are normed so that $\sum m_i = 3$. This ensures that the constants ε_0, ν_0 and μ_0 have the physical meaning of Young's modulus, Poisson's ratio and shear modulus for a virtual linear-elastic, isotropic material (Zysset and Curnier, 1995). Hereby ν_0 is chosen to be 0.32 (Rho et al., 1997; Hengsberger et al., 2003). The tensorial product $\underline{\overline{\otimes}}$ is defined as $\mathbf{A} \,\underline{\overline{\otimes}}\, \mathbf{B} = \frac{1}{2}\left(A_{ik}B_{jl} + A_{il}B_{jk}\right) \mathbf{e}_i \otimes \mathbf{e}_j \otimes \mathbf{e}_k \otimes \mathbf{e}_l$ (Curnier et al., 1995). The virtual shear modulus is assumed to be $\mu_0 = \varepsilon_0 / 2\,(1+\nu_0)$.

A series of those tensors was set up for different given ratios of the fabric eigenvalues $m_3/m_1 \in \{0.1,\ 0.2,\ \ldots 5\}$. These tensors were used as input to the inverse procedure (Franzoso and Zysset, 2009) to compute indentation moduli for a virtual material with $\varepsilon_0 \stackrel{!}{=} 1$ in axial and transversal direction. Since

$$E^{IM}(\lambda, \mathbb{S}) = \lambda E^{IM}(\mathbb{S}), \tag{3.3}$$

the ratios of the measured indentation moduli can be used to determine the correct ratio of indentation moduli from the variation of the tensors to determine ε_0. For that a regressions was perfomed between the ratios of the eigenvalues m_{AX}/m_{TR} and the ratio of the computed indentation moduli $E^{IMc}_{AX}/E^{IMc}_{TR}$. Using the correct

ratio $\tilde{m}_{AX}/\tilde{m}_{TR}$ the compliance tensor in Equation 3.2 was set up with $\epsilon_0 = 1$ to compute a normalised axial indentation modulus $\hat{E}^{IMc}_{AX}$. Since Equation 3.2 gives $E_{AX}/E_{TR} = \epsilon_0 m^2_{AX}/\epsilon_0 m^2_{TR}$ and Equation 3.3 gives $E^{IMc}_{AX}/E^{IMc}_{TR} = E^{IMm}_{AX}/E^{IMm}_{TR}$, ϵ_0 can than be determined from Equation 3.7.

$$\left(\frac{E_{AX}}{E_{TR}}\right)^{\frac{1}{2}} = \frac{m_{AX}}{m_{TR}} = \left(\frac{E^{IMc}_{AX}}{E^{IMc}_{TR}}\right)^{0.80501} \tag{3.4}$$

$$\Rightarrow \frac{\tilde{E}^{IMc}_{AX}}{\tilde{E}^{IMc}_{TR}} = \left(\frac{E_{AX}}{E_{TR}}\right)^{\frac{1}{2\cdot 0.80501}} \tag{3.5}$$

$$\Rightarrow \frac{\tilde{m}_{AX}}{\tilde{m}_{TR}} = \left(\frac{\tilde{E}^{IMc}_{AX}}{\tilde{E}^{IMc}_{TR}}\right)^{0.80501} \tag{3.6}$$

$$\varepsilon_0 = \frac{E^{IMm}_{AX}}{\hat{E}^{IMc}_{AX}} \text{ with } \hat{E}^{IMc}_{AX} = f\left(\epsilon_0, \tilde{m}_{AX}, \tilde{m}_{TR}\right) \tag{3.7}$$

Here, E^{IMm}_{AX} is the measured indentation modulus in axial direction(Franzoso and Zysset, 2009). The constant ε_0 and the eigenvalues m_{AX} and m_{TR} are defined for the inner and outer region. With this, two transverse isotropic stiffness tensors $\mathbb{S}^{IN}$ and $\mathbb{S}^{OUT}$ for the inner and the outer part of a trabecula were defined (Figure 4.8).

Statistical analysis was performed with R (R Foundation for Statistical Computing) (Crawley, 2005). The datasets were freed from outliers defining any measurement below the 0.5^{th} percentile and above the 99.5^{th} percentile as outliers. This leads to a drop out of 38 from 3744 indentations. Prior to statistical analyses a noticeable environmental effect arising through changing humidity (κ) and temperature (τ) was removed from the data. This was done by performing a least square fit of the indentation moduli to a bilinear, affine function:

$$\begin{aligned} E^{IM} &= a\tau + b\kappa + c\tau\kappa + d \\ with\ (a,\ b,\ c,\ d) &= (-1.3260,\ -0.9969,\ 0.0393,\ 46.9248) \end{aligned} \tag{3.8}$$

Subsequently, indentation moduli were adjusted to a reference humidity $\kappa_{ref} = 42\%$ and a reference temperature $\tau_{ref} = 21^{\circ}C$. Age groups were set up so that at least three groups with an equal number of donors could be distinguished. Justified by equal variances ($p >> 0.05$) Analysis of variance (ANOVA) was used for testing.

3.3 Results

The remaining 3706 measurements were used for the analyses. Means of indentation moduli ranged between 11.31 GPa and 15.80 GPa (Table 4.1). Significant differences were found between the axial and transversal material directions ($p < 0.01$). The axial direction showed higher indentation moduli than the transverse directions (Figure 3.2 and Table 4.1). With respect to the inner and outer testing locations (IN, OUT), significant differences were found ($p < 0.01$), with higher indentation moduli for the inner regions (Figure 3.2). The ratios IN/OUT of the indentation moduli ranged in-between 1.05 and 1.12 (Table 4.1).

Table 3.1: The table shows the ratios of the means of the indentation moduli $\pm$ their coefficient of variation for the inner (IN) and peripheral (OUT) regions of interest as well as for indentations on axial (AX) and transverse (TR) cross sections of trabeculae. The line *mean* shows the means of the ratios over the anatomic directions. (See Figure 4.2 for a visualization of the test regions.)

	IN_{AX}/OUT_{AX}	IN_{TR}/OUT_{TR}	AX_{IN}/TR_{IN}	AX_{OUT}/TR_{OUT}
AP	$\frac{15.28(\pm0.19)}{13.74(\pm0.23)} = 1.11$	$\frac{12.63(\pm0.19)}{11.31(\pm0.2)} = 1.12$	$\frac{15.28(\pm0.19)}{12.63(\pm0.19)} = 1.21$	$\frac{13.74(\pm0.23)}{11.31(\pm0.2)} = 1.21$
CC	$\frac{15.80(\pm0.18)}{15.05(\pm0.18)} = 1.05$	$\frac{12.44(\pm0.17)}{11.84(\pm0.2)} = 1.05$	$\frac{15.80(\pm0.18)}{12.44(\pm0.17)} = 1.27$	$\frac{15.05(\pm0.18)}{11.84(\pm0.2)} = 1.27$
DS	$\frac{14.52(\pm0.21)}{13.48(\pm0.23)} = 1.08$	$\frac{12.22(\pm0.18)}{11.39(\pm0.19)} = 1.07$	$\frac{14.52(\pm0.21)}{12.22(\pm0.18)} = 1.19$	$\frac{13.48(\pm0.23)}{11.39(\pm0.19)} = 1.18$
mean	1.08	1.08	1.22	1.22

The anatomic direction showed significant differences in the moduli. Here, the cranial-caudal direction showed the highest stiffness $E^{IM}_{CC} = 13.80\ GPa$ $(p < 0.01)$ (Figure 3.2). The factor combination anatomic versus material direction revealed significant differences for the cranial-caudal direction in the transverse material direction $(p < 0.01)$ but not for dexter-sinister and anterior-posterior (Figure 3.2). Removing the data in the cranial-caudal direction from the analysis and re-performing ANOVA led to a moderate difference between stiffness in the remaining anatomic directions $E^{IM}_{AP} = 13.24\ GPa$ and $E^{IM}_{DS} = 12.90\ GPa$. The other factors remained significantly different $p < 0.01$ (Figure 3.2).

Gender did not show a significant influence. There was no difference in the indentation moduli between males and females $(p > 0.05)$. The factors material direction, indentation location and anatomic direction remained significantly different $p < 0.01$ after the categorical variable gender was removed from the ANOVA (Figure 3.3).

Evaluating the indentation results with regard to age did not show any influence. There was no significant difference between the defined age groups $p > 0.5$ (Figure 3.4).

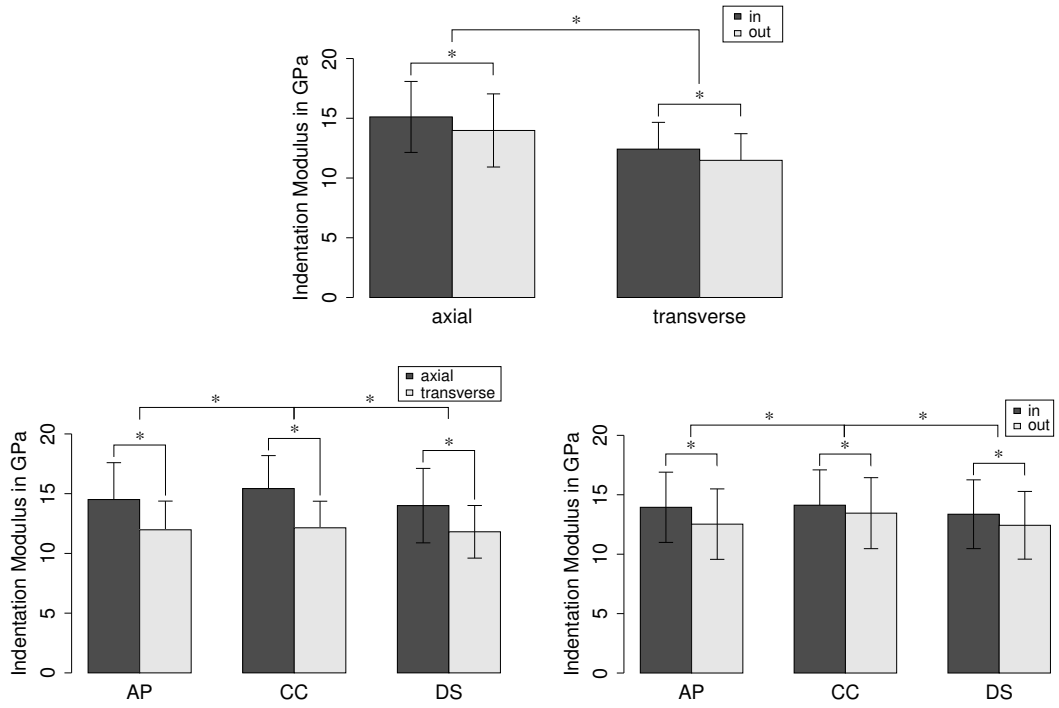

Figure 3.2: Indentation moduli for the different test regions as depicted in Figure 4.2. Top, stiffness is higher when testing on axial than on transverse cross-sections. Furthermore, stiffness is higher when testing in the core (in) compared to the periphery (out) of trabeculae. Bottom line, moderate differences were detected when testing in different anatomical directions for both the material directions (axial – transverse) and the micro-anatomicals location (in – out). The figure depicts means of elastic moduli in GPa. The error bars denote $\pm$ 1 standard deviation and the asterisk marks significance to $p < 0.05$.

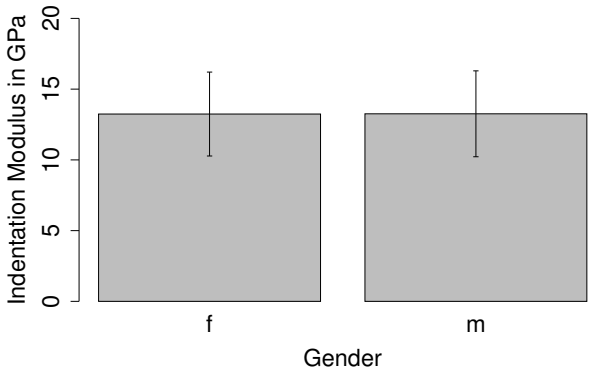

Figure 3.3: No dependence on gender was found for the indentation modulus of vertebral trabecular bone matrix. The figure shows means of indentation moduli for both male (m) and female (f). The error bars denote $\pm$ 1 standard deviation.

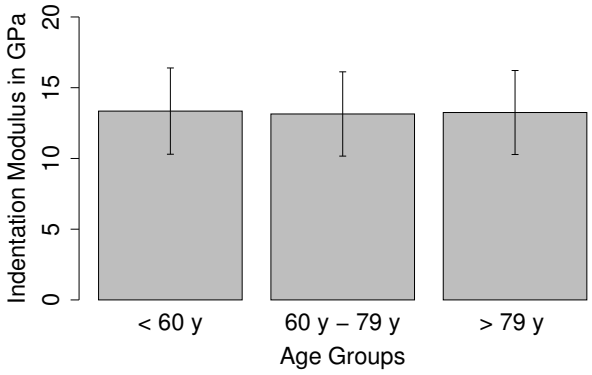

Figure 3.4: Indentation modulus of vertebral trabecular bone matrix is independent of age as measured for three age groups. The figure shows means of the indentation moduli for three age groups having a balanced number of donors. The error bars denote ± 1 standard deviation.

The vertebral level showed a weak but insignificant correlation ($p = 0.073$ and $r^2 \approx 0.17$) with the indentation moduli (Figure 4.5). This could indicate that trabecular bone in the lumbar levels is stiffer than the thoracic levels.

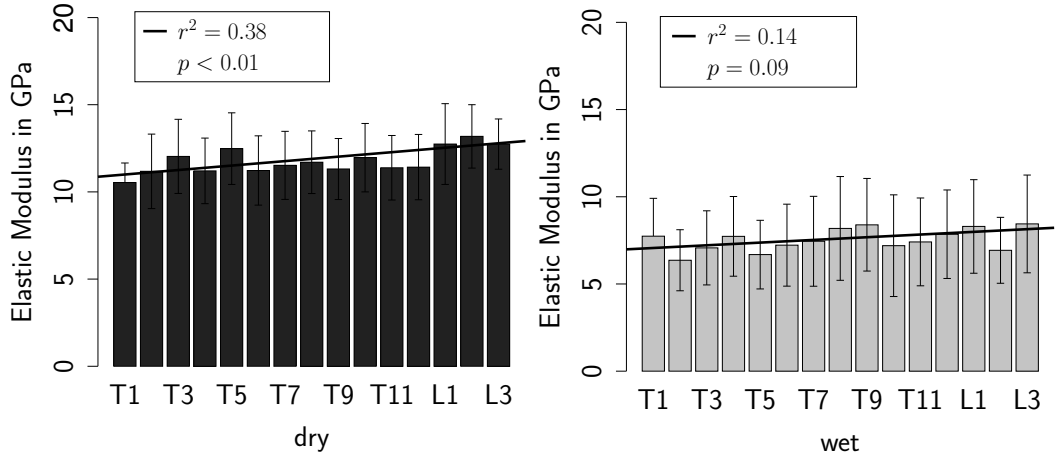

Figure 3.5: A weak but insignificant correlation between indentation modulus and vertebral level from the first thoracic (T1) to the third lumbar (L3) vertebra could indicate a dependence of stiffness of vertebral trabecular bone matrix on the vertebral level. The figure shows means of indentation moduli of each vertebral level. The error bars denote ± 1 standard deviation.

The mean indentation moduli in axial and transverse material direction were used to quantified and visualize the assumed transverse isotropy. Differences are noticeable in two stiffness tensors for the inner and outer trabecular regions (Figure 4.8).

$\mathbb{S}^{\text{dry}}$ $\mathbb{S}^{\text{wet}}$

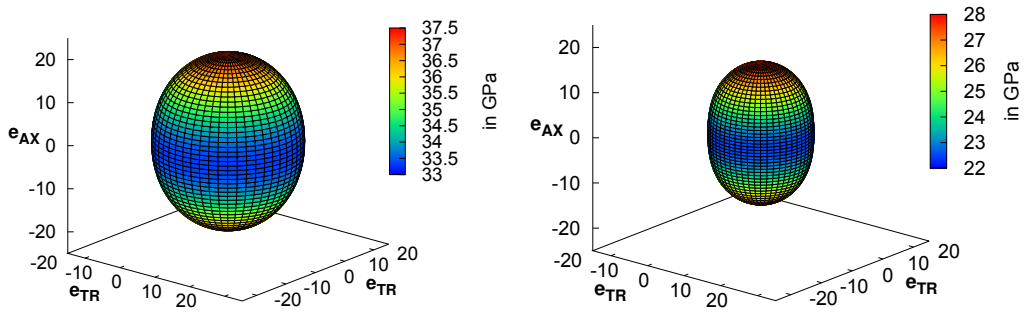

$$\begin{pmatrix} 16.82 & 7.91 & 8.62 & 0 & 0 & 0 \\ 7.91 & 16.82 & 8.62 & 0 & 0 & 0 \\ 8.62 & 8.62 & 19.94 & 0 & 0 & 0 \\ 0 & 0 & 0 & 9.70 & 0 & 0 \\ 0 & 0 & 0 & 0 & 9.70 & 0 \\ 0 & 0 & 0 & 0 & 0 & 8.90 \end{pmatrix} \qquad \begin{pmatrix} 11.13 & 5.24 & 6.15 & 0 & 0 & 0 \\ 5.24 & 11.13 & 6.15 & 0 & 0 & 0 \\ 6.15 & 6.15 & 15.37 & 0 & 0 & 0 \\ 0 & 0 & 0 & 6.92 & 0 & 0 \\ 0 & 0 & 0 & 0 & 6.92 & 0 \\ 0 & 0 & 0 & 0 & 0 & 5.89 \end{pmatrix}$$

Figure 3.6: Visualization of the two constructed stiffness tensors. To set up these stiffness tensors, indentation moduli were converted to elastic moduli assuming a Poisson's ratio of 0.32[27 12]. Left the inner trabecular regions. Right the outer trabecular regions. The shape depicts the elongation modulus and the color encodes the bulk modulus[11].

3.4 Discussion

In agreement with hypothesis i), it was found that vertebral trabeculae exert a 1.18 to 1.27 times higher stiffness in the axial than in the transverse direction. Regarding hypothesis ii), it could be shown that the stiffness in the inner region of a trabecula is 1.05 to 1.12 times higher than at its periphery. Unexpectedly, a significant difference in the stiffnesses of the samples obtained in the different anatomic directions was found. This disagrees with hypothesis iii). In disagreement to hypothesis iv), age had no effect on the indentation moduli. The vertebral level did not significantly influence the indentation moduli as proposed in hypothesis v). Finally, gender did not show any effect on the indentation results confirming hypothesis vi).

The overall mean value for the moduli found in this study was higher than values given by Hoffler et al. (2000a) but lower than those given by Rho et al. (1997, 1999). This may be due to environmental factors such as wet indentation, different preparation and testing protocols as well as different indentation depths.

However, our results lay in-between those found for wet indentation (Hoffler et al., 2000a) and those for dry indented but alcohol dehydrated specimens (Rho et al., 1997, 1999) indicating that our results were in an acceptable range.

The ratios of anisotropy E^{IM}_{AX}/E^{IM}_{TR} for trabecular bone are in good agreement with Rho et al. (1999) especially for the cranial-caudal direction. This ratio was found to be lower for the samples cut in the transverse anatomic directions. In contrast, the ratios of moduli between the inner and outer regions E^{IM}_{IN}/E^{IM}_{OUT} were higher in the samples obtained in the transverse anatomic direction than in the cranial-caudal direction. However, both ratios E^{IM}_{AX}/E^{IM}_{TR} and E^{IM}_{IN}/E^{IM}_{OUT} were equal for AX/TR and IN/OUT respectively when averaging over the anatomic directions (Table 4.1). Altogether the ratios E^{IM}_{IN}/E^{IM}_{OUT} were lower than E^{IM}_{AX}/E^{IM}_{TR} indicating that the anisotropy is more important than the inhomogeneous mineralization caused by the remodelling areas (Figure 3.2).

Unexpectedly, a higher stiffness was found in samples extracted from the cranial-caudal direction. Even though significant, the mean differences are moderate $E^{IM}_{AP} = 13.24\ GPa$, $E^{IM}_{CC} = 13.79 GPa$, $E^{IM}_{DS} = 12.90\ GPa$. Judging from the axial indentations in all three anatomic directions the difference in the samples extracted in the transverse directions are negligible. The higher stiffness in the cranial-caudal direction could be due to a higher mineralization in this direction. However, since the trabecular grid in a vertebral body is not perfectly orthogonal, this difference is most likely introduced through better aligned sections of the trabeculae in the cranial-caudal direction giving better sections. Because of this the indentations in CC are more axially aligned than in the samples from the transverse directions. This presumably leads to slightly higher indentation moduli there. The difference in stiffness was less obvious when regarding solely the indents on the transverse trabecula. This may be due to the fact, that the possible misalignment is not as severe as in the axial case. Furthermore, even though care was taken to visually identify the transverse middle cross section of a trabecula errors in identifying trabeculae with a cross section exactly in the middle could have occurred. If not in the middle, the possibility of indentations placed more towards the periphery of the sectioned trabecula arises. Thus, slight errors in determining the same cross section for all trabeculae could have caused greater noise in the results.

Gender and age did not show a significant difference which corroborates the findings in femoral trabecular bone (Hoffler et al., 2000b). Thus, Hypothesis iv) can be rejected and v) can be accepted. The lack of an effect of age may indicate that the alteration of macroscopic mechanical competence of vertebral trabecular bone with age (Karlsson et al., 2005) is due to structural changes such as thinning and not accompanied by decreasing material properties of the trabecular tissue at the micro-level. Presumably, the remodelling site is moved towards the center, keeping the overall ratio of material composition the same. The lack of a gender

effect suggests that vertebral trabecular bone composition is equal for males and females at the micro-level.

The vertebral level only weakly explained the variation in modulus ($r^2 \approx 0.17$, $p = 0.073$). However, the trend could indicate that trabecular tissue is stiffer in lumbar vertebrae. The higher mineralization and thus the higher stiffness could be due to a constant trabecular thickness throughout the thoracal and lumbar vertebral levels (Banse et al., 2001).

The fabric based representation of the stiffness tensor used to quantify and visualize the transverse isotropy was justified by the trabecular ultrastructure. This consists of a mineralized collagen network with a preferential texture along the longitudinal axis of a trabecula (Weiner et al., 1997; Jaschouz et al., 2003; Rokita et al., 2005). Thus allowing the fabric based stiffness representation.

The chosen embedding techniques should not have had any influence on the results for the dry indentation, since the epoxy cures within 12 hours. Thus, no infiltration in a histological sense should have occurred (Mittra et al., 2006). However, to avoid possible influences of the bone-epoxy interface, outer indentations were placed so that the indents were about seven times the indentation depth away from the boundary (Hengsberger et al., 2002). This is approximately the diameter of the projected area of contact of the Berkovich indenter used.

Regarding the absolute stiffness values with respect to physiologic results, the major limitation of this study were the dry indentation conditions. Since collagen tends to shrink when dried, changed material properties could be expected. However, it is unclear whether rehydration would have an impact on the anisotropy or on the different results from inner and outer ROIs. Regarding the other factors, such as the influence of age, gender and vertebral level, it is also of interest whether these would change when testing wet. It is usual to perform the indentation tests rehydrated to obtain results under more physiological conditions (Bushby et al., 2004). However, we aimed for quantifying anisotropy rather than physiological stiffness values. The great advantage of testing under dry conditions however is the good reproducibility of the tests as indicated by the low coefficients of variation in Table 4.1. These do as well reflect the sufficient number of specimens used for the statistics (Sachs, 2006).

This study provided qualitative and quantitative insights into the transverse isotropic material properties of vertebral trabecular bone with a particular focus on age, gender, vertebral level and anatomic direction. Transverse isotropy could be quantified and visualized in terms of stiffness tensors for the inner and the outer region of trabeculae. In particular, the quantitative results could help to improve numerical models of trabecular bone to determine macroscopic mechanical properties using numerical simulations.

Chapter 4

Rehydration affects the elastic properties of vertebral trabecular bone

As published in: Wolfram, U., Wilke, H.-J., Zysset, P. K., 2010. Rehydration of Vertebral Trabecular Bone: Influences on its Anisotropy, its Stiffness and the Indentation Work with a View to Age, Gender and Vertebral Level. Bone 46 (2), 348 – 354. ★

4.1 Introduction

Vertebral bodies show a high risk of fracture in the elderly which is most likely due to osteoporosis (Melton et al., 1992). A more sophisticated diagnosis could help to deploy treatments more specifically which in turn could possibly prevent those vertebral fractures. This, however, necessitates a robust assessment of the fracture risk of single vertebrae. A major part of the vertebral load is borne by the cancellous core. Thus, its macroscopic material properties play an important role in the assessment of fracture risk. Due to the hierarchical nature of bone (Rho et al., 1998), this macroscopic material behaviour of the cancellous core is dependent on the micromechanical properties of the contained trabeculae (Zysset et al., 1999). Their micromechanical properties are in turn dependent on their ultrastructure which shows a preferential texture along the longitudinal axis of a trabecula (Jaschouz et al., 2003; Rokita et al., 2005; Weiner et al., 1997). Furthermore, these orientation dependent micromechanical properties are affected by a constant remodelling process on the trabecular surface with a slowly continuing mineralisation (Birkenhäger-Frenkel et al., 1993) after remodelling. Since the trabecular core is unaffected, this causes a nonuniform mineral distribution over the trabecular cross-section (Linden et al., 2001; Roschger et al., 2008). Thus, the trabecular material properties vary over its cross-section and should be considered at least linear elastic transverse isotropic along the longitudinal direction of the trabecula. However, trabeculae are often regarded as homogeneous, isotropic and linear elastic in the literature (Bayraktar et al., 2004a; Chevalier et al., 2007; Kabel et al., 1999; Niebur et al., 2000; Rietbergen et al., 2003, 1995; Verhulp et al., 2008). This is probably due to the fact that the aforementioned nonuniform texture necessitates a high spatial resolution to assess the degree of mineralisation and the anisotropic material properties.

Such a high spatial resolution can be provided by depth-sensing indentation techniques (Oliver and Pharr, 1992) which give the possibility to determine directional elastic properties of trabecular bone directly. Using these techniques the elastic properties on longitudinal and transverse sections of alcohol dehydrated trabecular bone and tibial cortex were determined (Rho et al., 1999, 1997; Roy et al., 1999). Higher elastic moduli where found for the longitudinal direction. A study comparing acoustic microscopy and nanoindentation (Turner et al., 1999) found that both measurements gave the same ratio of elastic moduli measured in axial direction (E_{AX}) to elastic moduli measured in transverse direction (E_{TR}) but that E measured using acoustic microscopy was 20% lower. The authors argued that this was due to the fact that the specimens for acoustic microscopy were allowed to rehydrate prior to testing. This was corroborated when comparing nanoindentation under wet and dry testing conditions (Hengsberger et al., 2002; Hoffler et al., 2005).

A validation study (Hengsberger et al., 2003) proposed a method which allows the determination of elastic moduli along two orthogonal axes. The procedure was further developed to determine an orthotropic elasticity tensor for secondary osteons (Franzoso and Zysset, 2009). This scheme was used (Wolfram et al., 2010b) to determine transverse isotropic elasticity tensors for dried trabecular bone both for its centre and its periphery. This confirmed findings on sheep (Brennan et al., 2009) regarding different elastic moduli between centre and periphery. Furthermore, it was confirmed that the elastic moduli of dried vertebral trabecular bone do not depend on age and gender which was found previously for femoral trabecular bone (Hoffler et al., 2000b).

A recent review on nanoindentation (Lewis and Nyman, 2008) points out that the state of hydration of the specimens is crucial to obtain more physiological results. Clearly, results from dried vertebral trabecular bone are far off any physiological meaning. This review indicates furthermore a need for more information about the anisotropic elastic properties of vertebral trabecular bone over a broad spectrum of vertebrae obtained under more physiologic, i. e. wet, indentation conditions. The effect of rehydration on the anisotropy and the indentation work of vertebral trabecular bone is unclear. Besides this, the absolute values for the elastic moduli and the indentation work for vertebral trabecular bone obtained under wet indentation conditions and the impact of rehydration on factors such as donor age, gender and vertebral level could be of interest.

Thus, the present study aims to investigate the effect of rehydration in a conjoined statistics comparing results from dry and wet indentation. Furthermore, more physiological elastic moduli for human vertebral trabecular bone as well as the indentation work for a certain indentation protocol are provided. It was hypothesised that, i) E will be lowered by rehydration. ii) the ratio of E obtained in

axial to E obtained in transverse indentation direction will increase under wet conditions due to different swelling modes of the cross-sections. iii) It is expected that a lower mineralisation and therefore a higher collagen content leads to a greater impact of the rehydration. Thus, the ratio between E measured in the core and the periphery of trabeculae will increase under wet conditions. Rehydration will not change the effects of iv) gender, v) age, vi) vertebral level and vii) anatomic direction on E in comparison to tests under dry conditions. viii) The elastic and dissipated indentation work W will be affected qualitatively in a similar fashion than E.

4.2 Material and Methods

Test specimens were obtained from a set of 104 human vertebrae. This set consisted of 50 male and 54 female vertebrae with a mean age of 65 (range 21 – 94) and vertebral levels from T1 to L3. The vertebrae were randomly assigned to three anatomical testing groups indicating the normal of a cutting plane, cranial-caudal (CC), anterior-posterior (AP) and dexter-sinister (DS) and cleaned from surrounding soft tissue. To compare the effects of rehydration on the indentation results, raw dry indentation data was taken from a previous study (Wolfram et al., 2010b) on samples obtained from the same set of vertebrae which underwent the same preparation protocol. For the wet indentations, a second 5 mm thick slice was cut per vertebra with a high precision band saw (Exakt Apparatebau, Norderstedt, Germany). The samples were submerged in soap water in an ultrasound bath (Sonorex, BANDELIN electronic GmbH & Co. KG, Berlin, Germany) and exposed to ultrasound for five minutes at 35 kHz. The bath was left at $40°C$ for 12 h (Chevalier et al., 2007). Afterwards, the samples were exposed to ultrasound at 35 kHz for five minutes, rinsed with water and left for drying over night. Specimens were then embedded in epoxy resin (Struers A/S, Ballerup, Denmark) and allowed to cure at room temperature ($\approx 21°C$) for 12 h. After curing, the samples were polished with progressive grades of silicon carbide paper (P1000, P1400, P2000, P2500, P4000 – Hermes Schleifmittel GmbH & Co. KG, Hamburg, Germany) and finished with 1 µm diamond paste on a polishing cloth. Between each grinding step the samples were cleaned in a distilled water ultrasound bath for seven minutes at 35 kHz. Prior to testing, specimens were rehydrated for 1.5 h in 99% saturated Hank's Balanced Salt Solution (HBSS). For the wet tests the samples were submerged in HBSS so that they were covered by an approximately 3 mm thick layer of HBSS. Wet indentation was performed using a depth-sensing nanohardness tester equipped with a pyramidal Berkovich diamond tip and a wet cell (CSM Instruments SA, Peseux, Switzerland, Figure 4.1). Indentations were driven to a depth of 2.5 µm. Load was applied as a monotonic ramp at 120 $\frac{\mathrm{mN}}{\mathrm{min}}$ followed by a

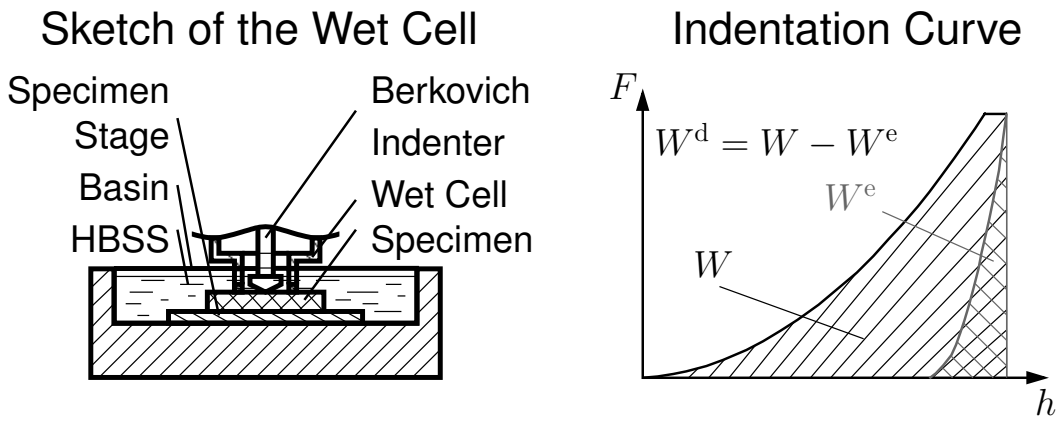

Figure 4.1: The figure shows a sketch of the used wet cell (left) and illustrates the determination of the indentation work (right) with W total energy, W^e elastic and W^d dissipated energy.

hold time of 30 s to prevent the influence of creep and an unloading ramp similar to the loading ramp. Six regions of interest (ROI) were defined, three in axial (AX) and three in transverse indentation direction (TR). These were further divided in an inner (IN) and an outer (OUT) subregion. Per subregion, three indents were performed to determine the elastic modulus E and the indentation work W giving 36 indentations per sample (Figure 4.2). Outer indents were placed at approximately seven times the testing depth away from the bone-epoxy interface to avoid embedding effects (Hengsberger et al., 2002; Mittra et al., 2006).

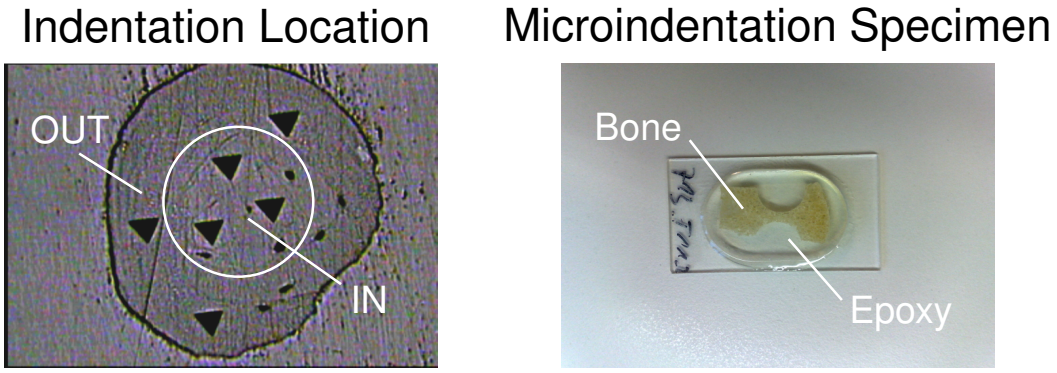

Figure 4.2: The figure shows the regions of interest (ROI) for the indentation tests. A ROI in axial indentation direction is depicted on the left and a ROI in transversal indentation direction on the right.

Indentation work (W) was determined numerically from the force displacement curves using a trapezoidal integration rule (Kiusalaas, 2005). Integration was per-

formed along the loading part up to the end of the hold time and the elastic energy (W^{e}) was obtained by integrating over the unloading part. Dissipated energy (W^{d}) was derived by subtracting W^{e} from W (Figure 4.1).

To quantify and visualise the assumed transverse isotropy in a homogenised stiffness-tensor, an inverse scheme was used (Swadener and Pharr, 2001; Franzoso and Zysset, 2009; Hengsberger et al., 2003). With respect to the trabecular ultrastructure (Rokita et al., 2005) a fabric based representation of the compliance tensor (Zysset, 2003) was used as target tensor choosing a Poisson's ratio of 0.32 for trabecular bone (Oliver and Pharr, 1992; Hengsberger et al., 2003). Two transverse isotropic stiffness-tensors $\mathbb{S}^{\mathrm{wet}}$ and $\mathbb{S}^{\mathrm{dry}}$ for wet and dry indentation conditions were defined (Figure 4.1).

Statistical analysis was performed with R (R Foundation for Statistical Computing, Crawley (2005)). Contrary to the study which delivered the raw data under dry indentation conditions, datasets were freed from outliers defining any measurement with a modulus below the 2.5^{th} percentile and above the 97.5^{th} percentile as outliers to obtain a robust comparison. The results for dry indentations were recomputed for comparison. Age groups were set up so that three groups with a balanced amount of donors could be distinguished. Justified by equal variances ($p \gg 0.05$), Analysis of Variance (ANOVA) was used for testing and a significance level of $p = 0.05$ was chosen.

4.3 Results

All together 7488 indentations were performed of which 7114 were used for the comparison of wet and dry measurements after removing outliers. Means of elastic moduli measured in wet indentation lay between 6.59 GPa and 12.04 GPa and were significantly lower than those found for dry indentation ($p < 0.05$). Wet mean elastic modulus E^{wet} was $\approx 29\%$ lower than dry mean elastic modulus E^{dry}. Coefficients of variation were on average 1.69 times higher under wet compared to dry indentation conditions (Table 4.1, Figure 4.3).

Significant differences were found between tests in axial and transverse indentation directions ($p < 0.05$) before and after rehydration. Elastic moduli in axial were higher than in transverse indentation direction with increased ratios of AX/TR for wet indentation conditions (Figure 4.3). The ratios AX/TR ranged from 1.16 to 1.23 for dry and 1.24 to 1.56 for wet indentations (Table 4.1). Elastic moduli from the inner and outer testing locations showed significant differences for dry and wet indentation conditions ($p < 0.05$). The elastic moduli in the inner region were higher for both indentation conditions (Figure 4.3). The ratios of IN/OUT ranged from 1.03 to 1.08 for dry and 1.09 to 1.29 for wet indentation conditions (Table 4.1). In dry testing conditions the ratios of elastic moduli $\mathrm{IN_{AX}}/\mathrm{OUT_{AX}}$ and $\mathrm{IN_{TR}}/\mathrm{OUT_{TR}}$

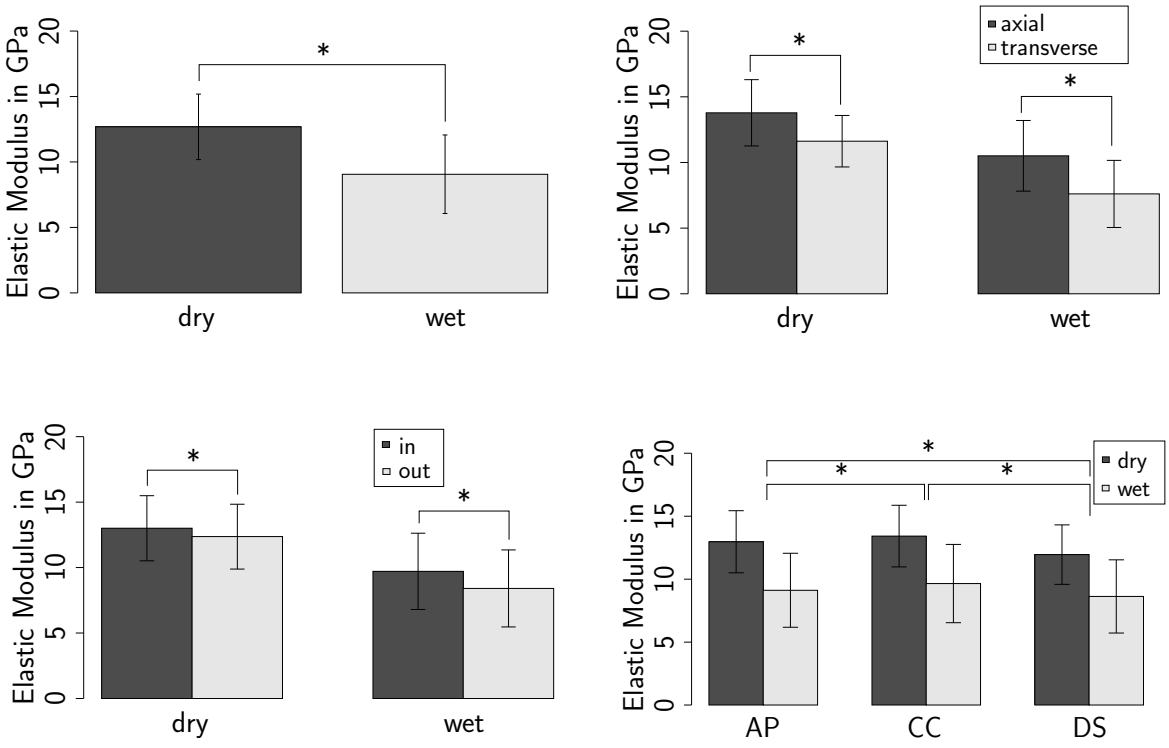

Figure 4.3: Means of elastic moduli for the two testing conditions "wet" and "dry" and the different indentation locations as shown in Figure 4.2. Top left, overall means of elastic moduli in dry and wet indentation. Top right, combination of material direction and testing condition against elastic modulus. Bottom left, combination of testing condition and indentation location against elastic modulus. Bottom right, combination of testing condition and anatomic direction against elastic modulus. The whiskers denote ± 1 standard deviation.

stayed the same when averaging over the anatomic directions. So do the ratios AX_{IN}/TR_{IN} and AX_{OUT}/TR_{OUT}. For wet testing conditions, these ratios were all different and were increasing from IN_{AX}/OUT_{AX} to IN_{TR}/OUT_{TR} to AX_{IN}/TR_{IN} to AX_{OUT}/TR_{OUT} (Table 4.1).

The differences in the anatomic directions persisted in wet indentation ($p < 0.05$) in a similar fashion than in dry indentation with the highest stiffness in cranial-caudal direction $E_{CC} = 9.65$ GPa (Figure 4.3).

Rehydration of the specimens did not affect the independence of the elastic moduli on gender ($p_{wet} = 0.54,\ p_{dry} = 0.13$). The same held true for age (Figure 4.4). No difference could be found between the age groups before and after rehydration ($p_{wet} = 0.28,\ p_{dry} = 0.41$).

The weak but significant correlation between elastic moduli and vertebral level found for dry indentations $\left(p_{dry} = 0.009,\ r^2_{dry} = 0.38\right)$ was lower in the wet case

Table 4.1: The table compares the results of wet (top) and dry (bottom) indentations. Elastic moduli are given in GPa. Ratios of the means of the elastic moduli for the inner (IN) and peripheral (OUT) indentation regions as well as for indents in axial (AX) and in transverse indentation direction (TR) are shown. The line "mean" indicates the means of the ratios over the anatomic directions. See Figure 4.2 for a sketch of the indentation locations and Figure 4.8 for the stiffness-tensors constructed with these results.

Wet Indentation:

	IN_{AX}/OUT_{AX}	IN_{TR}/OUT_{TR}	AX_{IN}/TR_{IN}	AX_{OUT}/TR_{OUT}
AP	$\frac{10.99(\pm0.23)}{9.76(\pm0.27)} = 1.13$	$\frac{8.84(\pm0.3)}{6.87(\pm0.34)} = 1.29$	$\frac{10.99(\pm0.23)}{8.84(\pm0.30)} = 1.24$	$\frac{9.76(\pm0.27)}{6.87(\pm0.34)} = 1.42$
CC	$\frac{12.04(\pm0.19)}{11.01(\pm0.21)} = 1.09$	$\frac{8.54(\pm0.31)}{7.07(\pm0.34)} = 1.21$	$\frac{12.04(\pm0.19)}{8.54(\pm0.31)} = 1.41$	$\frac{11.01(\pm0.21)}{7.07(\pm0.34)} = 1.56$
DS	$\frac{10.53(\pm0.25)}{9.43(\pm0.29)} = 1.12$	$\frac{7.88(\pm0.31)}{6.59(\pm0.32)} = 1.20$	$\frac{10.53(\pm0.25)}{7.88(\pm0.31)} = 1.34$	$\frac{9.43(\pm0.29)}{6.59(\pm0.32)} = 1.43$
mean	1.11	1.23	1.33	1.47

Dry Indentation:

	IN_{AX}/OUT_{AX}	IN_{TR}/OUT_{TR}	AX_{IN}/TR_{IN}	AX_{OUT}/TR_{OUT}
AP	$\frac{14.48(\pm0.16)}{13.49(\pm0.19)} = 1.07$	$\frac{12.46(\pm0.16)}{11.51(\pm0.16)} = 1.08$	$\frac{14.48(\pm0.16)}{12.46(\pm0.16)} = 1.16$	$\frac{13.49(\pm0.19)}{11.51(\pm0.16)} = 1.17$
CC	$\frac{15.00(\pm0.14)}{14.60(\pm0.15)} = 1.03$	$\frac{12.36(\pm0.15)}{11.86(\pm0.17)} = 1.04$	$\frac{15.00(\pm0.14)}{12.36(\pm0.15)} = 1.21$	$\frac{14.60(\pm0.15)}{11.86(\pm0.17)} = 1.23$
DS	$\frac{13.24(\pm0.20)}{12.64(\pm0.19)} = 1.05$	$\frac{11.23(\pm0.16)}{10.65(\pm0.16)} = 1.05$	$\frac{13.24(\pm0.20)}{11.23(\pm0.16)} = 1.18$	$\frac{12.64(\pm0.19)}{10.65(\pm0.16)} = 1.19$
mean	1.05	1.06	1.18	1.20

$(p_{\text{wet}} = 0.09,\ r^2_{\text{wet}} = 0.14)$ when regarding indentations in transverse direction. (Figure 4.5).

Dry elastic energy was 1.16 times higher than wet elastic energy $(p < 0.05)$ whereas dry dissipated energy was 1.30 times higher than wet dissipated energy $(p < 0.05)$. No significant difference between the elastic energy in axial and in transverse indentation direction could be found for wet or dry indentation conditions $(p > 0.5)$. The dissipated energy showed significant differences between indentations in axial and transverse indentation direction $(p < 0.05)$. Significant differences $(p < 0.05)$ for both elastic and dissipated energy were found when comparing indentations from the core and the periphery for both indentation con-

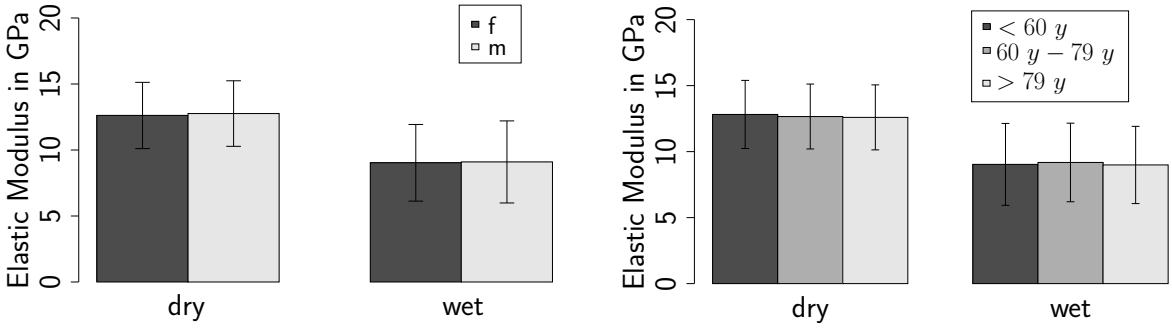

Figure 4.4: Left: The influence of gender (m – male, f – female) on the elastic moduli under dry and wet indentation conditions. Right: The influence of age on the elastic moduli under dry and wet indentation conditions for three age groups $< 60\ y$, $60\ y$ to $79\ y$ and $> 79\ y$. The figure depicts means of elastic moduli and the whiskers denote ± 1 standard deviation.

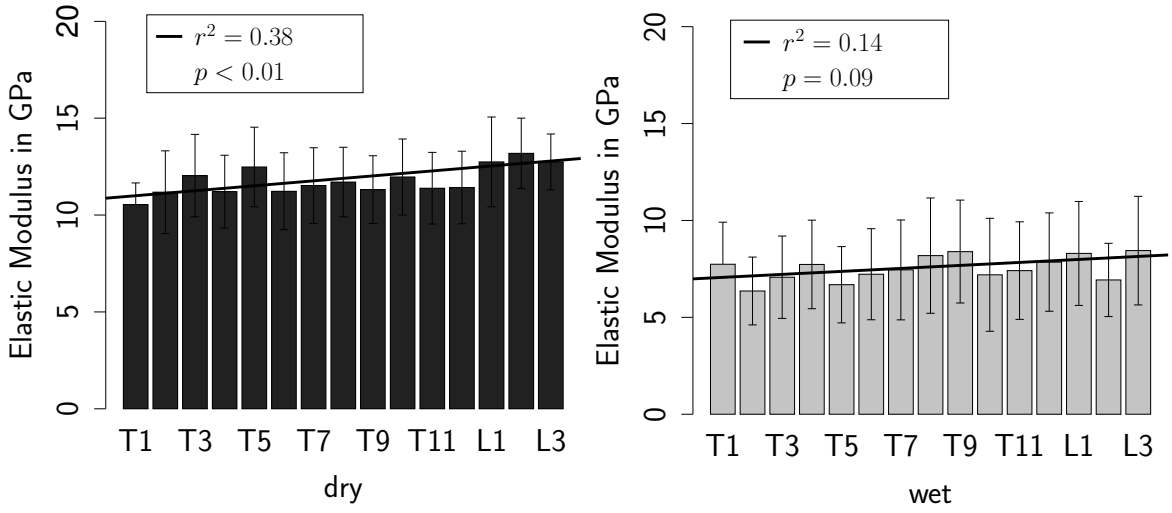

Figure 4.5: The influence of the vertebral level on the elastic moduli. Left for dry indentation conditions and right for wet indentation conditions. The figure shows, means of elastic moduli obtained in transverse indentation direction over the vertebral levels used. The whiskers denote ± 1 standard deviation per level. The black line depicts a regression between elastic moduli and vertebral levels.

ditions (Figure 4.6). Except for the comparison of the elastic energy in axial and transverse direction rehydration increased the ratios of the mean indentation work (Table 4.2). No difference could be found for dry or wet indentation conditions in the elastic or dissipated energy ($p > 0.05$) with respect to gender (Figure 4.7). Elastic and dissipated energies increased with age under wet indentation condi-

tions ($p < 0.05$). In the dry case, elastic energy showed significant differences ($p < 0.05$) but not dissipated energy (Figure 4.7).

Table 4.2: The table compares the indentation energies of wet (top) and dry (bottom) indentations. Elastic (W^{e}) and dissipated (W^{d}) indentation energy is given in $\mathrm{mN} \cdot \mu\mathrm{m}$ plus minus their respective coefficient of variation. Ratios of the means of the elastic and dissipated energy are given in the same way as the elastic moduli, that is, for the inner (IN) and peripheral (OUT) indentation regions as well as for indents in axial (AX) and in transverse indentation direction (TR) separately. See Figure 4.2 for a sketch of the indentation locations as well as the regions used to compute the indentation work.

Wet Indentation:

	IN_{AX}/OUT_{AX}	IN_{TR}/OUT_{TR}	AX_{IN}/TR_{IN}	AX_{OUT}/TR_{OUT}
W^e	$\frac{16.11(\pm0.29)}{14.35(\pm0.35)} = 1.12$	$\frac{16.35(\pm0.41)}{13.45(\pm0.51)} = 1.22$	$\frac{16.11(\pm0.29)}{16.35(\pm0.41)} = 0.99$	$\frac{14.35(\pm0.35)}{13.45(\pm0.51)} = 1.07$
W^d	$\frac{51.24(\pm0.27)}{47.23(\pm0.33)} = 1.08$	$\frac{43.96(\pm0.44)}{37.08(\pm0.56)} = 1.19$	$\frac{51.24(\pm0.27)}{43.96(\pm0.44)} = 1.17$	$\frac{47.23(\pm0.33)}{37.08(\pm0.56)} = 1.27$

Dry Indentation:

	IN_{AX}/OUT_{AX}	IN_{TR}/OUT_{TR}	AX_{IN}/TR_{IN}	AX_{OUT}/TR_{OUT}
W^e	$\frac{17.81(\pm0.21)}{17.19(\pm0.26)} = 1.04$	$\frac{17.95(\pm0.2)}{17.13(\pm0.21)} = 1.05$	$\frac{17.81(\pm0.21)}{17.95(\pm0.2)} = 0.99$	$\frac{17.19(\pm0.26)}{17.13(\pm0.21)} = 1.00$
W^d	$\frac{63.04(\pm0.18)}{61.52(\pm0.21)} = 1.02$	$\frac{56.46(\pm0.17)}{53.95(\pm0.18)} = 1.05$	$\frac{63.04(\pm0.18)}{56.46(\pm0.17)} = 1.12$	$\frac{61.52(\pm0.21)}{53.95(\pm0.18)} = 1.14$

Combining the results of dry and wet indentations and averaging over IN and OUT, two stiffness tensors can be given for trabecular bone tested in dry and wet condition (Figure 4.8).

4.4 Discussion

As expected in hypothesis i) E was $\approx 29\%$ lower when testing rehydrated. According to hypothesis ii), the ratios $E_{\mathrm{AX}}/E_{\mathrm{TR}}$ were 1.13 and 1.23 times higher in wet indentation than in dry indentation depending on whether the test was performed in the inner or the peripheral region of trabeculae. In accordance with hypothesis iii), the ratios $E_{\mathrm{IN}}/E_{\mathrm{OUT}}$ were 1.05 and 1.16 times higher when measured under wet indentation conditions depending on whether axial or transverse indentation directions were tested. Gender did not show a changing effect on the elastic moduli

after rehydration which agrees with hypothesis iv). Compared to dry indentation

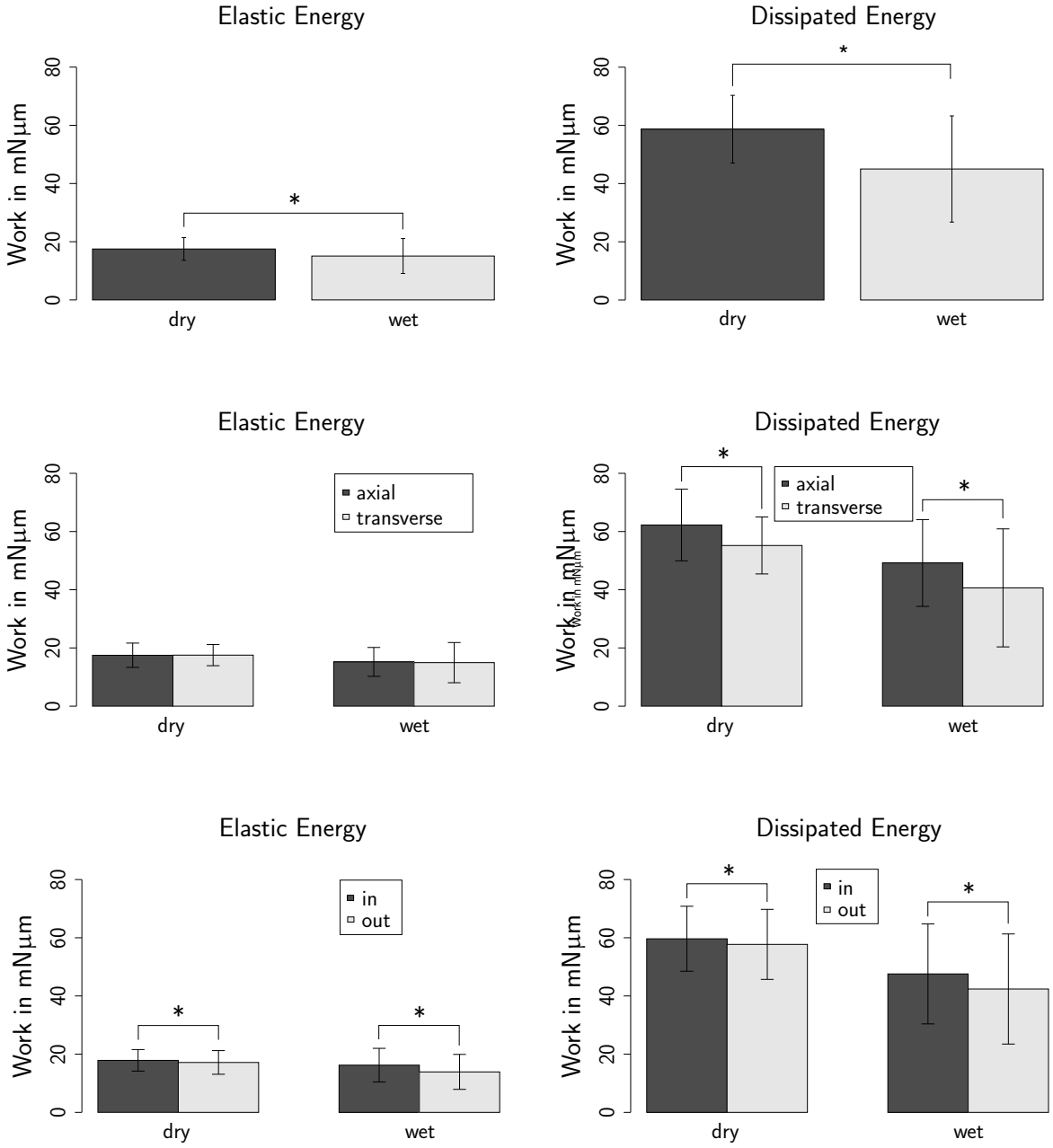

Figure 4.6: Elastic and dissipated indentation energy for indentations under dry and wet conditions (Top row). The middle row compares indentation energies in axial and transverse indentation direction. The bottom row compares the work for indentations on the core and the periphery. Energy means are shown and the whiskers denote ± 1 standard deviation.

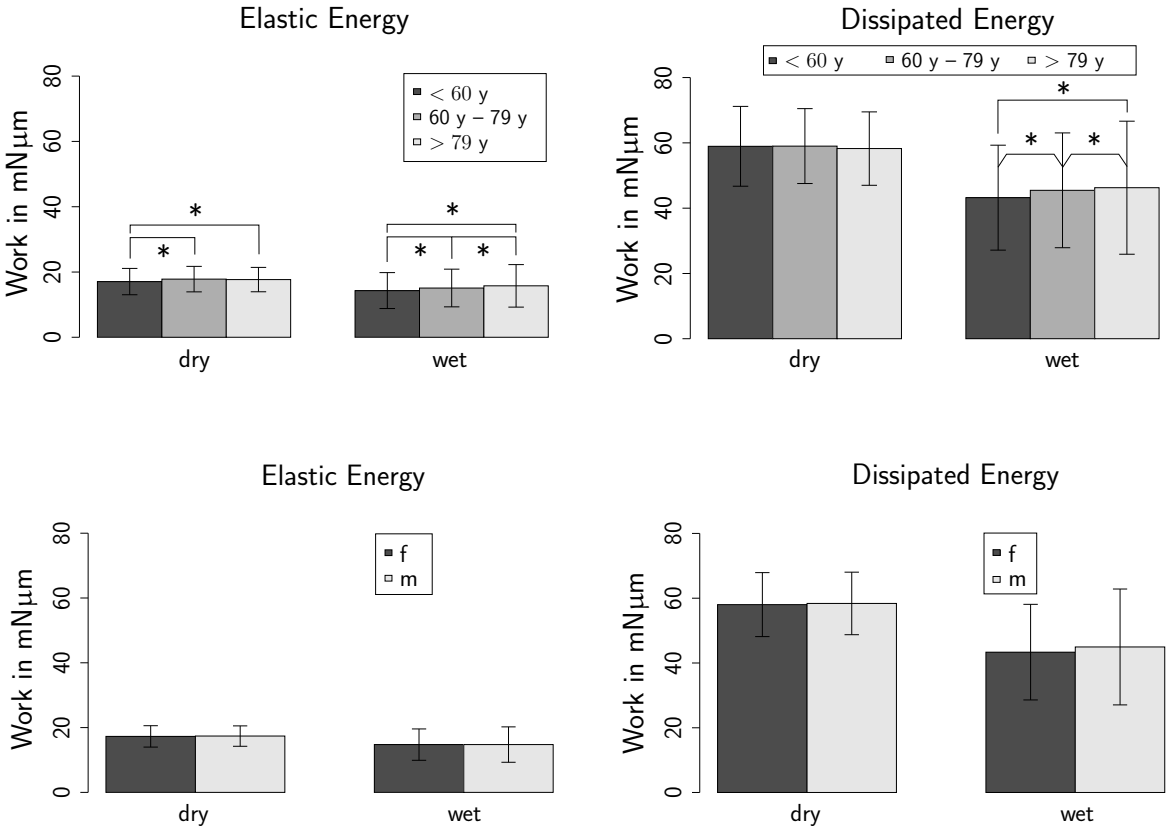

Figure 4.7: Wet elastic and dissipated energy seem to depend on age (top left and right). No difference between elastic and dissipated energy could be found with respect to gender. Energy means are shown and the whiskers denote ± 1 standard deviation.

conditions, the result strengthened with $p_{\text{dry}} \approx 0.13$ and $p_{\text{wet}} \approx 0.54$. According to hypothesis v), age did not show any effect on the elastic moduli under wet testing conditions. For dry indentation conditions this insignificance was stronger $\left(p_{\text{dry}} \approx 0.41 \text{ and } p_{\text{wet}} \approx 0.28\right)$. The correlation between vertebral level and elastic moduli was weaker for wet indentation conditions with $p_{\text{wet}} \approx 0.09$ and $r^2_{\text{wet}} = 0.14$ compared to $p_{\text{dry}} \approx 0.01$ and $r^2_{\text{dry}} = 0.38$. This disagrees with hypothesis vi). As expected in hypothesis vii), the anatomic direction stayed significantly different in the same fashion as for the dry indentations. In disagreement with hypothesis viii) indentation energies were not similarly affected by rehydration compared to the elastic moduli.

The overall wet mean elastic moduli were in the lower third of the range of elastic moduli given in a study on the femoral neck (Hengsberger et al., 2002). In addition, the results were in good agreement with elastic moduli given in the liter-

$\mathbb{S}^{\text{dry}}$ $\mathbb{S}^{\text{wet}}$

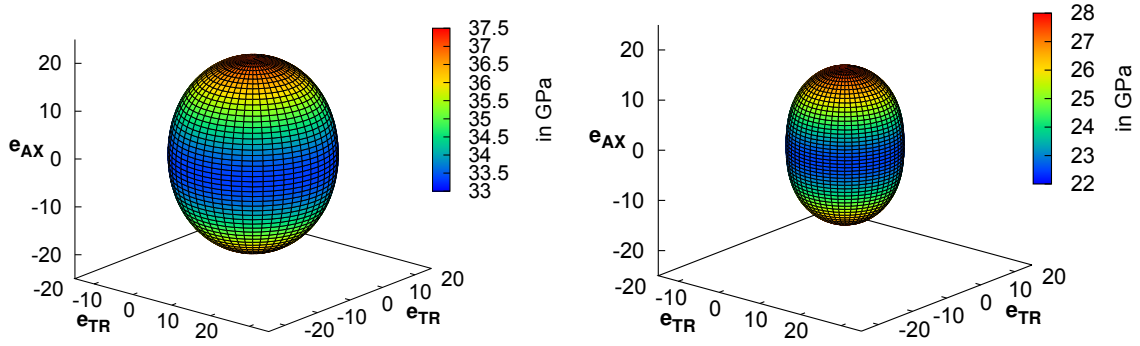

$$\begin{pmatrix} 16.82 & 7.91 & 8.62 & 0 & 0 & 0 \\ 7.91 & 16.82 & 8.62 & 0 & 0 & 0 \\ 8.62 & 8.62 & 19.94 & 0 & 0 & 0 \\ 0 & 0 & 0 & 9.70 & 0 & 0 \\ 0 & 0 & 0 & 0 & 9.70 & 0 \\ 0 & 0 & 0 & 0 & 0 & 8.90 \end{pmatrix} \qquad \begin{pmatrix} 11.13 & 5.24 & 6.15 & 0 & 0 & 0 \\ 5.24 & 11.13 & 6.15 & 0 & 0 & 0 \\ 6.15 & 6.15 & 15.37 & 0 & 0 & 0 \\ 0 & 0 & 0 & 6.92 & 0 & 0 \\ 0 & 0 & 0 & 0 & 6.92 & 0 \\ 0 & 0 & 0 & 0 & 0 & 5.89 \end{pmatrix}$$

Figure 4.8: Visualisation of two constructed stiffness tensors along the longitudinal axis of a trabecula. Left, for trabecular bone tested under dry conditions. Right, for trabecular bone tested under wet conditions. The shape depicts the elongation modulus and the colour encodes the bulk modulus (He and Curnier, 1995). The stiffness tensors give the mean stiffness anisotropy and were constructed by averaging the results over all anatomic directions.

ature for *L*5 (Hoffler et al., 2000a). The reduction of the elastic moduli of 29% after rehydration was slightly higher than reported in the literature with 20% (Turner et al., 1999; Hoffler et al., 2005). The test duration of approximately 4.5 h including rehydration should not have influenced the results. According to Hengsberger et al. (2002) no modulus reduction for samples submerged in Ringer's solution was observable within the first 12 h. A possible mineral washout was assumed to be hindered by HBSS. The used indentation depth of 2.5 µm facilitated good reproducibility by proper averaging over approximately three lamellae (Rho et al., 1998). However, it could have introduced additional damage, thus, lowering the elastic moduli (Zhang et al., 2008). Nevertheless, a 29% lower elastic modulus obtained under wet indentation conditions seems to be reasonable when compared to macroscopic values of compact bone (Dempster and Liddicoat, 1952). Interest-

ingly, the wet mean elastic modulus was similar to a numerically obtained effective tissue modulus for vertebral trabeculae (Bevill and Keaveny, 2009).

For the wet indentations, the ratio of E_{AX}/E_{TR} was higher than those found in the literature (Rho et al., 1999) regardless whether the ratio was taken for the inner or the peripheral region. In contrast, for dry indentation conditions the presented ratios did go well with the reported findings. The authors (Rho et al., 1999) dehydrated their specimens with alcohol prior to embedding. It is known that alcohol dehydration increases the stiffness of bone tissue (Bushby et al., 2004). The present study deployed a mild defatting procedure which was assumed to have little influence on the stiffness. Thus, the differences were probably due to different preparation protocols.

The mean ratios in Table 4.1 imply that the rehydration effect increases from the core to the periphery and from axial to transverse indentation direction. This may be due to the less mineralised periphery (Boyde et al., 1993; Linden et al., 2001) having a greater possibility to absorb water because of the higher amount of nonmineralised collagen fibres. For the transverse indentation direction, this could be further increased by a greater freedom of the collagen fibres to swell. The increased ratio E_{AX}/E_{TR} leads to a more slender orientation distribution of the stiffness which results in a stiffness-tensor with a higher degree of anisotropy than in the dry case (Figure 4.8). The reinforcement of the ratios IN/OUT and AX/TR by rehydration compared to dry indentation may further arise from different swelling modes in axial and transverse direction. This could be due to different water uptakes resulting from the orientation of collagen fibres along the longitudinal axis of a trabecula. The results for IN and OUT suggest that the swelling seems to depend on the degree of mineralisation. The measured elastic moduli could be influenced by an artificial bulging of the tissue surface that would not occur in situ. However, this needs further investigation.

Rehydration did not abolish the significant difference in the anatomic direction. This effect may rather be due to slight misalignments of the trabecular cross-sections with respect to the polished specimen surface. This misalignment was presumably caused by the nonorthogonal nature of the trabecular network. Because vertebral trabeculae are rather aligned with the cranial-caudal direction, indentations are driven more on-axis on those specimens. Thus, they deliver slightly higher moduli than the indentations on the specimens gained in anterior-posterior and dexter-sinister direction. Furthermore, if this effect would have been due to the material instead of the alignment, changes similar to the other factors should have occurred after rehydration. The differences in anatomic direction would lead to quantitatively slightly different stiffness tensors if these were set up for a specific anatomic direction. The qualitative effects of rehydration would stay the same (Table 4.2, Figure 4.8).

Elastic modulus remained independent of age and gender after rehydration. These results agree with findings for femoral trabecular bone (Hoffler et al., 2000b). The insignificant correlation between elastic modulus and vertebral level under wet indentation conditions goes with the expectation that the underlying bone material is independent of the vertebral level within the spinal column. The weakening of this correlation and the slight changing insignificances for age and gender are supposedly due to an increased variance reflected in the increased coefficients of variation under wet indentation conditions. It was assumed that bone diseases such as osteopenia lead to an extrinsic rather than an intrinsic deterioration and vertebrae showing those signs were not excluded from the study. This may have contributed to the coefficients of variance.

The indentation work W determined in this study was higher than that reported for tibial osteonal bone. In contrast, the elastic moduli found in the present study were lower (Fan and Rho, 2003). This could have been due to different loading protocols and preparation procedures. Since the elastic moduli in the present study were in good agreement with the literature, the results for the indentation work were considered reasonable for the chosen loading protocol. The indentation work followed partly the same pattern as the elastic modulus. That was, a decrease when rehydrated, lower elastic or dissipated energy for indentations in the periphery than in the centre and lower dissipated energy for indentations in transverse than in axial indentation direction. The lower energy dissipation after rehydration could indicate that water is protective with respect to W^{d} for a constant indentation depth (Figure 4.6). Interestingly, no difference was found when evaluating the elastic work with respect to indentations in axial and transverse indentation direction regardless whether dry or wet indentation conditions were present. It seems that the lower force reached for the transverse indentation direction was compensated by the reduced amount of plastic deformation. The higher energy dissipation in axial indentation direction could have been due to a higher amount of slippage between the collagen fibrils. Against that, fibrils in transverse indentation direction were rather loaded in bending and the amount of slippage could have been lower. As for the elastic moduli, rehydration had no impact on gender and both, wet and dry elastic or dissipated energies were equal. When regarding the energies under wet indentation conditions with respect to age, weakly increasing energies with aging tissue could be observed, which is in contrast with the loss of internal energy by damage accumulation expected in older bone. This increase in energies was apparently due to an increase in maximum force ($p < 0.05$), as no significant difference was found in the indentation or creep depth for both testing conditions. In fact, the increased maximum force may be attributed to an improved surface detection during the indenter approach in old when compared to young bone, especially in wet condition. Less mature cross-linking of the collagen

and more swelling of proteoglycans at the surface of younger bone may trigger early surface detection, decrease maximum force, elastic and dissipated energy without affecting stiffness (Wang et al., 2002). Beyond this potential artefact, the indentation properties of bone tissue remained surprisingly constant with age.

This study investigated the effects of rehydration on the transverse isotropic material properties of vertebral trabecular bone at different locations with a view to different donor specific properties. It could help to further improve the understanding of the mechanical properties of vertebral trabecular bone.

Chapter 5

Valid μFinite Element Models can be Set Up Directly With Nanoindentation

As published in: Wolfram, U., Wilke, H.-J., Zysset, P. K., 2010. Valid μFinite Element Models of Vertebral Trabecular Bone can be Obtained Using Tissue Properties Measured with Nanoindentation Under Wet Conditions. Journal of Biomechanics 43 (9), 1731 – 1737. ★

5.1 Introduction

Osteoporosis-related vertebral fractures represent a major public health problem (Rao and Singrakhia, 2003). Anatomy specific CT-based Finite Element (FE) simulations could help identifying which vertebrae have the highest risk of fracture and help deciding upon the need for vertebroplasty or other surgical intervention (Crawford et al., 2003a). Continuum level FE simulations require effective macroscopic material properties of the vertebra. Micro Finite Element (μFE) models can be used to circumvent the difficult experiments (Rincón-Kohli and Zysset, 2009) that are necessary to determine these effective material properties.

μFE models were used to determine apparent stiffness tensors for trabecular bone (Rietbergen et al., 1996). It was shown that it is possible to determine yield surfaces using μFE models (Bayraktar et al., 2004a,b). These and other studies used calibrated micro-mechanical properties for the trabecular tissue which were obtained inversely from simulations of uniaxial macro-mechanical experiments (Rietbergen et al., 1995; Niebur et al., 2000; Bayraktar et al., 2004b; Verhulp et al., 2008). Calibrated effective tissue stiffnesses can diverge for more than an order of magnitude and show lower precision in individual measurements of the tissue modulus (Bevill et al., 2009a). From a quantitative point of view, these μFE models depend critically on the chosen trabecular tissue properties.

Specimen specific tissue properties can be obtained using depth-sensing indentation techniques. These give the possibility to determine the elastic properties of trabecular bone *ex vivo* with a high spatial resolution (Oliver and Pharr, 1992). For μFE models of dried femoral trabecular bone tissue moduli were obtained using nanoindentation under dry conditions (Chevalier et al., 2007). Different authors determined the elastic moduli (E_{tiss}) of trabecular and cortical tissue (Rho et al.,

1997, 1999; Roy et al., 1999; Zysset et al., 1999; Lewis and Nyman, 2008). A reduction of E_{tiss} of (20%) was found when comparing acoustic microscopy and nanoindentation (Turner et al., 1999). This was due to rehydration of the specimens for acoustic microscopy. Reductions of E_{tiss} were also found when comparing nanoindentation under dry and wet measurement conditions (Hengsberger et al., 2002; Hoffler et al., 2005).

The question remains whether linear elastic μFE models of vertebral trabecular bone with and without specimen specific tissue properties yield similar results than non-destructive macroscopic experiments under moist conditions. The aim of the study was, to compare μFE models of rehydrated bone specimen with experimentally obtained tissue moduli with experimentally determined apparent elastic properties obtained with the same specimen for uniaxial tension, compression or torsion tests.

5.2 Materials and Methods

Sixteen fresh frozen vertebrae (T6 – L2) of 10 donors (7 male, 3 female) with a median age of 51 y (37 – 84 y) were used. Vertebrae were cleaned from surrounding soft tissue and the posterior parts were moulded in Poly-Methyl Methacrylate (Technovit 3040, Heraeus Kulzer GmbH, Wehrheim, Germany). Subsequently, the endplates were removed with a high precision band saw (Exakt Apparatebau, Norderstedt, Germany). Thirty cylindrical samples (on average two per vertebra, 10 for compression, 10 for tension, 10 for torsion) of 8×18 to 25 mm depending on the vertebral height were cored from the remaining slices using a custom made core drill. Marrow was removed from the top and bottom ends of the cylinders using a pulsed water jet (Braun Oral-B Professional Care 6500, Kronberg, Germany). The top and bottom ends of the cylinders were moulded in Polyurethane (PU) (SG 2000, ebalta Kunststoff GmbH, Rothenburg ob der Tauber, Germany) so that an approximately 12 mm free gage length was left in-between (Figure 5.1).

The endcapped cylinders were submerged in 0.9% sodium chloride and scanned in a μCT (μCT 40, SCANCO Medical AG, Brüttisellen, Switzerland) at a resolution of $(12\ \mu\text{m})^3$. Specimens were refrozen after scanning. Greyscale μCT-datasets were scaled to resolutions of $(24\ \mu\text{m})^3$, $(36\ \mu\text{m})^3$ and $(48\ \mu\text{m})^3$ and thresholded using the single level threshold of IPL (Image Processing Language, SCANCO Medical AG, Brüttisellen, Switzerland).

μFE models were setup for *parFE* (Arbenz et al., 2008) by converting image voxels to 8-noded volume elements. Nodes in the bottom cross-section of the cylinders were constrained to $\left(u_x = u_y = u_z = 0\right)$. In uniaxial tension and compression, the nodes of the top cross-section were loaded with a displacement in z-direction and constraint in the other directions $\left(u_x = u_y = 0,\ u_z = 0.1\ \text{mm}\right)$. In

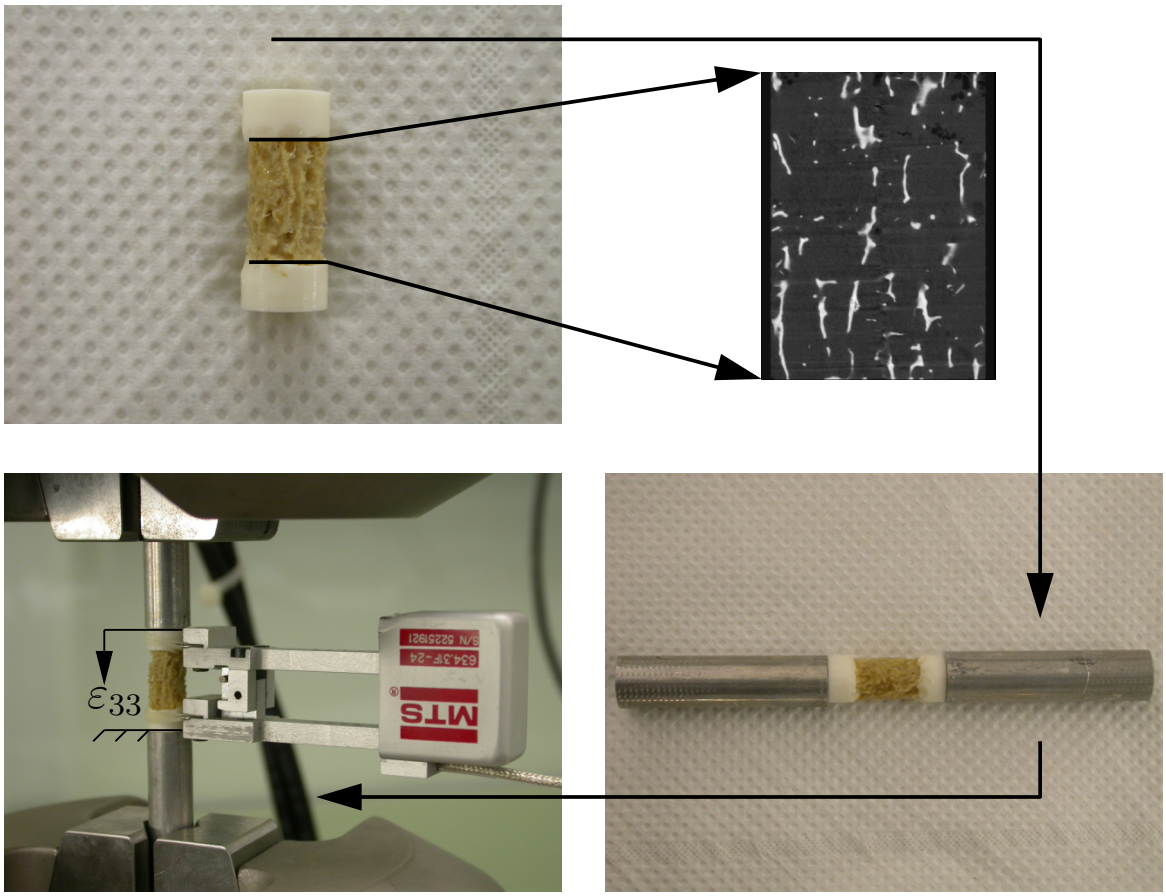

Figure 5.1: Workflow for an exemplary compression specimen. Top left, specimen with moulded endcaps. Top middle, midplane image from the CT data set of the gage length. Top right, glued metal rods for gripping. Bottom right, macroscopic test to determine the apparent elastic and shear moduli. Bottom left, axial trabecular cross-section with six nanoindentation imprints (black triangles) to obtain specimen specific trabecular tissue properties. Bottom middle, resulting FE model with deflection field $|u|$. The thick grey arrows illustrate the results which were input to the FE model and the subsequent validation.

torsion, the top plane was loaded with a rotation φ around the middle axis of the cylinder $\left(u_x = u_y \neq 0, \quad u_z = 0, \; \varphi = 0.1^\circ\right)$. Forces and Moments were computed and apparent elastic (E_{app}) and shear moduli (G_{app}) were calculated.

Tissue elastic properties were obtained using nanoindentation. Indentation tests were performed after coring on the cancellous tissue which surrounded the cylinders. Two 5 mm thick slices one for wet and one for dry indentation were obtained using the high precision band saw. The slices were submerged in soap water in an ultrasound bath (Sonorex, BANDELIN electronic GmbH & Co. KG, Berlin, Germany) and exposed to ultrasound for five minutes at 35 kHz. The bath was left

at 40°C for 12 h. Afterwards, the samples were exposed to ultrasound at 35 kHz for five minutes, rinsed with water and left for drying over night. Specimens were than embedded in epoxy resin (Struers A/S, Ballerup, Denmark) and cured 12 h at ≈21°C. Subsequently, the samples were polished with progressive grades of silicon carbide paper (P1000, P1400, P2000, P2500, P4000 – Hermes Schleifmittel GmbH & Co. KG, Hamburg, Germany) and finished with 1 μm diamond paste on a polishing cloth. Between each grinding step the samples were cleaned in a distilled water ultrasound bath for seven minutes at 35 kHz. Wet indentation samples were rehydrated in 99% saturated Hank's Balanced Salt Solution (HBSS) for 1.5 h prior to nanoindentation and submerged in HBSS during testing. Indentation was performed using a depth-sensing nanohardness tester equipped with a pyramidal Berkovich diamond tip and in case of the wet indentation additionally with a wet cell (CSM Instruments SA, Peseux, Switzerland). Indentations were driven to 2.5 μm depth. Load was applied as monotonic ramp at 120 $\frac{\mathrm{mN}}{\mathrm{min}}$, unexpended for 30 s to prevent creep influences and an unloading ramp like the loading ramp (Wolfram et al., 2010a). Three indentations were performed on three axial trabecular cross-sections in the core and the periphery of trabeculae giving 18 indentations per sample (Figure 5.1). A Poisson's ratio of $\nu^{tiss} = 0.32$ was assumed (Rho et al., 1997; Hengsberger et al., 2003). Tissue elastic moduli (E_{tiss}) were obtained (Oliver and Pharr, 1992) and averaged over all 18 indentations per sample. This yielded specific E_{tiss} under wet and dry conditions for each cylindrical specimen.

Prior to apparent mechanical testing, specimens were rehydrated for one hour in 0.9% sodium chloride. Aluminium rods were glued onto the endcaps using cyanoacrylate (Loctite, Henkel Central Eastern Europe GmbH, Austria). An extensometer was attached to the PU endcaps after mounting the specimen to the testing system (Mini-Bionix MTS system, Milwaukee, MN, USA) (Figure 5.1). In torsion, angular data were recorded with the rotary variable differential transformer of the testing system. Specimens were tested moist and preconditioned with three cycles to $\varepsilon = 0.004$ strain at a strain rate of $\dot{\varepsilon} = 0.004\ \frac{1}{\mathrm{s}}$. Subsequently, the specimens were loaded up to $\varepsilon = 0.004$ strain (in case of torsion to $\gamma = 0.008$) at a strain rate of $\dot{\varepsilon} = 0.002\ \frac{1}{\mathrm{s}}$ (Haddok et al., 2004; Bayraktar et al., 2004b). Apparent tensile and compressive stress was calculated from the recorded forces as $\sigma = \frac{F}{A_0}$ with A_0 the initial sample cross-section. Torque-twist-angle curves were denoised using an average filter (Jähne, 2005). Peak apparent torsional stress was calculated with r the specimen radius, θ the twist-angle per unit length and M_T the torque moment (Nadai, 1950).

$$\tau = \frac{1}{2\pi r^3}\left(\theta\frac{dM_T}{d\theta} + 3M_T\right) \tag{5.1}$$

The derivative $\frac{dM_T}{d\vartheta}$ was approximated from the denoised torque-twist-angle curve using a central difference operator. Accounting for the influence of the fixation and the PU endcaps, the shear strain γ_B was calculated by first subtracting the influence of the machine compliance from the angular data and than subtracting the strain over the endcaps from the strain over the whole sample.

$$\gamma_B = \left(\Delta\vartheta - \frac{M_T}{K_F}\right)\frac{r_S}{\ell_S} - \left(\frac{M_T \ell_{BP}}{J_{BP} G_{BP}}\right)\frac{r_{BP}}{\ell_{BP}} \tag{5.2}$$

Here, $\Delta\vartheta$ denotes the twist-angle, K_F the fixation stiffness, ℓ_{BP}, r_{BP} endcap length and radius and ℓ_s, r_s sample length and radius. J_{BP} and G_{BP} denote the polar moment of inertia and the shear modulus of the endcap. K_F was determined to 17317.31 $\frac{\text{Nmm}}{\text{rad}}$ with seven moulded PU cylinders of 9×20 mm using the same test protocol as for torsion. A rule of mixture was used to calculate G_{BP}.

$$G_{BP} = v_f G_P + \left(1 - v_f\right) G_B \tag{5.3}$$

Where, $G_P = E_P / 2\left(1 + \nu\right)$ was the shear modulus of PU and G_B of bone which was derived in a similar fashion. Young's modulus of PU was determined to 2014 MPa with seven moulded PU cylinders of 9×20 mm using the compression test protocol. Young's modulus of bone E_B was directly measured using nanoindentation. Apparent Young's and shear moduli were obtained from the stress-strain curves using a moving regression (Figure 5.2).

Statistical analyses were performed with R (R Development Core Team, 2008). For nanoindentation, outliers were defined as any measurement below the 2.5^{th} or above the 97.5^{th} percentile leaving 545 out of 576 measurements. Simulations and measurements of apparent moduli were compared using Wilcoxon's Signed Rank Test to test differences in the distributions to a significance level of $p = 0.05$. The concordance correlation coefficient r_c (Lin, 1989) was used to evaluate the agreement between experiment and simulation with respect to E_{app} and G_{app}. Additionaly, Bland-Altman plots (Bland and Altman, 1986) were used to compare experiment and simulation in a one by one fashion. The μFE models were considered valid if the Wilcoxon tests showed no significant difference, $r_c > 0.95$ and the deviation of the mean differences in the Bland-Altman plots was ≤ 10 MPa with the averages of experiments and simulations placed over the whole range.

5.3 Results

Morphological analysis of the samples yielded an in-plane degree of anisotropy $DA_{ip} = 1.03 \pm 0.04$, volume fraction $v_f = 0.11 \pm 0.03$ and deviation of trabecular main direction from the cylindrical main axis $\alpha = 4.78^\circ \pm 2.36^\circ$. No difference was

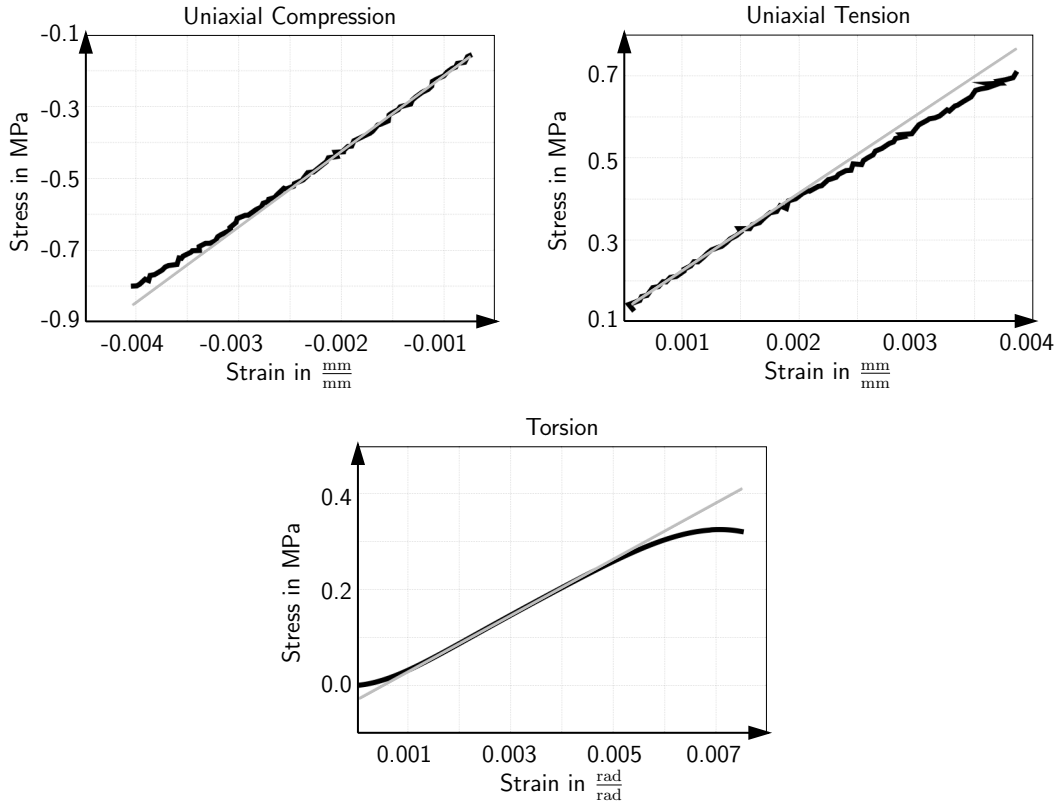

Figure 5.2: The loading part of exemplary datasets for compression, tension and torsion is shown. The black line indicates the data derived from the uniaxial measurements. The grey straight line is the result of a moving regression to determine Young's and Shear moduli at the stiffest part of the curve.

found in DA_{ip} and v_f between the samples for compression, tension and torsion ($p > 0.05$).

Different resolutions of the μFE models did not lead to differences in simulated E_{app} or G_{app} with $r_c \geq 0.98$ except for torsion at 48 μm where a drop of r_c to 0.95 was observed (Figure 5.3). Therefore, the focus is laid on the results for $(36\ \mu m)^3$.

Significantly lower $E_{tiss}^{wet} = 12.3$ GPa was found for wet indentation conditions compared to dry indentation conditions $E_{tiss}^{dry} = 15.4$ GPa ($p < 0.05$).

No significant difference was found between E_{app} in tension and compression ($p > 0.05$). Lower apparent moduli were found when simulating the experiments with tissue properties obtained under wet $\left(E_{app,UC}^{wet} = 419\ \text{MPa}, E_{app,UT}^{wet} = 443\ \text{MPa}, G_{app}^{wet} = 76\ \text{MPa}\right)$ than under dry indentation conditions $\left(E_{app,UC}^{dry} = 507\ \text{MPa}, E_{app,UT}^{dry} = 524\ \text{MPa}, G_{app}^{dry} = 100\ \text{MPa}\right)$ ($p < 0.05$).

No significant difference ($p > 0.05$) was found for E_{app} or G_{app} between experi-

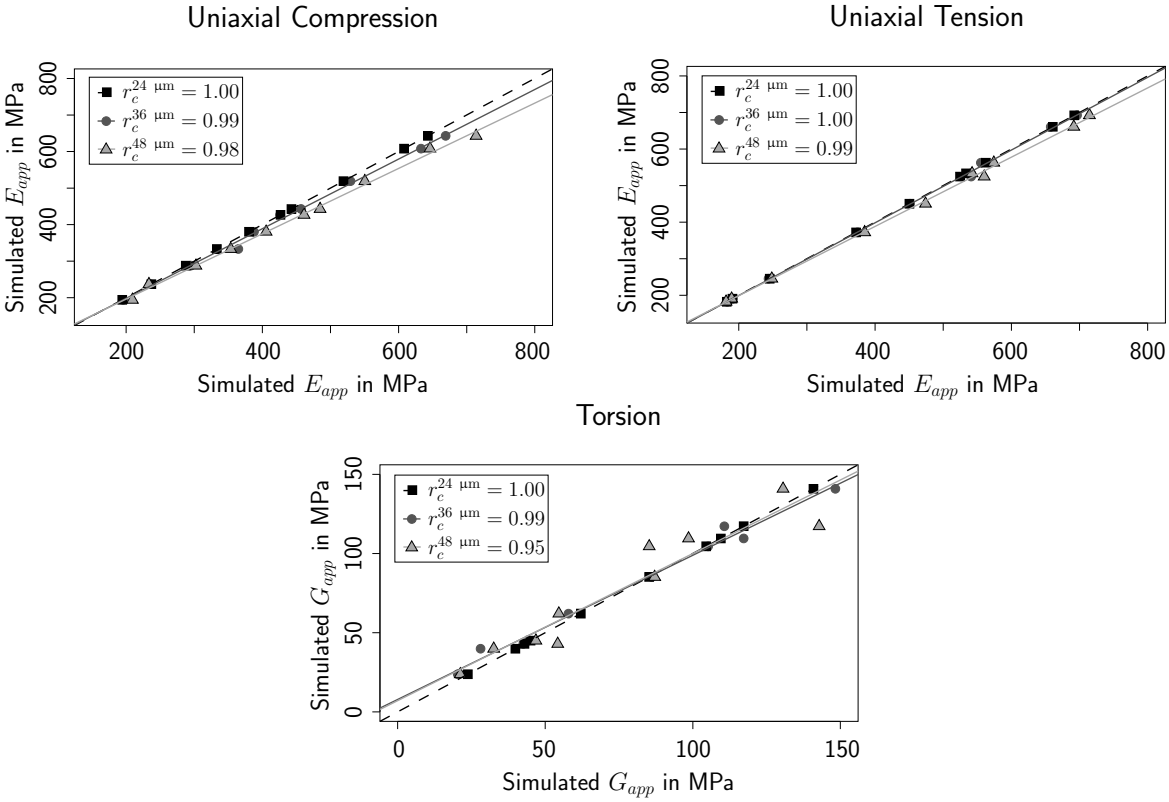

Figure 5.3: Influence of the resolution of the μFE models on the apparent modulus for the three load cases. Concordance correlation coefficients (r_c) were computed for the comparison. The results at 24 μm resolution were defined to serve as basis against which the comparison was carried out. Resolutions are colour encoded in the figure from 24 μm (black-square), 36 μm (grey circle) to 48 μm (light grey triangles). The dashed black line is the concordance line, i. e. the 24 μm results

ment and simulations with tissue properties obtained under wet indentation conditions. Experiments and simulations with tissue properties obtained under dry indentation conditions were different ($p < 0.05$) except for torsion (Figure 5.4).

Good concordance between experiment and simulation with wet tissue properties was found for compression $\left(r_c^{wet} = 0.96\right)$ and tension $\left(r_c^{wet} = 0.96\right)$. Moderate concordance between experiment and simulation with wet tissue properties was found for torsion $\left(r_c^{wet} = 0.81\right)$. Experiments and simulations with dry tissue properties showed distinctly lower r_c in all load cases (Figure 5.5).

The overestimation of E_{app} and G_{app} when using dry tissue properties in the simulation was as well observed in the Bland-Altman plots (Figures 5.6). Mean difference between experimental and simulated apparent moduli were found with -83.0 MPa in compression, -85.4 MPa in tension and -15.1 MPa in torsion. Wet

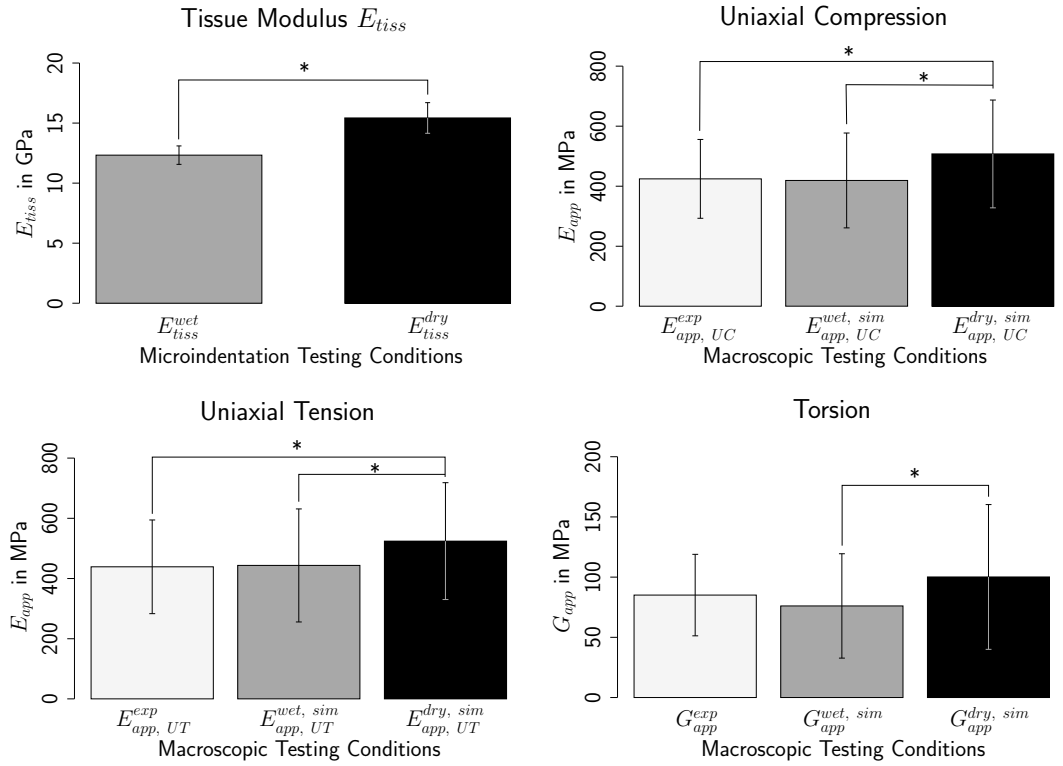

Figure 5.4: Mean apparent elastic moduli. Top left, tissue moduli for two different nanoindentation testing conditions. Top right, comparison of simulated compressive apparent moduli against experiment. Bottom left, comparison of simulated tensile apparent moduli against experiment. Bottom right, comparison of simulated apparent shear moduli against experiment. Whiskers denote ± 1 standard deviation. The asterisk denotes significance to a significance level of $p = 0.05$.

tissue properties yielded mean differences of 5.2 MPa in compression, 4.6 MPa in tension and 9.0 MPa in torsion. Compression and tension show low limits of agreement (± 1.96 standard deviation) which contain all data points in case of wet tissue properties. In case of torsion these are more severe (Figures 5.6).

5.4 Discussion

The goal of this study was to set up valid specimen specific μFE models of vertebral trabecular bone using experimentally obtained specimen specific effective tissue properties. The Wilcoxon tests did not show significant differences, $r_c^{wet} \geq 0.96$ for compression and tension. Mean differences in the Bland-Altman plots were $\leq$ 10 MPa when using tissue properties obtained under wet indentation conditions.

Apparent Young's moduli were slightly higher than those found in the literature

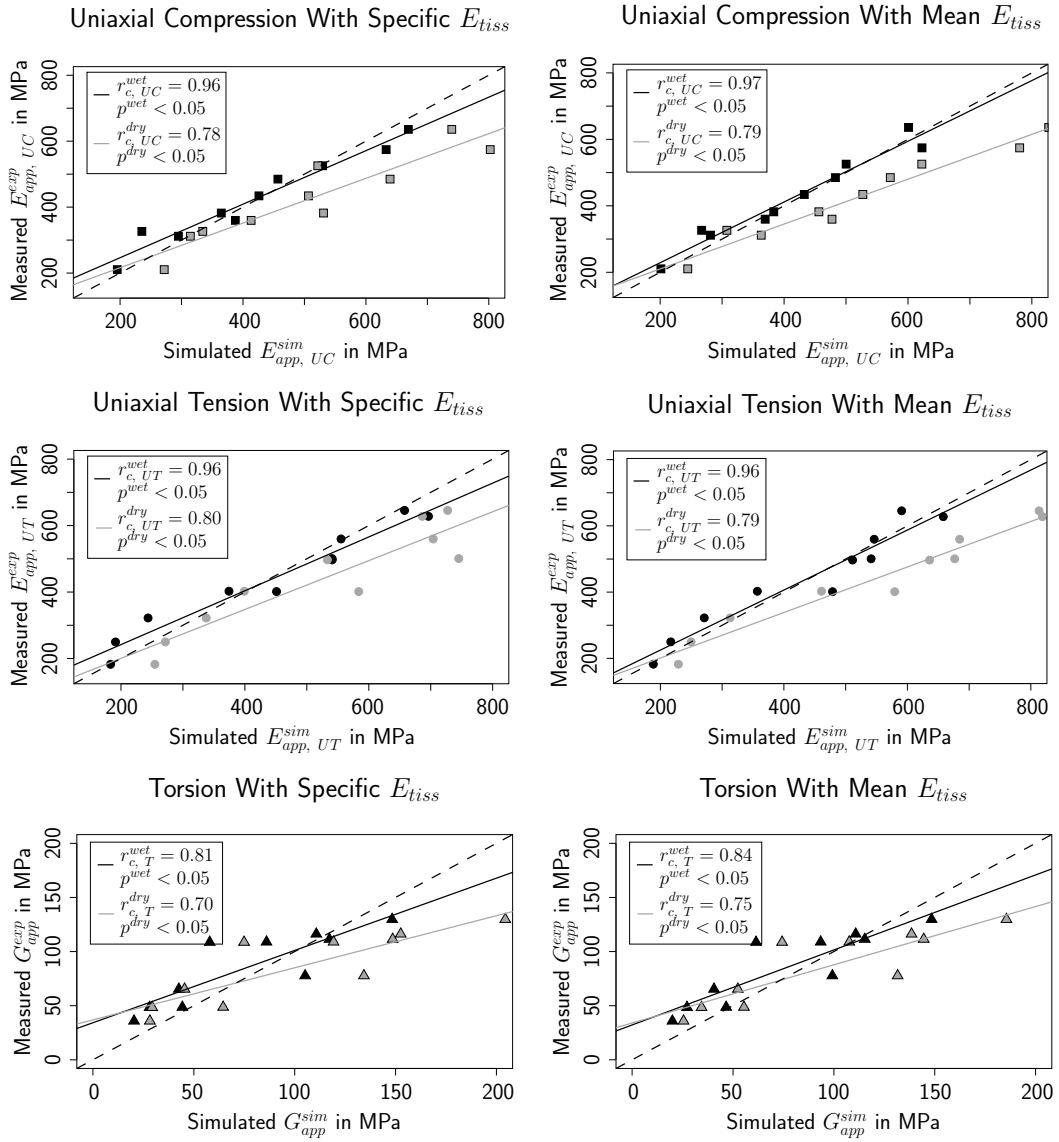

Figure 5.5: Concordance correlation coefficients of experimental apparent elastic moduli and computed apparent elastic moduli at a resolution of $(36\ \mu m)^3$ are shown. The left column of the figure depicts the results when using a specific tissue modulus for each specimen in each simulation. The right column shows the same results but using mean E_{tiss} as universal tissue modulus for all specimens in all simulations. Different tissue properties obtained from nanoindentation under wet and dry conditions are colour encoded with black and grey respectively. The dashed line indicates the concordance line $y = x$.

(Keaveny et al., 1997) but lay within the ranges reported by others (Kopperdahl and Keaveny, 1998; Morgan et al., 2003). The differences could have been due to different endcap techniques and slightly different testing setups and preparation

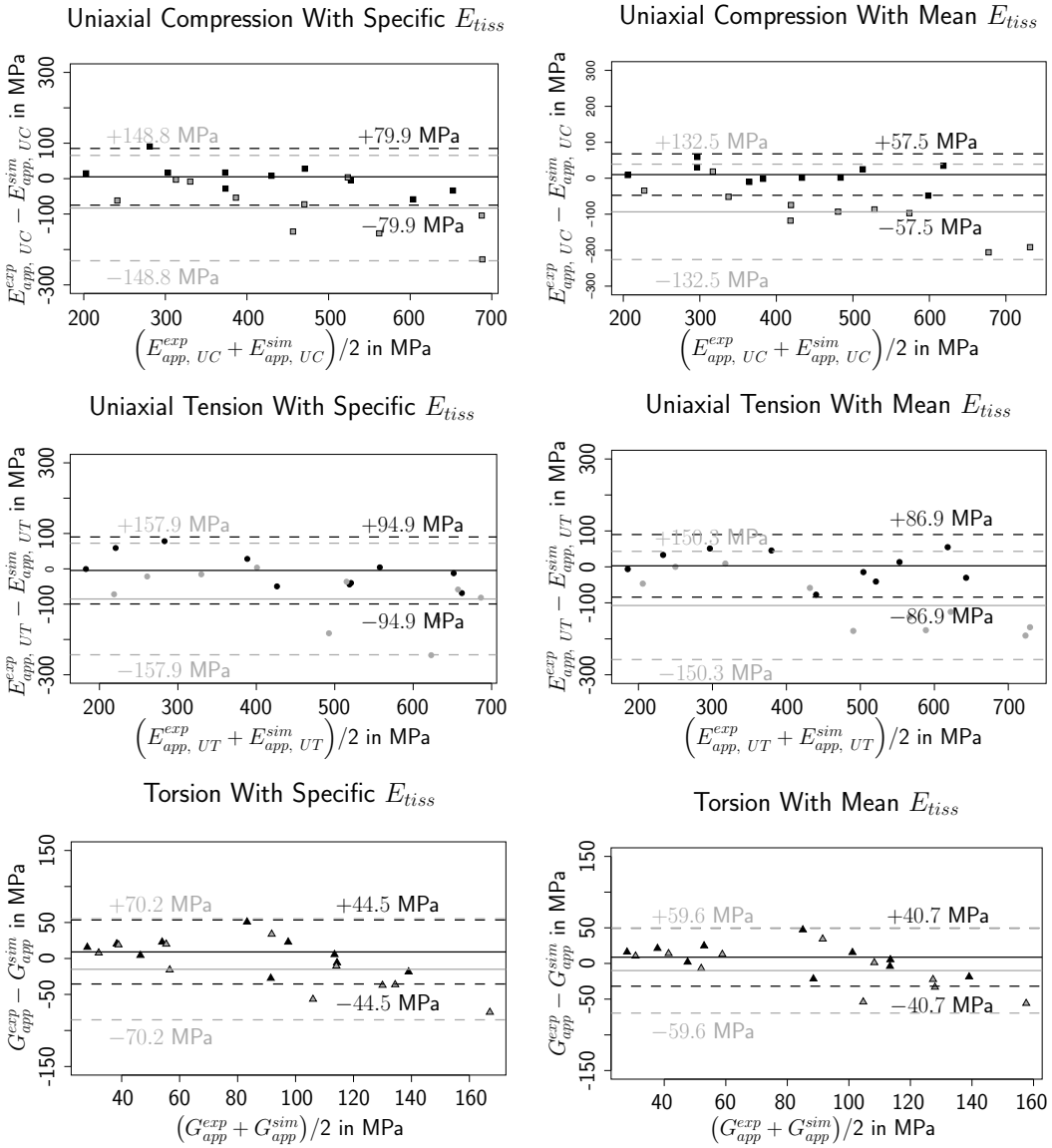

Figure 5.6: Bland-Altman plots of measured apparent elastic moduli and simulated apparent elastic moduli at a resolution of the FE models of $(36\ \mu m)^3$. The left column of the figure depicts the results when using a specific tissue modulus for each specimen in each simulation. The right column shows the same results but using mean E_{tiss} as universal tissue modulus for all specimens in all simulations. Wet and dry nanoindentation conditions are colour encoded with black and light grey respectively. The solid line denotes respective means of the differences and the dashed lines denote the limits of agreement (± 1.96 standard deviation from the mean difference).

protocols. The shear moduli obtained in the present study were lower than those presented for femoral trabecular bone (Garnier et al., 1999) or human trabecular

bone from different sites (Rincón-Kohli and Zysset, 2009). This could have been due to the higher volume fraction in these studies and as well to different testing setups and preparation protocols.

The small deviation of $0.96 \leq r_c < 1$ in case of compression and tension with wet tissue properties indicated small errors in the comparison of experiments and simulations in a one by one fashion (Figure 5.5). This was as well observable in the scatter in the Bland-Altman plots (Figure 5.6). These small errors were presumably due to the fact that the endcaps were not modelled explicitly. Instead just the free gage length with idealised fixed-end boundary conditions was modelled. It was assumed that this procedure causes minor errors (Bevill et al., 2009a). In case of torsion, r_c was worse with worse location and scale shifts (Figure 5.5). The limits of agreement in the Bland-Altman plots were higher as in case of uniaxial tension and compression relative to the value range (Figure 5.6). In case of torsion, the moulded endcaps could have lead to slight pooling/wicking of the PU into the gage length (Bevill et al., 2009a). This would cause boundary conditions different from those used for the μFE models and worsen the comparison. Furthermore, the rather unphysiological load case could have led to early damage which could have softened the material (Figure 5.7). In addition, torsion could have lead to more bending and geometrical nonlinearities. These effects were not included in the linear μFE models.

The worse concordance and the bigger limits of agreement of the models with dry tissue properties were relatable to the dry tissue moduli which were too stiff. This caused presumably as well the greater scatter between experiment and simulation. Using a tissue modulus of $\approx$ 15 GPa leads to a clear overestimation of the apparent stiffness. Hence, tissue moduli gained under similar testing conditions between macroscopic and microscopic experiments (dry, wet or alcohol dehydrated) should be used.

Surprisingly, a recomputation of the results with the mean tissue moduli as universal E_{tiss} for all μFE models did not worsen the results (Figures 5.5 and 5.6). This expresses the domination of bone volume fraction and architecture in prediction of apparent elastic properties. Specimen specific tissue moduli may be replaced by a properly measured mean tissue modulus to achieve valid μFE models. This indicates furthermore that a CT-based FE approach becomes reliable when bone volume fraction and fabric can be assessed like in high resolution peripheral quantitative CT.

The experimentally obtained tissue moduli under wet conditions were approximately twice as high than numerically calibrated E_{tiss} reported in the literature (Rietbergen et al., 1995; Verhulp et al., 2008). Both tissue moduli obtained under wet and dry indentation conditions were lower than those for femoral trabecular bone (Niebur et al., 2000; Bayraktar et al., 2004b). Interestingly, a numerically cal-

ibrated mean effective tissue modulus for vertebral trabecular bone was slightly lower than mean E_{tiss}^{wet} (Bevill et al., 2009a). The authors investigated the influence of the boundary conditions of FE models on the numerical determination of an effective tissue modulus. This indicates that their effective tissue moduli were in a sound range and the here presented models were properly constrained. Tissue moduli found in the present study were lower than those used to compute tissue strains (Rietbergen et al., 2003). This was probably due to the fact that the tissue moduli used in that study were obtained from alcohol dehydrated bone specimens (Turner et al., 1999). It is known that alcohol dehydration increases the stiffness of bone tissue (Bushby et al., 2004). However, these moduli lay in the range of the tissue moduli found under dry testing conditions in the present study. Wet tissue moduli were approximately 25% higher than those found on transverse trabecular cross-sections under wet conditions (Hoffler et al., 2000a). This is almost the ratio between elastic moduli measured on axial and those measured on transverse trabecular cross-sections (Rho et al., 1999). This indicates that the tissue moduli found in this study are in good agreement with the literature.

The chosen resolution of $(36\ \mu m)^3$ was approximately one fifth of a trabecu-

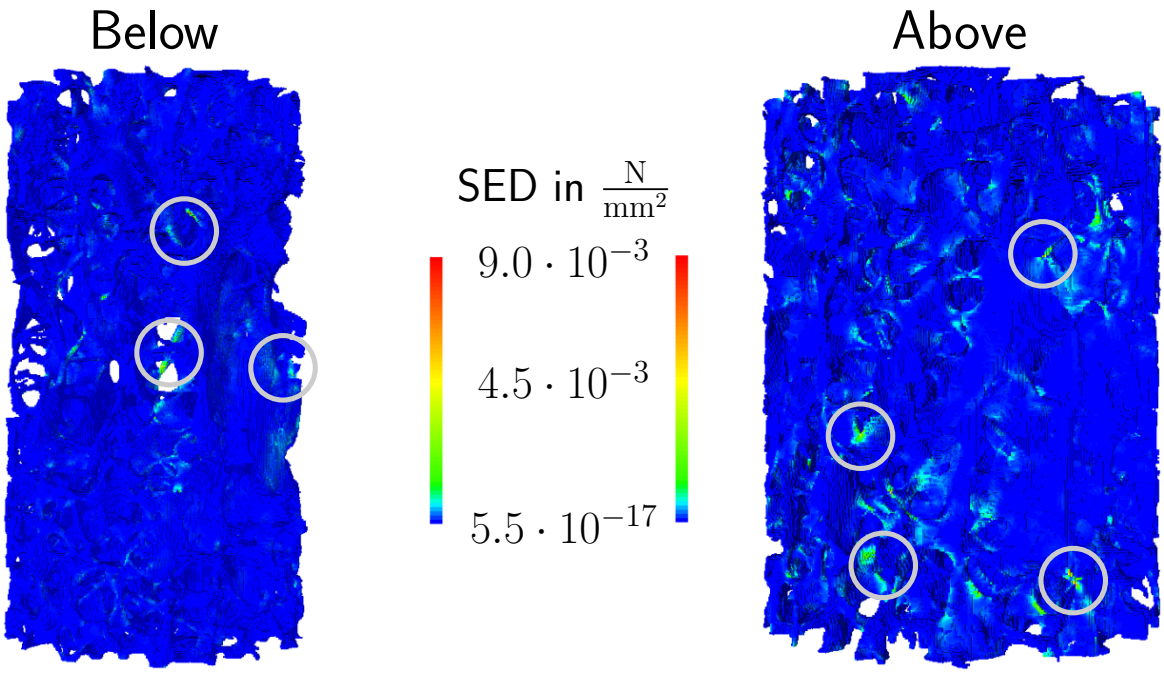

Figure 5.7: Strain energy density (SED) pattern in two extreme torsion samples indicate possible early damage. Left, a sample below and right, a sample above the concordance line in Figure 5.5. Rising SED is colour encoded from blue to red. The grey circles point to areas with high SED where damage could have occurred.

lar diameter in vertebrae. Dependencies of the results on the resolution of μFE models are known (Verhulp et al., 2008). The authors coarsened from $(40\ \mu m)^3$ to $(60\ \mu m)^3$. It was found that nonlinear μFE models at resolutions of $(80\ \mu m)^3$ and less are proper tools to examine micro-architecture related problems (Bevill and Keaveny, 2009). The chosen resolution seems to be above standard values. Therefore, a resolution of $(36\ \mu m)^3$ was regarded as good compromise between accuracy and computation time.

The overall good r_c in combination with the mean difference ≤ 10 MPa and the low limits of agreement in the Bland-Altman plots between experiments and simulations with wet tissue properties for compression and tension indicates validity of these models. Nevertheless, minor inter-specimen variations were obvious and the one by one comparison between experiment and simulation was not perfect. In case of torsion, the moderate agreement should be attributed to the boundary conditions and not to the models and their parameters.

This study suggests that it is possible to directly set up valid μFE models of vertebral trabecular bone in the linear range. This was possible by using specimen specific or mean effective tissue moduli obtained from nanoindentation under wet testing conditions. Except isotropy, no initial guess on the effective tissue properties was made. Furthermore, no numerical calibration process to obtain them was necessary. The presented models can be considered valid in the linear range.

Chapter 6

Damage Accumulation of Vertebral Trabecular Bone

As published in: Wolfram, U., Wilke, H.-J., Zysset, P. K., 2011. Uniaxial Damage Accumulation in Vertebral Trabecular Bone Depends on Loading ode and Direction. Journal of Biomechanics. 44 (6), 1164 – 1169 ★

6.1 Introduction

Osteoporotic vertebral fractures constitute a major clinical problem in aging societies (Maghraoui et al., 2008). A third of all vertebral fractures is caused by falls, 15% by lifting heavy loads or traffic accidents and 50% are not relatable to single traumatic events (Silva, 2007). In the latter case, vertebrae can show sinter processes which indicate the accumulation of damage and permanent deformation (Keaveny et al., 1994) in a cyclic fatigue fashion. Vertebrae can also accumulate substantial damage after isolated overloads. The associated small permanent deformation is not detectable in clinical radiographs but induces a decrease in stiffness and strength (Kopperdahl et al., 2000). This damage accumulation increases the risk of fracture (Fyhrie and Schaffler, 1994; Burr et al., 1997; Kopperdahl et al., 2000) and may finally lead to collapsing vertebrae. In addition, the ability of bone to repair induced damage decreases with age while bone microdamage increases with age (Waldorff et al., 2007; Burr et al., 1997). Thus, understanding the damage properties of vertebral trabecular bone is important to understand vertebral fractures.

Overloading trabecular bone leads to severe loss of stiffness and accumulation of residual strain (Zysset, 1994; Keaveny et al., 1994, 1999). Qualitatively, this damage accumulation appears to be independent on site, species and density (Keaveny et al., 1994; Zysset and Curnier, 1996; Kopperdahl et al., 2000). Cortical bone shows qualitatively similar damaging behaviour as trabecular bone (Fondrk et al., 1988; Garcia et al., 2010). This suggested that substantial damage occurs at the nanometer level (Keaveny et al., 2001). Cracks and diffuse damage that accumulate within trabeculae cause reductions in apparent modulus prior to failure of whole trabeculae (Wachtel and Keaveny, 1997). This was corroborated by findings that trabecular bone accumulates damage already at apparent strains lower than apparent ultimate strain (Morgan et al., 2005). Trabecular damage leads then to the

formation of fracture bands or greater regions of fractured trabeculae (Moore and Gibson, 2001; Thurner et al., 2006) until overall failure. Thus, damage of trabecular bone is a mixture of microcracking, diffuse damage and fractured trabeculae.

In case of vertebral trabecular bone, macroscopic damage and residual strain evolution leading to vertebral failure could be dependent on the load direction and the loading mode. It was suggested that overloading trabecular bone in one direction is detrimental to loads in a direction perpendicular to it (Shi et al., 2010). Knowledge about the possible anisotropy of macroscopic damage and residual strains may be important for the investigation of vertebral fractures, since vertebral damage caused by daily activities is not restricted to axial compression.

The goals of the study were therefore to: 1) investigate whether the evolution of damage and residual strains in vertebral trabecular bone is different in axial and transverse direction; and 2) whether these evolutions are different under compressive, tensile or torsional loading.

6.2 Materials and Methods

The study included 104 (50 male, 54 female) fresh frozen human vertebrae (T1 – L3) of 32 donors with a median age of 65 y (21 y – 94 y). Vertebrae were stored at $-20°C$ immediately after harvest and randomly assigned to three groups anterior-posterior (AP), cranial-caudal (CC) and latero-lateral (LL). Vertebrae were cleaned from surrounding soft tissue and the posterior structures were partially removed. The remaining posterior parts of the vertebral bodies were moulded in polymethyl-methacrylate (PMMA) (Technovit 3040, Heraeus Kulzer GmbH, Wehrheim, Germany) to enable gripping. Endplates were removed with a band saw (Exakt Apparatebau, Norderstedt, Germany). Subsequently, 251 cylindrical specimens $(8\ \text{mm}$ diameter and $18-25\ \text{mm}$ height$)$ were cored from the remaining slices using a custom made core drill. Marrow was removed from top and bottom of the cylinders using a pulsed water jet (Braun Oral-B Professional Care 6500, Kronberg, Germany) but kept in the middle. Top and bottom of the cylinders were moulded in polyurethane (PU) (SG 2000, ebalta Kunststoff GmbH, Rothenburg ob der Tauber, Germany) so that an approximately 12 mm marrow filled free gage length was left in-between.

Cylinders were submerged in water with 0.9% sodium chloride, scanned in a µCT (µCT 40, SCANCO Medical AG, Brüttisellen, Switzerland) at a resolution of $(12\ \mu\text{m})^3$ and refrozen. Standard morphometric parameters, bone volume fraction ρ and the mean intercept length fabric tensor $\mathbf{M}$ (Hildebrand and Rüegesegger, 1997; Odgaard, 1997) were obtained using IPL (Image Processing Language, SCANCO Medical AG, Brüttisellen, Switzerland). Forty-one CC samples which showed an in-plane degree of anisotropy $DA_{ip} < 1.1$ and a structural misalign-

ment from the cylindrical longitudinal axis $\alpha < 10^\circ$ were selected for torsion testing.

Prior to mechanical testing, specimens were rehydrated for one hour in water with 0.9% sodium chloride. Aluminium rods were glued to the endcaps using cyanoacrylate (Loctite, Henkel Central Eastern Europe GmbH, Austria) to allow proper gripping. An extensometer (Mini-Bionix MTS system, Milwaukee, MN, USA) was attached to the PU endcaps after mounting the specimens on the testing system to measure strain during uniaxial compression (UC) or uniaxial tension (UT) tests. Angular data for the torsion (T) tests were recorded with the rotary variable differential transformer of the testing system. Specimens were preconditioned with three cycles up to $\varepsilon = 0.4\%$ strain at $\dot{\varepsilon}= 0.004\ \frac{1}{\mathrm{s}}$ and loaded strain controlled to five different load steps with three cycles per load step at a rate of $\dot{\varepsilon}= 0.002\ \frac{1}{\mathrm{s}}$ (Table 6.1).

Table 6.1: Load steps $(\varepsilon_i)$for uniaxial compression $\left(\varepsilon^{UC}\right)$, uniaxial tension $\left(\varepsilon^{UT}\right)$ and torsion (γ)

	ε_1	ε_2	ε_3	ε_4	ε_5
ε^{UC} in %	0.4	0.7	1.4	2.5	4.0
ε^{UT} in %	0.4	0.6	1.0	1.6	2.4
γ in %	0.8	1.4	2.8	5.0	8.0

In case of uniaxial compression and uniaxial tension, stress was calculated from the recorded force-strain curve as $\sigma = \frac{F}{A_0}$ with A_0 the initial cross section of the sample. Torque-twist angle curves were denoised using an average filter (Jähne, 2005). Peak apparent torsional stress was computed with radius r, twist-angle/length θ and torque-moment M_T (Nadai, 1950).

$$\tau = \frac{1}{2\pi r^3}\left(\theta\frac{dM_T}{d\theta} + 3M_T\right) \tag{6.1}$$

The derivative $\frac{dM_T}{d\theta}$ was approximated from the denoised torque-twist angle curve with a central difference operator. Accounting for the influence of fixation and PU endcaps, engineering shear strain acting in the free gage length γ_B was calculated by first subtracting the influence of the machine compliance from the angular data and than subtracting strain over the endcaps from strain over the whole sample.

$$\gamma_B = \left(\Delta\vartheta - \frac{M_T}{K_F}\right)\frac{r_S}{\ell_S} - \left(\frac{M_T\ell_{BP}}{J_{BP}\mu_{BP}}\right)\frac{r_{BP}}{\ell_{BP}} \tag{6.2}$$

$\Delta\vartheta$ denotes the twist angle, K_F the fixation stiffness, ℓ_{BP}, r_{BP} endcap length and radius and ℓ_s, r_s sample length and radius. J_{BP} and μ_{BP} denote the polar moment of inertia and the shear modulus of the endcap. $K_F = 17317.31\ \frac{\text{Nmm}}{\text{rad}}$ was determined with seven moulded PU cylinders $(9 \times 20\ \text{mm})$ using the same test protocol as for torsion. A rule of mixture was used to calculate μ_{BP}.

$$\mu_{BP} = v_f \mu_P + \left(1 - v_f\right) \mu_B \tag{6.3}$$

$\mu_P = \epsilon_P / 2\,(1 + \nu)$ was the shear modulus of PU and μ_B of bone which was derived in a similar fashion. Young's modulus for PU was obtained from compression tests on seven moulded PU cylinders $(9 \times 20\ \text{mm})$. It was determined to 2014 MPa using the first load step of the compression test protocol. Young's modulus of bone ϵ_B was directly measured for each sample using nanoindentation (Wolfram et al., 2010a).

Apparent moduli were obtained from the stiffest section of the loading part (Keaveny et al., 1994) of the first cycle per load step of the stress-strain curve using a moving linear regression. Damage was defined as decay in modulus during the load steps ε_i, that is $\epsilon_i = (1 - D_i)\,\epsilon_1$. Residual strains were obtained from the unloading part of the third cycle per load step at the intersection of unloading curve and abscissa. A cubic spline interpolation was performed using the inflexion points of the third cycles per load step (Figure 6.1). This served to obtain quasi-static, monotonic variables such as yield and maximum stress and strain that allow comparison with the literature to judge upon the validity of the experiments. Yield was defined using the 0.2%-offset rule. Maximum was defined as the point were the derivative onto the spline sets vanished (Figure 6.1).

Statistical analyses were performed with R (R Development Core Team, 2008). Outliers were defined as any measurement below the 5th or above the 95th percentile. Due to linear quantile-quantile plots, normal distributions were assumed and t-tests were performed to a significance level of $p < 0.05$.

6.3 Results

Due to early failure and the outlier criterion, 48 out of 251 specimens were excluded. A weak but significant correlation between degree of anisotropy (DA) versus bone volume fraction (ρ) was found $(r^2 = 0.08)$. No statistical significant difference between ρ and DA in CC and AP was found. In LL ρ and DA were 1.16 and 1.02 times higher.

No statistically significant difference was found between ϵ^{AP} and ϵ^{LL}. These directions were pooled to transverse (TR). No statistically significant difference was found between initial stiffness in compression and tension for axial $(\epsilon^{AX}_{UC} = 383.4 \pm 162.9\ \text{MPa},\ \epsilon^{AX}_{UT} = 384.1 \pm 155.1\ \text{MPa})$ and transverse $(\epsilon^{TR}_{UC} = 119.5 \pm 74.2\ \text{MPa},$

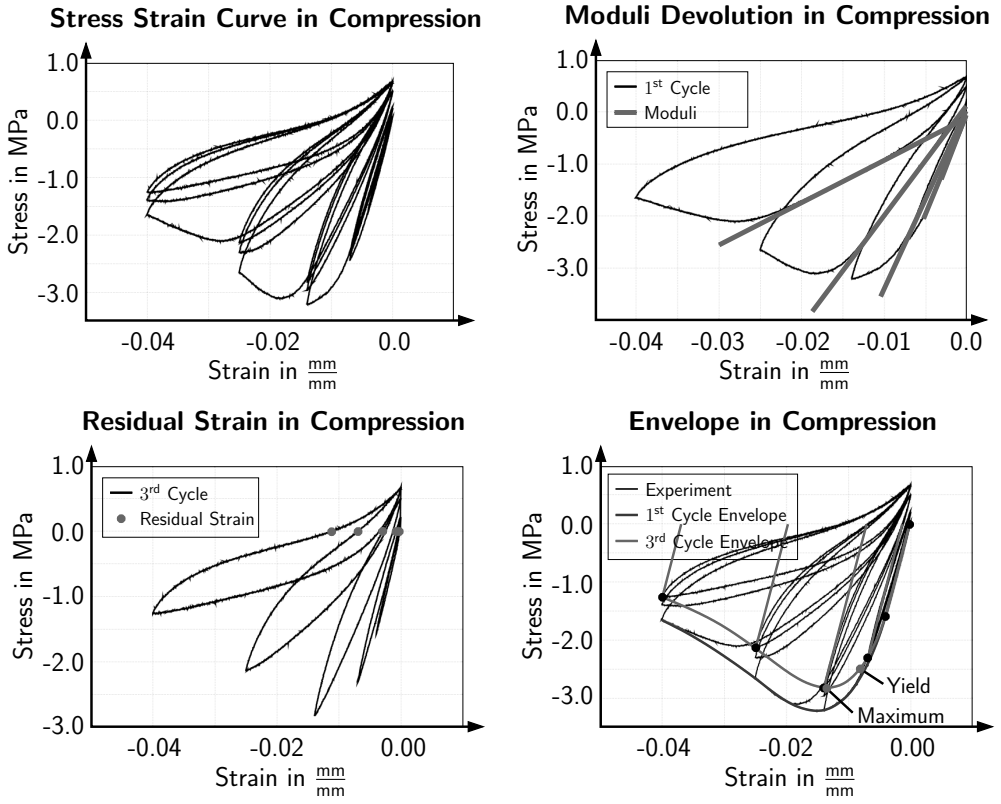

Figure 6.1: The exemplary stress-strain curve clearly shows three conditioning cycles per laodstep. Damage was determined as modulus devolution. Residual strains were determined from the unloading part of the third cycle per load step. The construction of a monotonic stress-strain envelope using the inflexion points of the first or third cycle per load step of the stress-strain curve allowed for the determination of yield and maximum.

$\epsilon_{UT}^{TR} = 129.7 \pm 54.7$ MPa) loading directions. In torsion, initial shear moduli were found to be $\mu = 77.9 \pm 28.6$ MPa.

In compression, no statistically significant difference was found between axial and transverse damage for loadstep ε_2 but for loadsteps ε_3 to ε_5. In tension, statistically significant differences between damage in axial and transverse directions were found for loadsteps ε_3 to ε_5 but not for loadstep ε_2. In compression and tension, damage in axial direction was found to be higher than in transverse direction (Figure 6.2). Maximum stress in axial was reached at lower damage than in transverse loading direction for both compression and tension. Thereafter, higher relative stresses were maintained in transverse direction (Figure 6.3). In torsion, damage increased significantly for all loadsteps γ_1 to γ_5 and was more sigmoidal than in tension and compression (Figure 6.2).

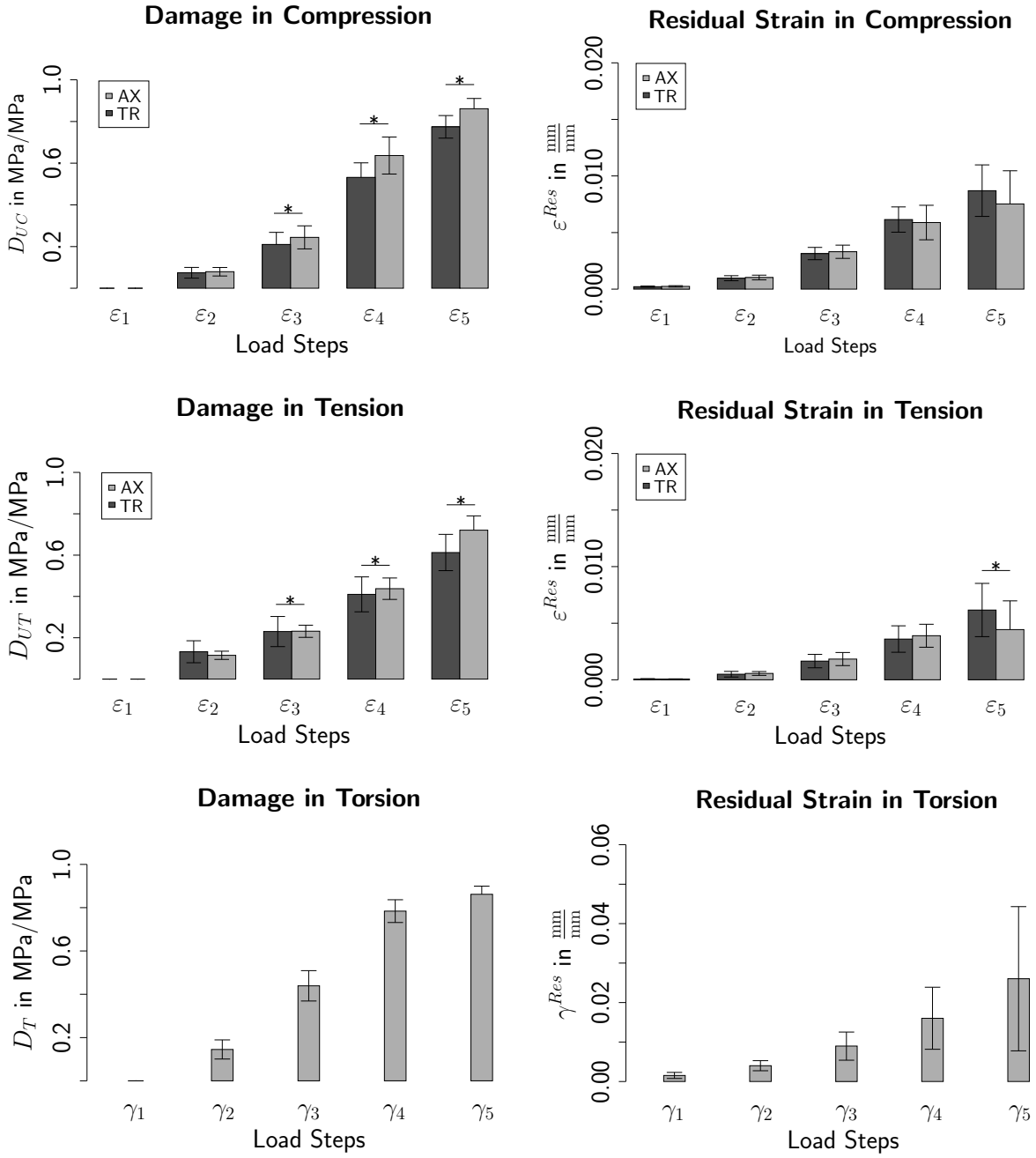

Figure 6.2: Statistically significant more damage (D) was accumulated in axial (AX) than in transverse (TR) load direction. Damage accumulation seems to be more linear in tension (UT) compared to compression (UC) and more sigmoidal in torsion (T) than in compression and tension. No statistically significant difference could be found for residual strains in axial and transverse direction except for loadstep ε_5 in tension. Comparing the loading modes the evolution of residual strains seem qualitatively similar. The whiskers denote ± 1 standard deviation and the asterisk statistical significance to a significance level of $p = 0.05$.

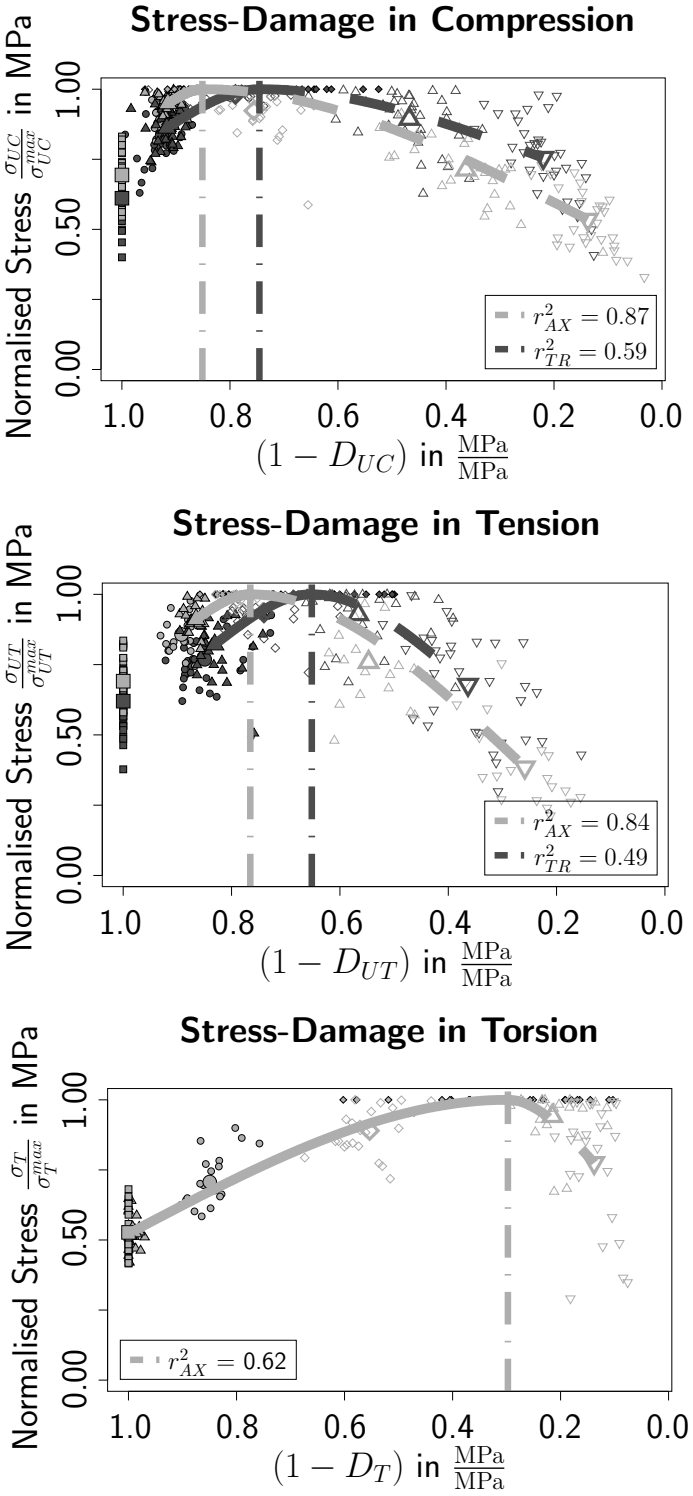

Figure 6.3: Normalised stress-damage ($\frac{\sigma}{\sigma^{max}}$ over $1 - D$) evolutions over all loadsteps show that maximum stress was reached at higher damage and that higher relative stresses are maintained afterwards in transverse loading direction. The dot-dashed lines indicate damage at maximum stress for axial and transverse directions. Comparing compression (UC), tension (UT) and torsion (T) suggests that the stress-damage evolution in different loading modes is not comparable and different in load direction. Stress-damage functions were derived by piecewise cubic spline interpolations through $(\sigma^y,\ D^y)$, $(\sigma^{max},\ D^{max})$ and $(\sigma(\varepsilon_5),\ D(\varepsilon_5))$. Different load steps are shape encoded with $\varepsilon_1 = \blacksquare$, $\varepsilon_2 = \bullet$, $\varepsilon^y = \blacktriangle$, $\varepsilon^{max} = \blacklozenge$, $\varepsilon_3 = \lozenge$, $\varepsilon_4 = \triangle$, $\varepsilon_5 = \triangledown$.

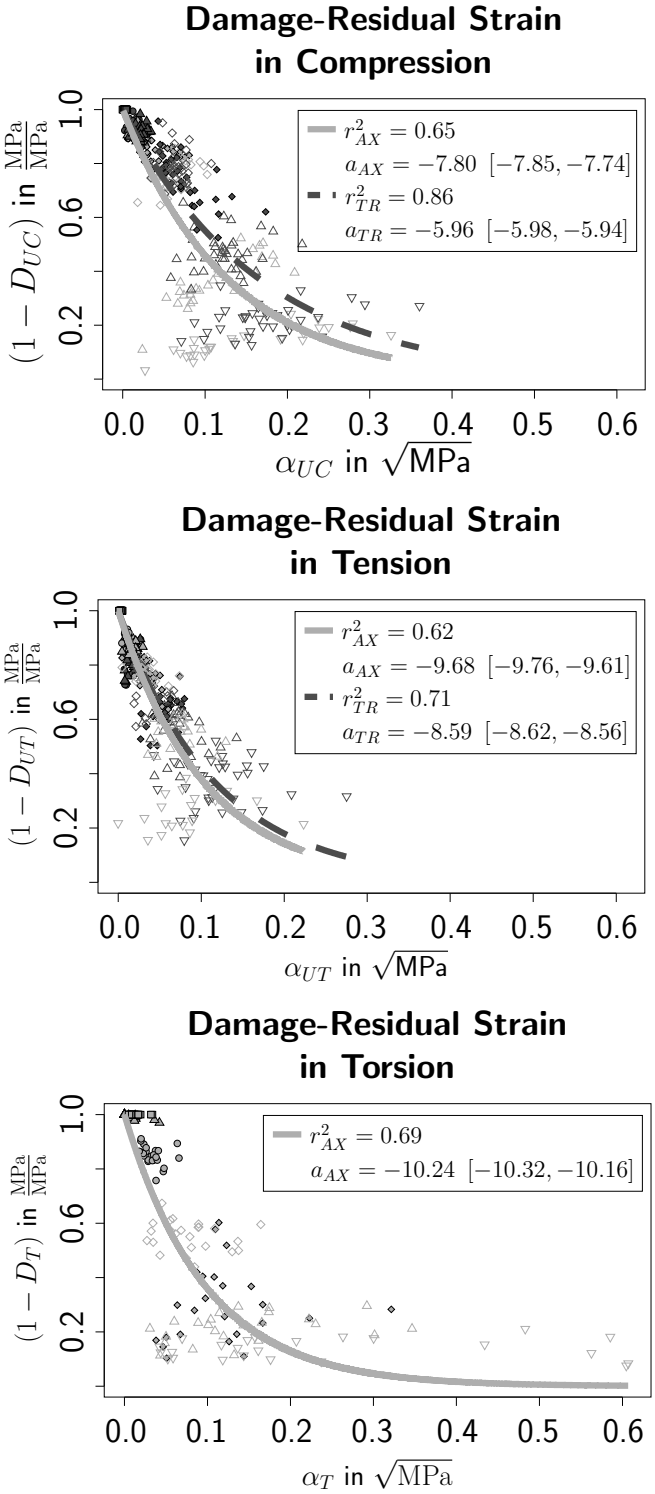

Figure 6.4: Different 95% confidence intervals of the fit-parameter a imply different damage-residual strain evolutions $(1 - D$ over $\alpha)$ in axial and transverse loading direction for compression (UC), tension (UT) and torsion (T). Comparing the loading modes the evolutions seem to be qualitatively similar. The internal variable $\alpha = \sqrt{\epsilon_0}\rho^{\frac{k}{2}} m^l \varepsilon^{res}$ (for compression and tension) or $\alpha = \sqrt{\mu_0}\rho^{\frac{k}{2}} m_{TR}^{\frac{l}{2}} m_{AX}^{\frac{l}{2}} \gamma^{res}$ (for torsion) accounts for the evolution of the residual strains weighted by the respective fabric eigenvalue and stiffness parameter of the fabric based elasticity model. Data was fit to evolution equations $D = 1 - e^{a\alpha}$. Different load steps are shape encoded with $\varepsilon_1 = \blacksquare$, $\varepsilon_2 = \bullet$, $\varepsilon^y = \blacktriangle$, $\varepsilon^{max} = \blacklozenge$, $\varepsilon_3 = \lozenge$, $\varepsilon_4 = \triangle$, $\varepsilon_5 = \triangledown$.

Residual strains increased significantly with each load step for each loading mode. In compression, no statistically significant difference could be found between residual strains in axial and transverse directions. This was found for tension as well except for loadstep ε_5 (Figure 6.2). Regarding the evolution of damage over residual strains, slightly lower damage was observed in transverse directions for both compression and tension. The confidence intervals of the fit parameters in AX and TR did not overlap (Figure 6.4).

Statistically significant differences $\approx$ 5% were found between yield strains in compression and tension. Comparing yield strains in torsion to yield strains in compression and tension these differences were $\approx$ 15% (Figure 6.5). Highest maximum strains were found in torsion. In case of compression and tension, significantly higher maximal strains were obtained in transverse directions. Statistically insignificant differences of $>$ 5% were found between maximum strains in tension and compression for both axial and transverse directions (Figure 6.5).

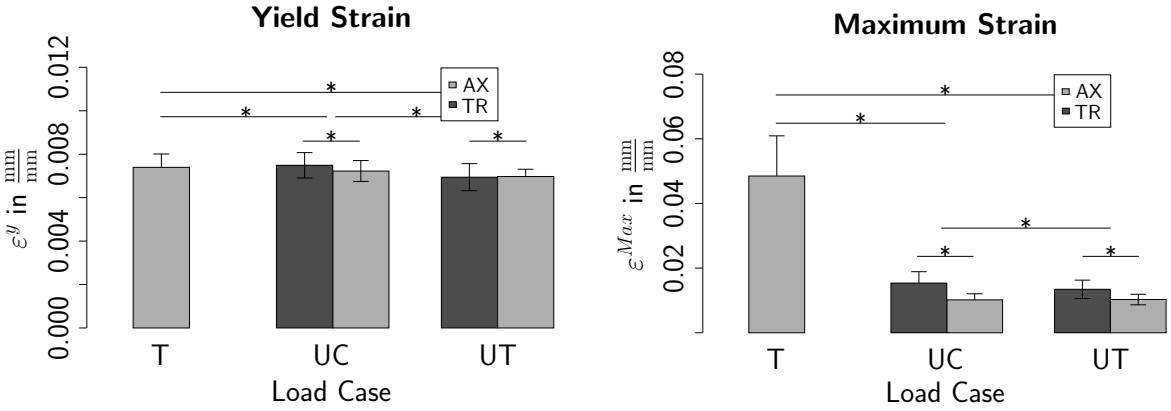

Figure 6.5: Small statistically significant differences were found for yield strains between compression (UC), tension (UT) and torsion (T) and in axial (AX) and transverse (TR) loading direction. Maximum strains showed greater differences between loading directions and modes. The whiskers denote ± 1 standard deviation and the asterisk statistical significance to a significance level of $p = 0.05$.

6.4 Discussion

The goal of this study was to investigate whether damage and residual strain evolution is different in axial and transverse loading direction. Furthermore, it was of interest whether these evolutions are different under different loading modes. Damage (Figure 6.2), stress-damage (Figure 6.3) and damage-residual strain (Figure 6.4) evolutions suggest that different damage but not residual strain evolution mechanisms were present in axial and transverse loading direction. Furthermore, the results indicate that these evolutions are different for different loading modes.

Damage accumulation was qualitatively similar between axial and transverse loading directions in compression and tension with respect to the same strain range. Damage accumulation was lower in transverse direction for both load cases indicating an anisotropic damage process. It seems that less damage but the same amount of residual strain accumulated in transverse direction (Figures 6.3 and 6.4). In torsion, damage accumulation was not comparable to compression or tension. Maximum stress was reached at higher damage compared to compression and tension (Figure 6.3).

In fact, damage accumulation depends on the tissue stress distribution. This in turn, depends on the loading mode. Most bending of trabeculae and therefore the most heterogeneous stress distribution is present under torsion, some trabecular bending in compression and least in tension. On the trabecular length scale, damage occurs primarily at high tensile stresses caused by bending. Therefore, it accumulated more rapidly in torsion, than in compression and finally the least in tension. The progression of damage was also more linear for tension. The same was true for residual strains. The free trabecular bending length is larger in transverse direction, which means that the elastic behaviour extends over a larger strain range and delays the onset of damage and maximum strain (Figure 6.3). Accounting for fabric, the relationship between damage and residual strains showed similar trends for all loading directions and modes (Figure 6.4). However, the non-overlapping confidence intervals of the parameter a suggest that the relationships between damage and residual strains were different in axial and transverse direction. Thus, different damage mechanisms could be present in axial and transverse loading direction.

Since damage is defined as decay in modulus, it is necessary to compare the initial stiffness to the literature. Initial stiffness was higher than those reported for vertebral trabecular bone (Keaveny et al., 1997; Matsuura et al., 2007). Stiffnesses lay in the range found by others (Kopperdahl and Keaveny, 1998; Morgan et al., 2003) or were lower than those found in a study on different sites (Rincón-Kohli and Zysset, 2009). Shear moduli were lower than those found for femoral trabecular bone (Garnier et al., 1999) or from different sites (Rincón-Kohli and Zysset, 2009). Differences may have been due to the higher volume fraction in these studies. Further differences compared to the literature may have arisen from different preparation and testing protocols. However, the obtained results lay in a range comparable to the literature. Thus, the determined stiffnesses were considered usable to determine the damage evolution of vertebral trabecular bone.

Yield and maximum strains serve as markers to integrate the presented results on damage and residual strain evolution in the quasi-static mechanical behaviour of vertebral trabecular bone. Axial yield strains in compression and tension and their statistically significant difference of $\approx 5\%$ were in the lower range reported in

the literature (Kopperdahl and Keaveny, 1998). Comparing the results to data from different sites, ε^y_{UC} was lower while ε^y_{UT} was in a similar range (Rincón-Kohli and Zysset, 2009). Axial ε^y_{UC} laid in the range reported for uniaxial compression (Matsuura et al., 2007). In torsion, the presented yield strains were lower than those found for femoral trabecular bone (Garnier et al., 1999) or for data from different anatomic sites (Rincón-Kohli and Zysset, 2009). This could have been attributable to the noise reduction using a median filter which could have caused offsets affecting the strain determination but not the stiffness determination.

Differences between yield strains in compression and tension were small but lay in a range reported in the literature (Kopperdahl and Keaveny, 1998). Other studies, however, found differences up to 56% (Rincón-Kohli and Zysset, 2009). It was reported that yield strains in compression depend on apparent density respectively bone volume fraction while yield strains in tension do not (Kopperdahl and Keaveny, 1998; Bevill et al., 2009b). Thus, yield strains in compression found in this study could differ from the literature (Rincón-Kohli and Zysset, 2009) due to different bone volume fractions of the samples. However, when obtaining quasi-static data from the first cycles per load step (Figure 6.1) it was found that compressive yield strains $\left(\varepsilon^y_{UC} = 0.0081\right)$ were significantly higher than tensile yield strains $\left(\varepsilon^y_{UT} = 0.0072\right)$. Comparison to the results from the third cycles per load step $\left(\varepsilon^y_{UC} = 0.0073,\ \varepsilon^y_{UT} = 0.0070\right)$ shows that the conditioning in every load step had a greater effect in compression than in tension. It seems that more energy was dissipated in compression leading to balanced yield strains in compression and tension. Still the same caveats regarding bone volume fraction exist with the yield strains obtained from the first cycle per load step.

Axial maximum strains in compression and tension were in the range reported in the literature (Kopperdahl and Keaveny, 1998; Matsuura et al., 2007). Compared to data from tibiae (Ford and Keaveny, 1996) or from different anatomical sites (Rincón-Kohli and Zysset, 2009) the mean was lower. The higher maximal strains obtained in transverse directions fitted better to the literature. In torsion, maximum strains were comparable to data from different anatomical sites (Rincón-Kohli and Zysset, 2009). The conditioning effect observed for the yield strains could have led to lower maximal strains as well. In conclusion, the results for yield and maximum strains support the validity of the experiment and, thus, the conclusions derived upon the damage mechanisms.

Load rates for quasi-static testing in this study have been slower than rates reported earlier (Bayraktar et al., 2004b; Morgan and Keaveny, 2001; Morgan et al., 2005; Rincón-Kohli and Zysset, 2009). Three conditioning cycles in each load step allowed for distinction of a loading part which included pore fluid and other influences on an elastic response and an unloading part after three conditioning cycles which reflects a settled quasi-static load situation. This settled load situ-

ation in the third unloading cycle in load step ε_i was almost equal to the new loading cycle ε_{i+1} (Figure 6.1). Regarding the observed effect on ε^y the conditioning seems to minimise viscous effects already after one cycle. Thus, damage values obtained from the loading path of the first cycle represent an initial response and the residual strains from the unloading path of the third cycle represent a settled response. A drawback was the high number of failed samples. This was due to failure of the glue joints in higher loadsteps which did not stand the cyclic high amplitudes. Dropping the outlier criterion and reperforming statistical evaluation with nonparametric statistics did not lead to changes in the results. Thus, the used statistics seem to be reasonable.

This paper provides detailed insights in the damage and residual strain evolution of vertebral trabecular bone under different uniaxial loading modes. Damage but not the residual strain evolution seems to be anisotropic and both seem and both seem to evolve differently under different loading modes. This indicates that different damage mechanisms are present under different loading directions. The results could help to improve the understanding and numerical assessment of vertebral fractures.

Chapter 7

Conclusion

Osteoporosis constitutes a major problem in ageing societies. The disease is characterised by a loss of bone mass and a decrease in fracture load. Incidents, such as falls, leading to vertebral fractures potentially increase with age while the ability of bone to repair induced damage and reestablish the bone strength decreases with age. To identify those vertebrae at risk of fracture and also to prevent vertebral fractures it is important to understand the mechanical properties of vertebral trabecular bone. Therefore, this PhD thesis was concerned with the improvement of our knowledge about the mechanical properties of vertebral trabecular bone over different length scales.

On a macroscopic scale, the material properties can be approximated by bone volume fraction and fabric. While bone volume fraction could be at least approximated via CT based bone mineral density measurements, it was unclear whether the trabecular orientation can be determined in clinical settings. An experimental protocol was proposed that allowed for the comparison of μCT and clinical CT and showed that at least the trabecular main direction can be determined from clinical scans. This forms the basis for applying volume fraction and fabric based material laws for determining patient specific fracture loads.

Clinical CT does not allow to investigate the deterioration of mechanical properties on microscopic length scales. Thus, it was necessary to investigate the mechanical properties on the microscale and how these may be influenced by patient related factors such as age and gender. Using nanoindentation, transverse isotropic stiffness tensors for vertebral trabecular bone matrix were determined which reflect the dependence of the mechanical properties of bone extra cellular matrix on the loading direction. Its stiffness remains unaffected by age, gender and vertebral level while the work to perform an indentation was affected by age. This means that the alteration of the macroscopic stiffness is a structural problem and not due to changing microscopic material properties. However, whether this is true for post yield properties such as strength remains unanswered.

The fact, that the alteration of the macroscopic stiffness is a structural problem was further corroborated in a combined numerical and experimental study. The study aimed at setting up valid μFE models from μCT scans and nanoindentation measurements. It showed first, that it is possible to set up valid μFE models to determine macroscopic material properties of vertebral trabecular bone directly.

Second, it corroborated the concept that the macroscopic mechanical properties are governed by trabecular structure and that similar tissue stiffness can be assumed for all samples.

Based on these observations, the use of clinical CT based FE models seems reasonable. However, vertebral fractures constitute a nonlinear problem and clinical CT datasets do not contain any information about already induced damage that increases fracture susceptibility. Therefore, knowledge about the damage properties of vertebral trabecular bone is mandatory. An experimental study was performed to investigate the damage properties of vertebral trabecular bone under uniaxial compression, tension or torsion. The study implies that isotropic representations of the post yield behaviour are not sufficient for the determination of vertebral fracture load. The damage mechanisms leading to vertebral collapse due to overloads are different in different anatomic load directions.

In summary, this thesis provides a conjoint dataset of the mechanical properties of vertebral trabecular bone from the microscale to the macroscale. These are the relevant scales for determining vertebral fracture load. To the author's knowledge this is the biggest conjoint dataset about multiscale mechanical properties for vertebral trabecular bone so far.

Chapter 8

Bibliography

Andresen, R., Radmer, S., Hakim, S., Banzer, D., 2006. The current state of osteoporosis diagnostics using spinal QCT. Osteoporosis International 6 (S1), 188.

Arbenz, P., van Lenthe, G., Mennel, U., Müller, R., Sala, M., 2008. A scalable multi-level preconditioner for matrix-free μ-finite element analysis of human bone structures. International Journal of Numerical Methods in Engineering 73 (7), 927 – 947.

Banse, X., Devogelaer, J. P., Munting, E., Delloye, C., Cornu, O., Grynpas, M., 2001. Inhomogeneity of human vertebral cancellous bone: systematic density and structure patterns inside the vertebral body. Bone 28 (5), 563 – 571.

Bayraktar, H. H., Gupta, A., Kwon, R. Y., Papadopoulos, P., Keaveny, T. M., 2004a. The modified super-ellipsoid yield criterion for human trabecular bone. Journal of Biomechanical Engineering 126 (6), 677 – 684.

Bayraktar, H. H., Morgan, E. F., Niebur, G. L., Morris, G. E., Wong, E. K., Keaveny, T. M., 2004b. Comparison of the elastic and yield properties of human femoral trabecular and cortical bone tissue. Journal of Biomechanics 37 (1), 27 – 35.

Bevill, G., Eswaran, S. K., Farahmand, F., Keaveny, T. M., 2009a. The influence of boundary conditions and loading mode on high-resolution finite element-computed trabecular tissue properties. Bone 44 (4), 573 – 578.

Bevill, G., Farhamand, F., Keaveny, T. M., 2009b. Heterogeneity of yield strain in low-density versus high-density human trabecular bone. Journal of Biomechanics 42 (13), 2165 – 2170.

Bevill, G., Keaveny, T. M., 2009. Trabecular bone strength predictions using finite element analysis of micro-scale images at limited spatial resolution. Bone 44 (4), 579 – 584.

Bikle, D. D., Halloran, B. P., Morey-Holton, E., 1997. Space flight and the skeleton: lessons for the earthbound. The Endocrinologist 7 (1), 10 – 22.

Birkenhäger-Frenkel, D. H., Nigg, A. L., Hens, C. J. J., Birkenhäger, J. C., 1993. Changes of interstitial bone thickness with age in men and women. Bone 14 (3), 211 – 216.

Bland, J. M., Altman, D. G., 1986. Statistical methods for assessing agreement between two methods of clinical measurement. Lancet 1 (8476), 307 – 310.

Bonjour, J. P., Theintz, G., Law, F., Slosman, D., Rizzoli, R., 1994. Peak bone mass. Osteoporosis International S1, 7 – 13.

Boyde, A., Elliott, J. C., Jones, S. J., 1993. Stereology and histogram analysis of backscattered electron images: age changes in bone. Bone 14 (3), 205 –210.

Brennan, O., Kennedy, O. D., Lee, T. C., Rackard, S. M., OBrien, F. J., 2009. Biomechanical properties across trabeculae from the proximal femur of normal and ovariectomised sheep. Journal of Biomechanics 42 (4), 498 – 503.

Brosper, P. J., Schulte, R., Roth, A., Helmchen, F., Waters, J., Lang, S., Sakmann, B., Wittum, G., 2005. Nonlinear anisotropic diffusion filtering of three-dimensional image data from 2-photon microscopy. In: Dougherty, E. R., Astola, J. T., Egiazarian, K. O. (Eds.), Proceedings of SPIE. Vol. 5672. Society of Photo-Optical Instrumentation Engineers, pp. 44 – 69.

Burr, D. B., Forwood, M. R., Fyhrie, D. P., Martin, R. B., Schaffler, M. B., Turner, C. H., 1997. Bone microdamage and skeletal fragility in osteoporotic and stress fractures. Journal of Bone and Mineral Research 12 (1), 6 – 15.

Bushby, A. J., Ferguson, V. L., Boyde, A., 2004. Nanoindentation of bone: Comparison of specimens tested in liquid and embedded in polymethylmethacrylate. Journal of Materials Research 19 (1), 249 – 259.

Chapuy, M. C., Pamphile, R., Paris, E., Kempf, C., Schlichting, M., Arnaud, S., Garnero, P., Meunier, P. J., 2002. Combined calcium and vitamin d3 supplementation in elderly women: confirmation of reversal of secondary hyperparathyroidism and hip fracture risk: the decalyos ii study. Osteoporosis International 13 (3), 257 – 264.

Chevalier, Y., Pahr, D., Allmer, H., Charlebois, M., Zysset, P., 2007. Validation of a voxel-based FE method for prediction of the uniaxial apparent modulus of human trabecular bone using macroscopic mechanical tests and nanoindentation. Journal of Biomechanics 40 (15), 3333 – 3340.

Chevalier, Y., Pahr, D., Zysset, P. K., 2009. The role of cortical shell and trabec-

ular fabric in finite element analysis of the human vertebral body. Journal of Biomechanical Engineering 131 (11), 111003–1 – 111003–12.

Cooper, C., 1993. The epidemiology of fragility fractures: Is there a role for bone quality? Calcified Tissue International 53, S23 – S26.

Cowin, S. C., 1985. The relationship between the elasticity tensor and the fabric tensor. Mechanics of Materials 4, 137 – 147.

Cowin, S. C. (Ed.), 2001. Bone Mechanics Handbook. CRC Press.

Crawford, P. R., Cann, C. E., Keaveny, T. E., 2003a. Finite element models predict in-vitro vertebral body compressive strength better than quantitative computed tomography. Bone 33 (4), 744 – 750.

Crawford, P. R., Rosenberg, W. S., Keaveny, T. M., 2003b. Quantitativ computed tomography-based finite element models of the human lumbar vertebral body: Effect of element size on stiffness, damage, and fracture strength predictions. Journal of Biomechanical Engineering 125, 434 – 438.

Crawley, M. J., 2005. Statistics – An Introduction using **R**. John Wiley & Sons, Ltd.

Curnier, A., He, Q. C., Zysset, P. K., 1995. Conewise linear elastic materials. Journal of Elasticity 37, 1 – 38.

Delmas, P. D., van de Langerijt, L., Watts, N. B., Eastell, R., Genant, H., Grauer, A., Cahall, D. L., 2005. Underdiagnosis of vertebral fractures is a worldwide problem: The impact study. Journal of Bone and Mineral Research 20 (4), 557 – 563.

Dempster, W. T., Liddicoat, R. T., 1952. Compact bone as a non-isotropic material. American Journal of Anatomy 91 (3), 331 – 362.

Donahue, S. W., McGee, M. E., Harvey, K. B., Vaughan, M. R., Robbins, C. T., 2006. Hibernating bears as a model for preventing disuse osteoporosis. Journal of Biomechanics 39, 1480 – 1488.

EFFO, NOF, 1997. Who are candidates for prevention and treatment for osteoporosis? Osteoporosis International 7 (1), 1 – 6.

Eisenmenger, M., Pötzsch, O., Sommer, B., 2006. Bevölkerung Deutschlands bis 2050 – 11. koordinierte Bevölkerungsvorausberechnung. Tech. rep., Statistisches Bundesamt.

Eswaran, S. K., Gupta, A., Adams, M. F., Keaveny, T. M., 2006. Cortical and trabecular load sharing in the human vertebral body. Journal of Bone and Mineral Research 21 (2), 307 – 314.

Fan, Z., Rho, J.-Y., 2003. Effects of viscoelasticity and time-dependent plasticity on nanoindentation measurements of human cortical bone. Journal of Biomedical Materials Research Part A 67 A, 208 – 214.

Faulkner, K. G., Cann, C. E., Hasegawa, B. H., 1991. Effect of bone distribution on vertebral strength: Assessment with patient-specific nonlinear finite element analysis. Radiology 179, 669 – 674.

Fondrk, M., Bahniuk, E., Davy, D. T., Michaels, C., 1988. Some viscoplastic characteristics of bovine and human cortical bone. Journal of Biomechanics 21 (8), 623 – 630.

Ford, C. M., Keaveny, T. M., 1996. The dependence of shear failure properties of trabecular bone on apparent density and trabecular orientation. Journal of Biomechanics 29 (10), 1309 – 1317.

Franzoso, G., Zysset, P. K., 2009. Elastic anisotropy of human cortical bone secondary osteons measured by nanoindentation. Journal of Biomechanical Engineering 131, 021001–1 – 021001–11.

Fratzl, P., Weinkamer, R., 2007. Nature's hierarchical materials. Progress in Materials Science 52 (8), 1263 – 1334.

Frost, H. M., 1997. On our age-related bone loss: insights from a new paradigm. Journal of Bone and Mineral Research 12 (10), 1539 –1546.

Fyhrie, D. P., Schaffler, M. B., 1994. Failure mechanisms in human vertebral cancellous bone. Bone 15 (1), 105 – 109.

Garcia, D., Zysset, P. K., Charlebois, M., Curnier, A., 2009. A three-dimensional elastic plastic damage constitutive law for bone tissue. Biomechanics and Modelling in Mechanobiology 8, 149 – 165.

Garcia, G., Zysset, P. K., Charlebois, M., Curnier, A., 2010. A 1d elastic plastic damage constitutive law for bone tissue. Archive of Applied Mechanics 80 (5), 543 – 555.

Garnier, K. B., Dumas, R., Rumelhart, C., Arlot, M. E., 1999. Mechanical characterization in shear of human femoral cancellous bone: torsion and shear tests. Med

Eng Phys 21 (9), 641– 649.

Gong, H., Zang, M., Ling, Q., Lee, K. K. H., Guo, X., Shi, S.-Q., 2006. Regional variations in microstructural properties of vertebral trabeculae with structural groups. Spine 31 (1), 24 – 32.

Goulet, R. W., Goldstein, S. A., Ciarelli, M. J., Kuhn, J. L., Brown, M. B., Feldkamp, L. A., 1994. The relationship between the structural and orthogonal compressive properties of trabecular bone. Journal of Biomechanics 27 (4), 375 – 389.

Guerin, H., Elliott, D., 2006. Degeneration affects the fiber reorientation of human annulus fibrosus under tensile load. Journal of Biomechanics 39 (8), 1410 – 1418.

Haddok, S. M., Yeh, O. C., Mummaneni, P. V., Rosenberg, W. S., Keaveny, T. M., 2004. Similarity in the fatigue behavior of trabecular bone across site and species. Journal of Biomechanics 37 (2), 181 – 187.

Hannan, M. T., Tucker, K. L., Dawson-Hughes, B., Cupples, L. A., Felson, D. T., Kiel, D. P., 2000. Effect of dietary protein on bone loss in elderly men and women: The framingham osteoporosis study. Journal of Bone and Mineral Research 15 (12), 2504 – 2512.

Harrigan, T. P., Jasty, M., Mann, R. W., Harris, W. H., 1988. Limitations of the continuum assumption in cancellous bone. Journal of Biomechanics 21 (4), 269 – 275.

Harrigan, T. P., Mann, R. W., 1984. Characterisation of microstructural anisotropy in orthotropic materials using a second rank tensor. Journal of Materials Sciences 19, 761 – 767.

He, Q.-C., Curnier, A., 1995. A more fundamental approach to damaged elastic stress-strain relations. International Journal of Solids and Structures 32, 1433 – 1457.

Helgason, B., Perilli, E., Schileo, E., Taddei, F., Brynjólfsson, S., Viceconti, M., 2008. Mathematical relationships between bone density and mechanical properties: A literature review. Clinical Biomechanics 23 (2), 135 – 146.

Hengsberger, S., Enstroem, J., Peyrin, F., Zysset, P. K., 2003. How is the indentation modulus of bone tissue related to its macroscopic elastic response? A validation study. Journal of Biomechanics 36 (10), 1503 – 1509.

Hengsberger, S., Kulik, A., Zysset, P. K., 2002. Nanoindentation discriminates the

elastic properties of individual human bone lamellae under dry and physiological conditions. Bone 30 (1), 178 – 184.

Hildebrand, T., Rüegesegger, P., 1997. A new method for the model-independent assessment of thickness in three-dimensional images. Journal of Microscopy 185 (1), 67 – 75.

Hoffler, C. E., Guo, X. E., Zysset, P. K., Goldstein, S. A., 2005. An application of nanoindentation technique to measure bone tissue lamellae properties. Journal of Biomechanical Engineering 127 (7), 1046 – 1053.

Hoffler, C. E., Moore, K. E., Kozloff, K., Zysset, P. K., Brown, M. B., Goldstein, S. A., 2000a. Heterogeneity of bone lamellar-level elastic moduli. Bone 26 (6), 603 – 609.

Hoffler, C. E., Moore, K. E., Kozloff, K., Zysset, P. K., Goldstein, S. A., 2000b. Age, gender, and bone lamellae elastic moduli. Journal of Orthopaedic Research 18 (3), 432 – 437.

Huang, Z., Himes, J. H., McGovern, P. G., 1998. Nutrition and subsequent hip fracture risk among a national cohort of white women. American Journal of Epidemiology 144 (2), 124 – 134.

Ito, M., Hayashi, K., Ishida, Y., Uetani, M., Yamada, M., Ohki, M., Nakamura, T., 1997. Discrimination of spinal fracture with various bone mineral measurements. Calcified Tissue International 60, 11 – 15.

Jähne, B., 2002. Digitale Bildverarbeitung. Springer.

Jähne, B., 2005. Digital Image Processing. Springer-Verlag Berlin Heidelberg New York.

Jaschouz, D., Paris, O., Roschger, P., Hwang, H.-S., Fratzl, P., 2003. Pole figure analysis of mineral nanoparticle orientation in individual trabecula of human vertebral bone. Journal of Applied Crystallography 36, 494 – 498.

Jee, W., 1983. Histology: cell and tissue biology, 5th Edition. Ch. The skeletal tissues.

Jiang, Y., Zhao, J., Augat, P., Ouyang, X., Lu, Y., Majumdar, S., Genant, H. K., 1998. Trabecular bone mineral and calculated structure of human bone specimens scanned by peripheral quantitative computed tomography: Relation to biomechanical properties. Journal of Bone Mineral Research 13, 1783–1790.

Johnell, O., Kanis, J. A., 2006. An estimate of the worldwide prevalence and disability associated with osteoporotic fractures. Osteoporosis International 17, 1726 – 1733.

Kabel, J., Rietbergen, B. v., Dalstra, M., Odgaard, A., Huiskes, R., 1999. The role of an effective isotropic tissue modulus in the elastic properties of cancellous bone. Journal of Biomechanics 32, 673 – 680.

Kanis, J. A., 2002. Diagnosis of osteoporosis and assessment of fracture risk. Lancet 359, 1929 – 1936.

Kanis, J. A., Johnell, O., 2005. Requirements for dxa for the management of osteoporosis in europe. Osteoporosis International 16 (3), 229 – 238.

Kanis, J. A., Johnell, O., De Laet, C., Johansson, H., Oden, A., Delmas, P., Eisman, J., Fujiwara, S., Garnero, P., Kroger, H., McCloskey, E. V., Mellstrom, D., Melton III, J. L., Pols, H., Reeve, J., Silman, A., Tenenhouse, A., 2004. A meta-analysis of previous fracture and subsequent fracture risk. Bone 35 (2), 375 – 382.

Karlsson, M., Obrant, C., Josefsson, P. O., 2005. Osteoporotic fractures Rockwood and Green's fractures in adults. Lippincott Williams & Wilkins.

Keaveny, T., Yeh, O., 2002. Architecture and trabecular bone — toward an improved understanding of the biomechanical effects of age, sex and osteoporosis. Journal of Musculoskeletal and Neuronal Interactions 2 (3), 205 – 208.

Keaveny, T. M., Morgan, E. F., Niebur, G. L., Yeh, O. C., 2001. Biomechanics of trabecular bone. Annual Review of Biomedical Engineering 3, 307 – 333.

Keaveny, T. M., Pinilla, T. P., Crawford, R. P., Kopperdahl, D. L., Lou, A., 1997. Systematic and random errors in compression testing of trabecular bone. Journal of Orthopaedic Research 15 (1), 101 – 110.

Keaveny, T. M., Wachtel, E. F., Guo, X. E., Hayes, W. C., 1994. Mechanical behavior of damaged trabecular bone. Journal of Biomechanics 27 (11), 1309 – 1318.

Keaveny, T. M., Wachtel, E. F., Kopperdahl, D. L., 1999. Mechanical behavior of human trabecular bone after overloading. Journal of Orthopaedic Research 17 (3), 346 – 353.

Kiusalaas, J., 2005. Numerical Methods in Engineering with Python. Cambridge University Press.

Klein-Nulend, J., Bacabac, R.G.and Mullender, M., 2005. Mechanobiology of bone tissue. Pathologie Biologie 53, 576 – 580.

Kopperdahl, D. L., Keaveny, T. M., 1998. Yield strain behaviour of trabecular bone. Journal of Biomechanics 31 (7), 601 –608.

Kopperdahl, D. L., Pearlman, J. L., Keaveny, T. M., 2000. Biomechanical consequences of an isolated overload on the human vertebral body. Journal of Orthopaedic Research 18 (5), 685 – 690.

Kornak, U., Mundlos, S., 2003. Genetic disorders of the skeleton: A developmental approach. American Journal of Human Genetics 73, 447 − 474.

Lee, T. C., O'Brien, F. J., Gunnlaugsson, T., Parkesh, R., Taylor, D., 2006. Microdamage and bone mechanobiology. Technology and Health Care 14, 359 – 365.

Lennox, A. R., Goodship, A. E., 2008. Polar bears (ursus maritimus), the most evolutionary advanced hibernators, avoid significant bone loss during hibernation. Comparative Biochemistry and Physiology - Part A: Molecular & Integrative Physiology 149 (2), 203 – 208.

Lewis, G., Nyman, J. S., 2008. The use of nanoindentation for characterizing the properties of mineralized hard tissues: State-of-the art review. Journal of Biomedical Materials Research. Part B, Applied biomaterials 288 – 303 (1), 87.

Liebschner, M. A. K., Kopperdahl, D. L., Rosenberg, W. S., Keaveny, T. M., 2003. Finite element modeling of the human thoracolumbar spine. Spine 28 (6), 559 – 656.

Lin, L. K., 1989. A concordance correlation coefficient to evaluate reproducibility. Biometrics 45 (1), 255 – 268.

Linden, J. C. v. d., Birkenhager-Frenkel, D. H., Verhaar, J., Weinans, H., 2001. Trabecular bone's mechanical properties are affected by its non-uniform mineral distribution. Journal of Biomechanics 34, 1573 —- 1580.

Magerl, F., Aebi, M., Gertzbein, S. D., Harms, J., Nazarian, S., 1994. A comprehensive classification of thoracic and lumbar injuries. European Spine Journal 3 (4), 184 – 201.

Maghraoui, A. E., Mounach, A., Gassim, S., Ghazi, M., Sep 2008. Vertebral fracture assessment in healthy men: Prevalence and risk factors. Bone 43 (3), 544–548.

Martin, R. B., 2002. Is all cortical bone remodeling initiated by microdamage? Bone 30 (8), 8 – 13.

Matsuura, M., Eckstein, F., Lochmüller, E., Zysset, P., 2007. The role of fabric in the quasi-static compressive mechanical properties of human trabecular bone from various anatomical locations. Biomechanics and Modelling in Mechanobiology 7 (1), 27 – 42.

Mazza, G., Franzoso, G., Pretterklieber, M., Zysset, P. K., 2008. Anisotropic elastic properties of vertebral compact bone measured by microindentation. In: Journal of Biomechanics. Abstracts of the 16th Congress, European Society of Biomechanics. Vol. 41.

Mc Donnell, P., Mc Hugh, P. E., O' Mahoney, D., 2007. Vertebral osteoporosis and trabecular bone quality. Annals of Biomedical Engineering 35 (2), 170 – 189.

Melton, L. J. I., Chrischilles, E. A., Cooper, C., Lane, A. W., Riggs, B. L., 1992. Perspective. How many women have osteoporosis? Journal of Bone Mineral Research 7 (9), 1005 – 1010.

Mittra, E., Akella, S., Qin, Y.-X., 2006. The effects of embedding material, loading rate and magnitude, and penetration depth in nanoindentation of trabecular bone. Journal of Biomedical Materials Research Part A 79 (1), 86 – 93.

Moore, T. L., Gibson, L. J., 2001. Modeling modulus reduction in bovine trabecular bone damaged in compression. Journal of Biomechanical Engineering 123 (6), 613 – 622.

Morgan, E. F., Bayraktar, H. H., Keaveny, T. M., 2003. Trabecular bone modulus-density relationships depend on anatomic site. Journal of Biomechanics 36 (7), 897 –904.

Morgan, E. F., Bayraktar, H. H., Yeh, O. C., Majumdar, A., Burghardt, A., Keaveny, T. M., 2004. Contribution of inter-site variations in architecture to trabecular bone apparent yield strains. Journal of Biomechanics 37, 1413 – 1420.

Morgan, E. F., Keaveny, T. M., 2001. Dependence of yield strain of human trabecular bone on anatomic site. Journal of Biomechanics 34, 569 – 577.

Morgan, E. F., Yeh, O. C., Keaveny, T. M., 2005. Damage in trabecular bone at small strains. Jouropean Journal of Morphology 42, 13 – 21.

Müller, R., Rüegsegger, P., 1995. Three-dimensional finite element modelling

of non-invasively assessed trabecular bone structures. Medical Engineering & Physics 17, 126 – 133.

Nadai, A., 1950. Torsion of a round bar. The stress-strain curve in shear. McGraw-Hill Book Company, Inc. New York, Toronto and London, Ch. 21, pp. 347 – 352.

Niebur, G. L., Feldstein, M. J., Yuen, J. C., Chen, T. J., Keaveny, T. M., 2000. High-resolution finite element models with tissue strength asymmetry accurately predict failure of trabecular bone. Journal of Biomechanics 33 (12), 1575 – 1583.

Odgaard, A., 1997. Three-dimensional methods for quantification of cancellous bone architecture. Bone 20 (4), 315 – 328.

Oliver, W., Pharr, G., 1992. An improved technique for determining hardness and elastic modulus using load and displacement sensing indentation experiments. Journal of Materials Research 7 (6), 1564 – 1583.

R Development Core Team, 2008. R: A Language and Environment for Statistical Computing. R Foundation for Statistical Computing, Vienna, Austria, ISBN 3-900051-07-0.
URL `http://www.R-project.org`

Raisz, L. G., 2005. Pathogenesis of osteoporosis: concepts, conflicts, and prospects. Journal of Clinical Investigation 115, 3318 – 3325.

Randell, A., Sambrook, P. N., Nguyen, T. V., Lapsley, H., Jones, G., Kelly, P. J., Eisman, J. A., 1995. Direct clinical and welfare costs of osteoporotic fractures in elderly men and women. Osteoporosis International 5 (6), 427 – 432.

Rao, R. A., Schunk, B. G., 1991. Computing oriented texture fields. CVGIP: Graph. Models Image Process. 53 (2), 157–185.

Rao, R. D., Singrakhia, M. D., 2003. Painful osteoporotic vertebral fracture. Journal of Bone and Joint Surgery 85A (10), 2010 –2022.

Reinhold, M., Knop, C., Beisse, R., Audigé, L., Kandziora, F., Pizanis, A., Pranzl, R., Gercek, E., Schultheiss, M., Weckbach, A., Bühren, V., Blauth, M., 2009. Operative Behandlung traumatischer Frakturen der Brust- und Lendenwirbelsäule – teil i: Epidemiologie. Der Unfallchirurg 112 (1), 33 – 45.

Rho, J., Tsui, T. Y., Pharr, G. M., 1999. Elastic properties of microstructural components of human bone tissue as measured by nanoindentation. Journal of Biomed-

ical Materials Research 45 (1), 48 – 58.

Rho, J. Y., Kuhn-Spearing, L., Zioupos, P., 1998. Mechanical properties and the hierarchical structure of bone. Medical Engineering & Physics 20 (2), 92 – 102.

Rho, J.-Y., Tsui, T. Y., Pharr, G. M., 1997. Elastic properties of human cortical and trabecular lamellar bone measured by nanoindentation. Biomaterials 20 (18), 1325 – 1330.

Rietbergen, B. v., Huiskes, R., Eckstein, F., Rüegsegger, P., 2003. Trabecular bone tissue strains in the healthy and osteoporotic human femur. J. Bone Miner. Res. 18 (10), 1781 – 1788.

Rietbergen, B. v., Odgaard, A., Kabel, J., Huiskes, R., 1996. Direct mechanics assesment of elastic constants of elastic symmetries and properties of trabecular bone architecture. Journal of Biomechanics 29 (12), 1653 – 1657.

Rietbergen, B. v., Odgaard, A., Kabel, J., Huiskes, R., 1998. Relationships between bone mophology and bone elastic properties can be accurately quantified using high-resolution computer reconstructions. Journal of Orthopaedic Research 16, 23 – 28.

Rietbergen, B. v., Weinans, H., Huiskes, R., Odgaardt, A., 1995. A new method to determine trabecular bone elastic properties and loading using micromechanical finite-element models. Journal of Bioimechanics 28 (1), 69 – 81.

Riggs, B. L., Melton III, J. L., 1983. Evidence for two distinct syndromes of involutional osteoporosis. American Journal of Medicine 75 (6), 899 – 901.

Rincón-Kohli, L., Zysset, P., 2009. Multi-axial mechanical properties of human trabecular bone. Journal of Biomechanics and Modelling in Mechanobiology 8 (3), 195 – 208.

Rokita, E., Chevallier, P., Mutsaers, P. H. A., Tabor, Z., Wróbel, A., 2005. Studies of crystal orientation and calcium distribution in trabecular bone. Nuclear Instruments and Methods in Physics Research Section B: Beam Interactions with Materials and Atoms 240 (1 – 2), 69 – 74.

Roschger, P., Paschalis, E. P., Fratzl, P., Klaushofer, K., 2008. Bone mineralization density distribution in health and disease. Bone 42, 456 – 466.

Rotter, M., Berg, A., Langenberger, H., Grampp, S., Imhof, H., Moser, E., 2001. Autocorrelation analysis of bone structure. Journal of Magnetic Resonance Im-

ageing 14, 87 – 93.

Roux, W., 1881. Der Kampf der Theile im Organismus: Ein Beitrag zur Vervollständigung der mechanischen Zweckmässigkeitslehre. W. Engelmann Leipzig.

Roy, M. E., Rho, J., Tsui, T. Y., Evans, N. D., Pharr, G. M., 1999. Mechanical and morphological variation of the lumbar vertebral cortical and trabecular bone. Journal of Biomedical Materials Research 44 (2), 191 – 197.

Sachs, L., 2006. Angewandte Statistik. Springer – Verlag.

Sato, Y., Iwamoto, J., Kanoko, T., Satoh, K., 2005. Amelioration of osteoporosis and hypovitaminosis d by sunlight exposure in hospitalized, elderly women with alzheimer's disease: a randomized controlled trial. Journal of Bone and Mineral Research 20 (8), 1327 – 1333.

Schmidt, H., Kettler, A., Heuer, F., Simon, U., Claes, L., Wilke, H.-J., 2007. Intradiscal pressure, shear strain, and fiber strain in the intervertebral disc under combined loading. Spine 32 (7), 748 – 755.

Schürch, M. A., Rizzoli, R., Slosman, D., Vadas, L., Vergnaud, P., Bonjour, J. P., 1998. Protein supplements increase serum insulin-like growth factor-i levels and attenuate proximal femur bone loss in patients with recent hip fracture. a randomized, double-blind, placebo-controlled trial. Annals of Internal Medicine 128 (10), 801 – 809.

Shea, B., Wells, G., Cranney, A., Zytaruk, N., Robinson, V., Griffith, L., Ortiz, Z., Peterson, J., Adachi, J., Tugwell, P., Guyatt, G., 2002. Meta-analyses of therapies for postmenopausal osteoporosis. vii. meta-analysis of calcium supplementation for the prevention of postmenopausal osteoporosis. Endocrine Reviews 23 (4), 552 – 559.

Shi, X., Sherry Liu, X., Wang, X., E., G. X., Niebur, G. L., 2010. Type and orientation of yielded trabeculae during overloading of trabecular bone along orthogonal directions. Journal of Biomechanics in press.

Shirazi-Adl, A., Ahmed, A. M., Shrivastava, S. C., 1986. Mechanical response of a lumbar motion segment in axial torque alone and combined with compression. Spine 11 (9), 914 – 927.

Silva, M. J., 2007. Biomechanics of osteoporotic fractures. Injury 38 (S3), S69 – S76.

Siris, E., Delmas, P. D., 2008. Assessment of 10-year absolute fracture risk: a new

paradigm with worldwide application. Osteoporosis International 19 (4), 383 – 384.

Sontag, A., Krege, J. H., 2009. First fractures among postmenopausal women with osteoporosis. Journal of Bone and Mineral Metabolism 28 (4), 485 – 488.

Swadener, J. G., Pharr, G. M., 2001. Indentation of elastically anisotropic half-spaces by cones and parabolae of revolution. Philosophical Magazine 81, 447 – 466.

Tabor, Z., Rokita, E., 2007. Quantifying anisotropy of trabecular bone from gray-level images. Bone 40, 966 – 972.

Teo, J., Si-Hoe, K., Keh, J., Teoh, S., 2007. Correlation of cancellous bone microarchitectural parameters from microct to ct number and bone mechanical properties. Materials Science and Engineering C 27, 333 – 339.

Thomsen, K., Gotfredsen, A., Christiansen, C., 1986. Is postmenopausal bone loss an age-related phenomenon? Calcified Tissue International 39 (3), 123 – 127.

Thurner, P. J., Wyss, P., Voide, R., Stauber, M., Stampanoni, M., Sennhauser, U., Müller, R., 2006. Time-lapsed investigation of three – dimensional failure and damage accumulation in trabecular bone using synchroton light. Bone 39, 289 – 299.

Turner, C. H., Rho, J., Takano, Y., Tsui, T. Y., Pharr, G. M., 1999. The elastic properties of trabecular and cortical bone tissues are similar: results from two microscopic measurement techniques. Journal of Biomechanics 32 (4), 437 – 441.

Ulrich, D., Rietbergen, B. v., Laib, A., Rüegesegger, P., 1999. The ability of three-dimensional structural indices to reflect mechanical aspects of trabecular bone. Bone 25 (1), 55 – 60.

Verhulp, E., 2006. Analyses of trabecular bone failure. Ph.D. thesis, Technische Universiteit Eindhoven.

Verhulp, E., Rietbergen, B. v., Müller, R., Huiskes, R., 2008. Micro-finite element simulation of trabecular-bone post-yield behaviour-effects of material model, element size and type. Computer Methods in Biomechanics and Biomedical Engineering 11 (4), 389 – 395.

von Meyer, G. H., 1867. Die architektur der spongiosa. Archiv für Anatomie, Physiologie und wissenschaftliche Medicin 34, 615 – 628.

Wachtel, E. F., Keaveny, T. M., 1997. Dependence of trabecular damage on mechanical strain. Journal of Orthopaedic Research 15 (5), 781 – 787.

Wald, M. J., Vasilic, B., Saha, P. K., Wehrli, F. W., 2007. Spatial autocorrelation and mean intercept length analysis of trabecular bone anisotropy applied to in vivo magnetic resonance imaging. Medical Physics 34 (3), 1110 – 1120.

Waldorff, E. I., Goldstein, S. A., McCreadie, B. R., 2007. Age-dependent microdamage removal following mechanically induced microdamage in trabecular bone in vivo. Bone 40 (2), 425 – 432.

Wang, X., Shen, X., Li, X., Mauli Agrawal, C., 2002. Age-related changes in the collagen network and toughness of bone. Bone 31 (1), 1 – 7.

Weickert, J., 1998. Anisotropic diffusion in image processing. B. G. Teubner Stuttgart.

Weiner, S., Arad, T., Sabanay, I., Traub, W., 1997. Rotated plywood structure of primary lamellar bone in the rat: Orientations of the collagen fibril arrays. Bone 20 (6), 6.

Whitehouse, W. I., 1974. The quantitative morphology of anisotropic trabecular bone. Journal of Microscopy 101, 153 – 168.

Wolff, J., 1870. Ueber die innere architectur der knochen und ihre bedeutung für die frage vom knochenwachsthum. Virchow's Archiv für Anatomie, Physiologie und wissenschaftliche Medicin 50 (3), 389 – 450.

Wolff, J., 1892. Das Gesetz der Transformation der Knochen. Verlag von August Hirschwald, Berlin.

Wolfram, U., Wilke, H.-J., Zysset, P. K., 2010a. Rehydration of vertebral trabecular bone: Influences on its anisotropy, its stiffness and the indentation work with a view to age, gender and vertebral level. Bone 46 (2), 348 – 354.

Wolfram, U., Wilke, H.-J., Zysset, P. K., 2010b. Transverse isotropic elastic properties of vertebral trabecular bone matrix measured using microindentation under dry conditions (effects of age, gender and vertebral level). Journal of Mechanics in Medicine and Biology 10 (1), 139 – 150.

World Health Organization, 1994. Assessment of fracture risk and its application to screening for postmenopausal osteoporosis. Technical Report Series 843, World Health Organization.

World Health Organization, 2003. Prevention and management of osteoporosis. Technical Report Series 921, World Health Organization.

Zhang, J., Niebur, G. L., Ovaert, T. C., 2008. Mechanical property determination of bone through nano- and micro-indentation testing and finite element simulation. Journal of Biomechanics 41 (2), 267 – 275.

Zysset, P. K., 1994. A constitutive law for trabecular bone. Ph.D. thesis, École Polytechnique Fédérale de Lausanne.

Zysset, P. K., 2003. A review of morphology-elasticity relationships in human trabecular bone: Theories and experiments. Journal of Biomechanics 36, 1469 – 1485.

Zysset, P. K., Curnier, A., 1995. An alternative model for anisotropic elasticity based on fabric tensors. Mechanics of Materials 21, 243 – 250.

Zysset, P. K., Curnier, A., 1996. A 3d damage model for trabecular bone based on fabric tensors. Journal of Biomechanics 29, 1549 – 1558.

Zysset, P. K., Guo, E. X., Hoffler, E. C., Moore, K. E., Goldstein, S. A., 1999. Elastic modulus and hardness of cortical and trabecular bone lamellae measured by nanoindentation in the human femur. Journal of Biomechanics 32 (10), 1005 – 1012.

Appendix A

Acknowledgements

Over the past years many people contributed in different ways and to different extends to the thesis. I have to admit, that I finish with more open questions than answers which is a brilliant feeling. My astonishment over natures beauty, especially found in bone, increased with every day working on this project. Finishing up, I humbly feel smaller in the shade of natures evolutionary might. Bearing this in mind, my deepest thanks go to all of them who helped me on this way. Without you, I would not have had the freedom to discover the beauty of bone tissue and science.

Especially, I would like to thank two outstanding scientists without who this work would not have been shaped. First, I would like to thank my supervisor Prof. Dr. Hans-Joachim Wilke. This thesis would not have been possible without his patience and willingness to support establishing my ideas, the project and the grand application. I am deeply thankful for his trust in a good ending of that story.

Second, I would like to thank Prof. Dr. Philippe Zysset who took on to serve as second referee. Without his willingness to welcome me as a guest-researcher at the Institute of Lightweight Design and Structural Biomechanics in Vienna, the presented papers would not have been feasible. I am deeply thankful for his constant help, support and interest in my research.

One of the most important principles in science I learned from Prof. Wilke is that there is no science without funding. Therefore, I am happy to state that this thesis was supported by the Deutsche Forschungsgemeinschaft (German Research Foundation), grand number WI 1352/13 – 1.

Finally and most importantly, I want to thank my wife Christiane for her support, her patience and the backing she gives already just by knowing that she is part of my life. Without her, all this would be nothingness.

Appendix B

Scientific Curriculum Vitae

Personal Data	Uwe Wolfram July, 2nd 1979 Oelsnitz (Vogtland) Married German
Career Progression	
03/2009 – today	PhD student, Institute of Orthopaedic Research and Biomechanics, Ulm University, Ulm, Germany
08/2008 – 02/2009	Guest-Researcher, Institute of Lightweight Design and Structural Biomechanics (Professor Philippe Zysset), University of Technology Vienna, Vienna, Austria
10/2006 – 07/2008	PhD student, Institute of Orthopaedic Research and Biomechanics, Ulm University, Ulm, Germany
01/2006 – 10/2006	PhD student and Guest-Researcher, Institute for Numerical Simulation (Prof. Martin Rumpf), Bonn University, Bonn, Germany
Academic Background	
01/2006 – today	PhD student on "Fracture Risk of Vertebral Bodies", supervisor Professor Dr. Hans-Joachim Wilke, Institute of Orthopaedic Research and Biomechanics, Ulm University, Ulm, Germany
09/1999 – 11/2005	Mechanical Engineering, Chemnitz University of Technology, Chemnitz, Germany
Social Service	
08/2002 – 04/2003	Camphill Community Jerpoint, Thomastown, Republic of Ireland
Military Service	
09/1998 – 06/1999	1. Batterie, Artilleriebeobachtungsbatallion 131, Mühlhausen (Thüringen), Germany
Abitur (similar to A-levels)	
07/1998	Gymnasium Markneukirchen, Markneukirchen, Germany

Appendix C

List of Publications

1. Klammert U., Ignatius A., **Wolfram U.**, Reuther T., Gbureck, U. **in press**. In vivo degradation of low temperature calcium and magnesium phosphate ceramics in a heterotopic model. Acta Biomaterialia.
2. Rumpf, M., Schwen, L. O., Wilke, H.-J., **Wolfram U., in press**. Numerical homogenization of trabecular bone specimens using composite finite elements. International Journal of Multiphysics.
3. Claes, L., Reusch, M., **Wolfram U.**, Göckelmann, M., Ignatius, A. **in press**. Modelle der metaphysären Frakturheilung. Osteologie.
4. **Wolfram U.**, Wilke H.-J., Zysset P. K., **2011**. Damage accumulation in vertebral trabecular bone depends on loading mode and direction. Journal of Biomechanics 44, 1164 – 1169.
5. Wehner, T., **Wolfram U.**, Henzler, T., Niemeyer, F., Claes L., Simon U., **2010**. Musculoskeletal loads in the hindlimb of the rat during gait. Journal of Biomechanics 43 (13), 2473 – 2479.
6. **Wolfram U.**, Wilke H.-J., Zysset P. K., **2010b**. Valid μFinite Element models of vertebral trabecular bone can be obtained using tissue properties measured with nanoindentation under wet conditions. Journal of Biomechanics 43 (9), 1731 – 1737.
7. **Wolfram U.**, Wilke H.-J., Zysset P. K., **2010a**. Transverse isotropic elastic properties of vertebral trabecular bone matrix measured using microindentation under dry conditions (effects of age, gender and vertebral level). Journal of Mechanics in Medicine and Biology 10 (1), 139 – 150
8. **Wolfram U.**, Wilke H.-J., Zysset P. K., **2010**. Rehydration of vertebral trabecular bone: Influences on its anisotropy, its stiffness and the indentation work with a view to age, gender and vertebral level. Bone 46 (2), 348 –354
9. **Wolfram U.**, Schwen L. O., Simon U., Rumpf M., Wilke H.-J., **2009b**. Statistical osteoporosis models using composite finite elements: A parameter study. Journal of Biomechanics 42 (13), 2205 – 2209.
10. **Wolfram U.**, Schmitz, B., Heuer F., Reinehr, M., Wilke H.-J., **2009a**. Vertebral trabecular main direction can be determined from clinical CT datasets using the gradient structure tensor and not the inertia tensor – a case study. Journal of Biomechanics 42 (10), 1390 – 1396.

11. Hohmann A., **Wolfram U.**, Geiger M., Boryor A., Kober C., Sander C., Sander F. G., **2009**. Correspondences of hydrostatic pressure in periodontal ligament with regions of root resorption: A clinical and a finite element study of the same human teeth. Computer Methods and Programs in Biomedicine 93, 155 – 161.

12. Boryor A., Hohmann A., Geiger M., **Wolfram U.**, Sander C., Sander F. G., **2009**. A downloadable meshed human canine tooth model with PDL and bone for finite element simulations. Dental Materials 25, 57 – 62.

13. Heuer F., **Wolfram U.**, Schmidt H., Wilke H.-J., **2008**. A method to obtain surface strains of soft tissues using a laser scanning device. Journal of Biomechanics 41 (11), 2402 – 2410.

14. Hohmann A., **Wolfram U.**, Geiger M., Boryor A., Sander C., Faltin R., Faltin K. G. S. F., **2007**. Periodontal ligament hydrostatic pressure with areas of root resorption after application of a continuous torque moment. Angle Orthodontist 77 (4), 653 – 659.